CORA Cork Open Research Archive
Cartlann Taighde Oscailte Chorcaí

Title	Spatial modeling and analysis of generalized sandwich design for compliant rotational and translational joints
Authors	Li, Shiyao;Zhu, Jiaxiang;Hao, Guangbo
Publication date	2026-07-15
Original Citation	Li, S, Zhu, J & Hao, G 2026, 'Spatial modeling and analysis of generalized sandwich design for compliant rotational and translational joints', International Journal of Mechanical Sciences, vol. 322, 111698, pp. 1-31. https://doi.org/10.1016/j.ijmecsci.2026.111698
Type of publication	Article (peer-reviewed)
Link to publisher's version	https://www.scopus.com/pages/publications/105038838600 - 10.1016/j.ijmecsci.2026.111698
Rights	© 2026, authors. Published by Elsevier Ltd. This is an open access article under the CC BY license (http://creativecommons.org/licenses/by/4.0/) - https://creativecommons.org/licenses/by/4.0/
Download date	2026-11-11 13:02:28
Item downloaded from	https://hdl.handle.net/10468/19585

UCC
University College Cork, Ireland
Coláiste na hOllscoile Corcaigh

International Journal of Mechanical Sciences 322 (2026) 111698



Contents lists available at ScienceDirect

International Journal of Mechanical Sciences

journal homepage: www.elsevier.com/locate/ijmecsci





Spatial modeling and analysis of generalized sandwich design for compliant rotational and translational joints

Shiyao Li [a,b], Jiaxiang Zhu [b,c], Guangbo Hao [b,*]

[a] School of Artificial Intelligence, Shenyang Aerospace University, Shenyang 110136, China
[b] School of Engineering and Architecture-Electrical and Electronic Engineering, University College Cork, Cork T12 K8AF, Ireland
[c] College of Engineering & Physical Sciences, Aston University, Birmingham B47ET, United Kingdom

ARTICLE INFO

Keywords:
Compliant joints
Nonlinear spatial analysis
Stiffness variation
Asymmetric design
Remote center of motion
Center shift

ABSTRACT

Compliant joints are usually fabricated from elastic materials, with elastic sheets, rods, or their combination being the most common implementations. However, a generalized design and spatial model of compliant joints that can evolve into either rotational or translational joints has not been fully investigated. Furthermore, a generalized method for deriving the center shift of rotational joints is also lacking. This paper aims to address the above concerns by presenting a generalized compliant joint composed of elastic sheets. Building on foundational concepts from prior research, this study utilizes the sandwich interconnection to increase out-of-plane stiffness. A normalized nonlinear spatial analytical model for the generalized sandwich design is proposed and fully verified via nonlinear finite element analysis. The out-of-plane stiffness of the joint is analyzed sufficiently along each direction, in terms of stiffness changes/improvement against geometric parameters and primary rotational motion. Symmetric joints are prevalent, but this study uncovers asymmetric features by comparing normalized stiffness ratios of asymmetric and symmetric sandwich joints across a range of geometric parameters. Prototypes of both the generalized sandwich design and its counterpart, the two-layer design, have been manufactured and experimentally tested, thereby providing further verification of the analytical model and the nonlinear stiffness characteristics. Finally, employing our analytical model, a generalized method for determining the center shift of complaint rotational joints is established. This method is employed in a global parameter search to optimize center shift in generalized sandwich rotational joints, ensuring solution stability. Topology optimization is also used to achieve weight reduction in the proposed design.

1. Introduction

Compliant joints [1–3] serve as fundamental components in mechanical transmissions [4], mechanisms [5], and machines [6]. They provide frictionless and backlashless motion through elastic deformation and have been applied in diverse fields such as robotics [7–17], precision positioning systems [4,18–21], and energy absorption equipment [22–25]. Robotics composed of specially-designed joints can be made in slender shapes with high-degree-of-freedom (DoF), making them ideal for navigating constrained environments. Dong et al. [26–31] developed a 25-DoF compliant continuum robot with compliant revolute joints, each composed of two short compliant wire-beam structures, for inspecting and repairing turbine engines. Yuan et al. [32] introduced a deployable continuum robot with a coiling mechanism for inspection and maintenance in constrained environments. This robot significantly reduces the system's axial dimension compared to robots using linear feeding mechanisms. Kai et al. [33–36] designed a compliant continuum robot incorporating compliant wire-beam joints for minimally invasive surgery. The use of compliant joints enables the positioning systems to offer precise motions with minimal friction and backlash. Zhao et al. [37] introduced a crossing spring pivot for precision engineering applications [38,39], including aerospace mechanisms and optical alignment systems. Awtar et al. [40] proposed a compact XY flexure stage by arranging a series of compliant parallelogram joints, suitable for semiconductor mask and wafer alignment, scanning interferometry, and atomic force microscopy. Compliant joints allow for the creation of simpler, more compact, and lighter structures for energy absorption equipment [22]. Hargrove et al. [23] presented a semi-circular compliant joint for storing strain energy during deformation. Nastevska et al. [41] utilized a series of asymmetric compliant joints to build

* Corresponding author.
E-mail address: G.Hao@ucc.ie (G. Hao).

https://doi.org/10.1016/j.ijmecsci.2026.111698
Received 23 August 2025; Received in revised form 7 April 2026; Accepted 6 May 2026
Available online 8 May 2026
0020-7403/© 2026 The Author(s). Published by Elsevier Ltd. This is an open access article under the CC BY license (http://creativecommons.org/licenses/by/4.0/).

a contact-aided mechanism for directional energy absorption.

Parasitic motions [42–48] of compliant joints are along the degree-of-constraint (DoC) direction (i.e., bearing direction). They are undesired and often challenging to eliminate due to the inherent kinematic coupling that accompanies the primary motion (DoF) and the inevitable loading along with the bearing direction. Many researchers are motivated to reduce parasitic motions in their designs. As for rotational joints, center shift [49] is the primary parasitic motion. Zhao et al. [37,50–52] optimized the geometric parameters of the crossing spring pivot to mitigate the center shift. However, the optimized results should be specified with an accuracy of at least three decimal places, which may make it challenging to fabricate in high precision. Li et al. designed a parallel compound cross spring pivot [53] and reduced center shift by incorporating both the common and the anti-buckling crossing configuration. While this design achieves minimal center shift for any crossing position, its overall motion range is limited. Bai et al. [54] designed a compliant rotational joint comprising two trapezoidal pivots connected in series. When three such joints are arranged in parallel to form a new rotational joint, the resulting over-constraint effect suppresses parasitic motions of the new rotational joint. However, a drawback in [54] is that the joint's axial stiffness drops sharply as the primary motion increases, and the over-constraint method used in [53,54] also lead to an undesired increase of stiffness in primary rotation. It is worth noting that existing geometric methods for center shifts [55] are primarily restricted to planar deformation and are highly dependent on specific structural parameters (e.g., the crossing position denoted by λ in cross-spring pivots), which cannot be readily extended to general compliant rotational joints that do not employ crossing spring pivots. Accordingly, this paper aims aim to propose a generalized formulation that calculates the spatial center shift directly through the vector difference between the deformed and undeformed spatial coordinates of the intersection point. This coordinate-based approach is intrinsically spatial and geometry-independent, meaning it can be universally applied to various types of compliant rotational joints consisting of elastic sheet or beams, not just cross-spring pivots. The spatial center shift in this paper is derived from a nonlinear spatial analytical model, with the computation time almost being the same as to the exiting planar closed-form center shift formulas [55], and can enable the subsequent model-based design optimization.

While symmetric and parallel (or parallel) arrangements of compliant joints (as a type of over-constraint method) are widely adopted to minimize parasitic motions [19,56–59] and cross-spring pivots serve as common rotational joints [60–64], exploring designs beyond these conventional forms can unlock unique functionalities. First, asymmetric compliant joints offer certain performance that cannot be obtained by symmetric designs. For example, in energy-absorbing applications, they can be designed to efficiently absorb energy in one direction (e.g., folding) while maintaining rigidity in the opposite direction (e.g., load-bearing) [41]. Moreover, the principle of asymmetric design can be extended to systems with material asymmetry or asymmetric loading conditions, owing to its core capability to tailor spatial compliance distribution [65,66]. Furthermore, moving the rotational center away from the joint itself—a concept known as the remote center of motion (RCM)—provides another critical advantage. RCM compliant joints are particularly beneficial in applications like minimally invasive surgery [67] and knee exoskeletons [68], as they achieve a highly compact physical envelope for the joint while still permitting a large angular deflection of the connected components. Therefore, both asymmetric features and RCM should be explored for advancing the performance of compliant joints.

Various analytical modeling methods have been developed for the analysis of compliant mechanisms; however, they still exhibit certain limitations. The Pseudo-Rigid-Body Model [23,69–71] simplifies analysis by approximating flexures as rigid links with torsional springs, offering computational efficiency. However, its reliance on empirical correction factors reduces accuracy for highly flexible mechanisms and/or complex loading conditions. Euler-Bernoulli Beam Theory [72,73] provides closed-form solutions for large deflections in slender beams but neglects shear deformation, leading to inaccuracies in thick or short beams. Timoshenko Beam Theory [74–76] accounts for shear effects, improving accuracy for short or thick beams. However, its governing equations often require numerical solutions, raising computational costs. In this paper, we develop an analytical model [49] for the proposed design based on the Beam Constraint Model (BCM) [8,77–79] and Free-Body Diagram (FBD) [18,80], which is a nonlinear spatial kinetostatic model [12]. This analytical model can accurately strike a balance between mechanical rigor and practical adaptability and allows for a thorough evaluation of the geometric parameters that influence deformation and stiffness.

High bearing stiffness is crucial for suppressing parasitic motions for compliant joints. The work in [81,82] proposed the use of sandwich interconnection to increase out-of-plane (or bearing) stiffness for symmetric parallelogram flexure mechanisms (PFMs). The key contribution in [81,82] is that the proposed sandwich interconnection significantly enhances out-of-plane stiffness of the PFMs, without compromising (increasing) the in-plane DoF (or primary motion) stiffness, which is better than the prevailing over-constraint method as shown in [19,53,54,78]. Additionally, a general lumped-compliance beam for compliant mechanisms was introduced in our prior work [83], which was confined to **planar modelling and analysis in a single layer** and lacked a generalized design methodology for RCM rotational joints. However, the incorporation of the existing sandwich interconnection concept into **a general design framework (by combining a general lumped-compliance beam)** has not been reported and if and how the resulting out-of-plane stiffness **(to be spatially modeled)** is improved remains unknown. Therefore, spatial modeling and analysis are imperative to explicitly demonstrate and quantify the structural advantages of the sandwich configuration. Building upon the above advances, our study addresses the aforementioned concerns, including **general sandwich design of rotational joints with RCM**, nonlinear spatial analysis of asymmetric features, and derivation of general center shift equations.

The primary contributions of this paper are summarized as follows:

(1) A generalized sandwich design with RCM is proposed and spatially modeled: The present work generalizes the sandwich interconnection concept and extends its applicability beyond specific architectures for both rotational and translational joints. This broadens the design envelope of compliant joints, and the developed spatial model is also suitable for analyzing **traditional symmetric joints with manufacturing deviations**.

(2) The out-of-plane stiffness of the generalized sandwich designs is comprehensively studied based on the developed spatial model, leading to a different conclusion from the previous findings: Although the sandwich design can lead to the highest stiffness in the out-of-plane directions as compared to the two counterpart designs, stiffness changes of the sandwich joints are not always the smallest among their counterparts.

(3) Asymmetric characteristics of generalized sandwich joints are analyzed: Compared to its symmetric counterpart, the asymmetric generalized sandwich design exhibits unique characteristics in stiffness variation. Specifically, its out-of-plane stiffness ratios demonstrate distinct sensitivities to different asymmetric geometric parameters. This unique feature allows the stiffness ratios to be precisely adjusted by tuning these parameters, thereby enabling targeted directional stiffness optimization.

(4) A generalized derivation of center shift for rotational joints is proposed: Leveraging the advantages of spatial nonlinear modeling, the presented derivation allows for the determination of center shift for rotational centers at any location. A key advantage of

this approach is its broad applicability to various joint types, including, but not limited to, cross-spring pivots.

(5) A dual-optimization framework is established. The first optimization targets the parasitic center shift in generalized rotational joints based on the spatial model. A drawback of sandwich structures lies in the increase in overall structural mass due to the sandwich interconnection itself; thus, the second optimization aims to minimize the structural weight by using topology optimization.

This paper is organized as follows. In Section 2, a spatial nonlinear analytical model of the generalized sandwich design for the lumped-compliance sheet (GSLS) is introduced, and its normalized nonlinear spatial analytical model is derived. Building on this model, Section 3 presents a generalized sandwich design for rotational joints (GSRJ) and derives the corresponding generalized analytical model. Note that a generalized sandwich design for translational joints (GSTJ) can be derived from the GSRJ. Section 4 evaluates the model accuracy, normalized stiffness ratio comparisons between the GSRJ and its counterparts and comparisons of asymmetric and symmetric joints, followed by experimental tests and results. Section 5 carries out the derivation and optimization of the GSRJ center shift. Finally, Section 6 draws the conclusions of the paper.

2. GSLS model

Throughout this paper, we use the right-handed coordinate system and right-handed rule; we use capital symbols to denote dimensional parameters, and lower-case symbols to denote normalized (dimensionless) ones unless specified otherwise.

In this section, the design and normalized analytical model of the GSLS are described and derived. A parameterized lumped-compliance sheet is shown in Fig. 1(a). After integration with the sandwich interconnection, the resulting GSLS is shown in Fig. 1(b). It consists of two parameterized lumped-compliance sheets, a sandwich interconnection, a fixed stage, and a motion stage. The generalized model can be directly applied to design multi-sheet mechanisms with high out-of-plane stiffness. The local coordinate system o_i-$x_iy_iz_i$ is defined in Fig. 1(c). o_i denotes the midpoint between o_{iA} and o_{iB} and lies on the O_G-X_GY_G plane. As shown in Fig. 1(d), the axes directions of o_{iA}-$x_{iA}y_{iA}z_{iA}$ (or o_{iB}-$x_{iB}y_{iB}z_{iB}$) are consistent with those of o_i-$x_iy_iz_i$. We use O_G-$X_GY_GZ_G$ to denote the global coordinate system and use o_{iA}-$x_{iA}y_{iA}z_{iA}$ and o_{iB}-$x_{iB}y_{iB}z_{iB}$ ($i = 1$ or 2 throughout the paper) to denote local coordinate systems of the GSLS; use sheet-i_A and sheet-i_B to denote each sheet. The global coordinate system is located at the center of the motion stage, with the origin denoted as O_G. The local coordinate system of each sheet is positioned at its free end, with the origin denoted as o_{iA} or o_{iB}. The directions of all the coordinate systems remain constant during the motion of the GSLS.

Eight independent geometric parameters include the sheet length, sheet tilt angle, sheet width, sheet thickness, height of the rigid block, height of the motion stage, horizontal distance between o_2 and O_G, and sandwich thickness. These parameters are denoted by L_i, α_i, U, T, B_1, H_1, B_2, and H_2, respectively, and all are positive values. The corresponding normalized values are denoted by l_i, α_i, u, t, b_1, h_1, b_2, and h_2, respectively. L_d denotes the characteristic length for normalization; all translational displacements and length parameters are divided by L_d. L_d is equal to the diagonal length of the resulting design. Forces and moments

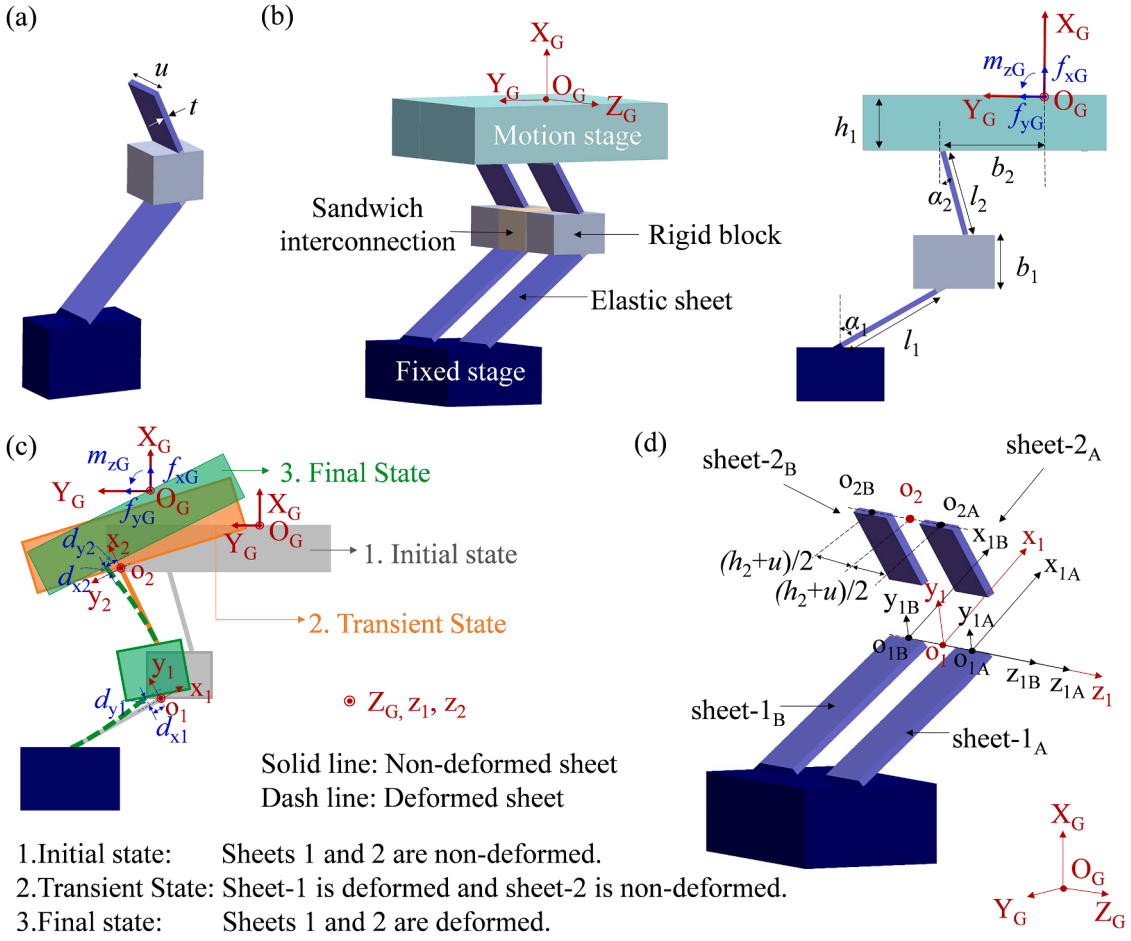


Fig. 1. Description of the GSLS model. (a) A parameterized lumped-compliance sheet; (b) The components and geometric parameters of the GSLS; (c) The local and global coordinate systems of the GSLS; (d) The local coordinate systems for sheet-1_A, sheet-1_B, sheet-2_A, and sheet-2_B.

are divided by EI_z/L_d^2 and EI_z/L_d, respectively, where I_z denotes the cross-section moment of inertia and is expressed as $UT^3/12$, and E is Young's Modulus of the material.

$\mathbf{R}_x$, $\mathbf{R}_y$, and $\mathbf{R}_z$ denote the rotational matrices about the X_G, Y_G, and Z_G-axes, respectively, which are shown as Eq. (5).

$$\mathbf{R}_{x(\theta_x)}=\begin{bmatrix}1&0&0\\0&\cos\theta_x&-\sin\theta_x\\0&\sin\theta_x&\cos\theta_x\end{bmatrix},\ \mathbf{R}_{y\left(\theta_y\right)}=\begin{bmatrix}\cos\theta_y&0&\sin\theta_y\\0&1&0\\-\sin\theta_y&0&\cos\theta_y\end{bmatrix},\ \mathbf{R}_{z(\theta_z)}=\begin{bmatrix}\cos\theta_z&-\sin\theta_z&0\\\sin\theta_z&\cos\theta_z&0\\0&0&1\end{bmatrix} \tag{5}$$

The analytical model for the GSLS is derived using a single-sheet model, complemented by compatibility and loading conditions. The single-sheet model proposed in [84] is the spatial BCM model, which is suitable for elastic sheets with high aspect ratios, as required in this paper. This approach is valid within an intermediate deformation range, where displacements are <10% of the sheet length, and rotations are below 0.1 rad. Key geometric assumptions require the ratios of sheet length to width and width to thickness, to exceed 10. The assumptions underlying the single-sheet model ensure the inclusion of key nonlinear aspects, such as second-order load-stiffening, the Wagner effect, and elastokinematic coupling. The analytical model of the GSLS includes twelve unknowns, consisting of the normalized displacements and rotations of o_i with respect to o_i-$x_iy_iz_i$, denoted by $\mathbf{d}_i$ and $\boldsymbol{\theta}_i$. Given the eight geometric parameters and loading inputs at O_G, the normalized displacements and rotations at O_G with respect to O_G-$X_GY_GZ_G$, denoted by $\mathbf{d}_G$ and $\boldsymbol{\theta}_G$, can be determined by solving the single-sheet model, compatibility condition, and loading equilibrium condition of the GSLS.

Step 1: Single sheet model

We use the nonlinear spatial analysis method for a single sheet with a large aspect ratio, which is presented in Appendix A of [84].

Step 2: Compatibility condition of the GSLS in a deformed state

The compatibility condition of the GSLS includes rotational and translational compatibility conditions. The rotational compatibility condition is given by Eqs. (1) and (2).

$$\mathbf{R}_G=\mathbf{R}_{z(\beta_1)}^{-1}\mathbf{R}_1\mathbf{R}_{z(\beta_2)}\mathbf{R}_2\mathbf{R}_{z(\beta_2)}^{-1}\mathbf{R}_{z(\beta_1)}, \tag{1}$$

where $\mathbf{R}_G$ and $\mathbf{R}_i$ denote the rotational matrices with respect to O_G-$X_GY_GZ_G$ and o_i-$x_iy_iz_i$, respectively; $\mathbf{R}_{z(\beta i)}$ denotes the rotational matrix with respect to the Z_G-axis, $\beta_1=\alpha_1$, and $\beta_2=\alpha_1+\alpha_2$.

$$\mathbf{R}_{iA}=\mathbf{R}_{iB}=\mathbf{R}_i, \tag{2}$$

where $\mathbf{R}_{iA}$ and $\mathbf{R}_{iB}$ denote the rotational matrices with respect to o_{iA}-$x_{iA}y_{iA}z_{iA}$ and o_{iB}-$x_{iB}y_{iB}z_{iB}$, respectively. The rotational sequences of $\mathbf{R}_G$, $\mathbf{R}_i$, $\mathbf{R}_{iA}$, and $\mathbf{R}_{iB}$ are described by the Euler angles using a ZXY convention as in Eq. (3); for instance, $\mathbf{R}_i$ can be derived as Eq. (4) and $\boldsymbol{\theta}_i=[\theta_{xi},\ \theta_{yi},\ \theta_{zi}]^T$.

$$\mathbf{R}=\mathbf{R}_{x(\theta_x)}\mathbf{R}_{z(\theta_z)}\mathbf{R}_{y\left(\theta_y\right)}, \tag{3}$$

$$\mathbf{R}_i=\mathbf{R}_{x(\theta_{xi})}\mathbf{R}_{z(\theta_{zi})}\mathbf{R}_{y\left(\theta_{yi}\right)}, \tag{4}$$

The translational compatibility condition is given by Eqs. (6) and (9).

$$\mathbf{d}_G=\mathbf{R}_{z(\beta_1)}^{-1}\mathbf{d}_{T1}+\mathbf{R}_{z(\beta_1)}^{-1}\mathbf{R}_1\mathbf{R}_{z(\beta_2)}\mathbf{d}_{T2}, \tag{6}$$

where $\mathbf{d}_{Ti}$ denotes the normalized displacements of O_G with respect to o_i-$x_iy_iz_i$, as given by Eq. (7).

$$\mathbf{d}_{Ti}=\mathbf{R}_i\mathbf{O}_{G_oi}-\mathbf{O}_{G_oi}+\mathbf{d}_i, \tag{7}$$

$\mathbf{O}_{G_oi}$ denotes the normalized coordinates of O_G with respect to o_i-$x_iy_iz_i$ in the non-deformed condition of the GSLS; ${}^2\mathbf{T}_{2m}$ denotes a translational matrix; they are given by Eq. (8).

$$\mathbf{O}_{G_o1}=\mathbf{R}_{z(\beta_1)}\begin{bmatrix}l_2\cos\alpha_2+h_1+(t\sin\alpha_1)/2+b_1+t\sin\alpha_2\\l_2\sin\alpha_2-b_2\\0\end{bmatrix},\mathbf{O}_{G_o2}={}^2\mathbf{T}_{2m}\begin{bmatrix}-b_2\sin\alpha_2+h_1\cos\alpha_2\\-b_2\cos\alpha_2-h_1\sin\alpha_2\\0\end{bmatrix},{}^2\mathbf{T}_{2m}=\begin{bmatrix}\mathbf{R}_2&\mathbf{d}_2\\\mathbf{0}_{1\times3}&1\end{bmatrix} \tag{8}$$

In Fig. 1(d), sheet-i_A and sheet-i_B are in parallel, so the rotations and displacements of each sheet with respect to o_{iA}-$x_{iA}y_{iA}z_{iA}$ or (o_{iB}-$x_{iB}y_{iB}z_{iB}$) can be expressed by those with respect to o_i-$x_iy_iz_i$.

$$\mathbf{d}_{iA}=\mathbf{R}_i\mathbf{o}_{iA_oi}-\mathbf{o}_{iA_oi}+\mathbf{d}_i\ \text{and}\ \mathbf{d}_{iB}=\mathbf{R}_i\mathbf{o}_{iB_oi}-\mathbf{o}_{iB_oi}+\mathbf{d}_i \tag{9}$$

where $\mathbf{d}_{iA}$ and $\mathbf{d}_{iB}$ denote the normalized displacements of o_{iA} and o_{iB} with respect to o_{iA}-$x_{iA}y_{iA}z_{iA}$ and o_{iB}-$x_{iB}y_{iB}z_{iB}$, respectively. $\mathbf{o}_{iA_oi}$ and $\mathbf{o}_{iB_oi}$ denote the normalized coordinates of o_{iA} and o_{iB} with respect to o_i-$x_iy_iz_i$, and $\mathbf{o}_{iA_oi}=[0,\ 0,\ (h_2+u)/2]^T$ and $\mathbf{o}_{iB_oi}=[0,\ 0,\ -(h_2+u)/2]^T$.

Step 3: Loading equilibrium condition of the GSLS in a deformed condition

The elastic sheet-1_A and sheet-1_B are arranged in parallel, and they are connected in series with elastic sheet-2_A and sheet-2_B The loading equilibrium condition of the GSLS in a deformed condition is given by Eqs. (10) and (11).

$$\begin{bmatrix}\mathbf{f}_1\\\mathbf{m}_1\end{bmatrix}=\mathbf{D}_{p1}^T\mathbf{R}_{Rz(\beta_1)}\begin{bmatrix}\mathbf{f}_G\\\mathbf{m}_G\end{bmatrix}, \tag{10}$$

$$\begin{bmatrix}\mathbf{f}_2\\\mathbf{m}_2\end{bmatrix}=\mathbf{D}_{p2}^T\mathbf{R}_{Rz(\beta_2)}^{-1}\mathbf{R}_{R1}^{-1}\mathbf{R}_{Rz(\beta_1)}\begin{bmatrix}\mathbf{f}_G\\\mathbf{m}_G\end{bmatrix}, \tag{11}$$

where $\mathbf{f}_G$, $\mathbf{m}_G$ and $\mathbf{f}_i$, $\mathbf{m}_i$ denote the normalized forces and moment with respect to O_G-$X_GY_GZ_G$ and o_i-$x_iy_iz_i$, respectively; and $\mathbf{f}_G=[f_{xG},f_{yG},f_{zG}]^T$, $\mathbf{f}_i=[f_{xi},f_{yi},f_{zi}]^T$, $\mathbf{m}_G=[m_{xG},m_{yG},m_{zG}]^T$, $\mathbf{m}_i=[m_{xi},m_{yi},m_{zi}]^T$; $\mathbf{D}_{pi}$ denote the 6 × 6 translational matrix, as shown in Eq. (12); $\mathbf{R}_{R1}$ and $\mathbf{R}_{Rz(\beta i)}$ denote the 6 × 6 rotational matrices, as given by Eq. (13); β_i can be found in Eq. (1).

$$\mathbf{D}_{pi}=\begin{bmatrix}\mathbf{I}_{3\times3} & \begin{bmatrix}0 & \mathbf{O}_{Gm_o_i}(3,1) & -\mathbf{O}_{Gm_o_i}(2,1)\\ -\mathbf{O}_{Gm_o_i}(3,1) & 0 & \mathbf{O}_{Gm_o_i}(1,1)\\ \mathbf{O}_{Gm_o_i}(2,1) & -\mathbf{O}_{Gm_o_i}(1,1) & 0\end{bmatrix}\\ \mathbf{0}_{3\times3} & \mathbf{I}_{3\times3}\end{bmatrix}, \tag{12}$$

$\mathbf{O}_{Gm_oi}$ denotes the normalized coordinates of O_G with respect to o_i-$x_iy_iz_i$ in a deformed condition of the GSLS, and is given by $\mathbf{O}_{Gm_oi}=\mathbf{R}_i\mathbf{O}_{G_oi}+\mathbf{d}_i$.

$$\mathbf{R}_{R1}=\begin{bmatrix}\mathbf{R}_1 & \mathbf{0}_{3\times3}\\ \mathbf{0}_{3\times3} & \mathbf{R}_1\end{bmatrix} \text{ and } \mathbf{R}_{Rz(\beta_i)}=\begin{bmatrix}\mathbf{R}_{z(\beta_i)} & \mathbf{0}_{3\times3}\\ \mathbf{0}_{3\times3} & \mathbf{R}_{z(\beta_i)}\end{bmatrix}, \tag{13}$$

$$\begin{bmatrix}\mathbf{f}_i\\ \mathbf{m}_i\end{bmatrix}=\mathbf{D}_{piA}^{T}\begin{bmatrix}\mathbf{f}_{iA}\\ \mathbf{m}_{iA}\end{bmatrix}+\mathbf{D}_{piB}^{T}\begin{bmatrix}\mathbf{f}_{iB}\\ \mathbf{m}_{iB}\end{bmatrix}, \tag{14}$$

$\mathbf{f}_{iA}$, $\mathbf{m}_{iA}$, and $\mathbf{f}_{iB}$, $\mathbf{m}_{iB}$ denote the normalized forces and moment with respect to o_{iA}-$x_{iA}y_{iA}z_{Ia}$ and o_{iB}-$x_{iB}y_{iB}z_{iB}$, respectively. $\mathbf{D}_{piA}$ and $\mathbf{D}_{piB}$ denote 6 × 6 translational matrices, as given by Eqs. (15) and (16).

$$\mathbf{D}_{piA}=\begin{bmatrix}\mathbf{I}_{3\times3} & \begin{bmatrix}0 & \mathbf{o}_{iAm_o_i}(3,1) & -\mathbf{o}_{iAm_o_i}(2,1)\\ -\mathbf{o}_{iAm_o_i}(3,1) & 0 & \mathbf{o}_{iAm_o_i}(1,1)\\ \mathbf{o}_{iAm_o_i}(2,1) & -\mathbf{o}_{iAm_o_i}(1,1) & 0\end{bmatrix}\\ \mathbf{0}_{3\times3} & \mathbf{I}_{3\times3}\end{bmatrix}, \tag{15}$$

$\mathbf{o}_{iAm_oi}$ denotes the normalized coordinates of o_{iA} with respect to o_i-$x_iy_iz_i$ in a deformed condition of the GSLS. It is given by

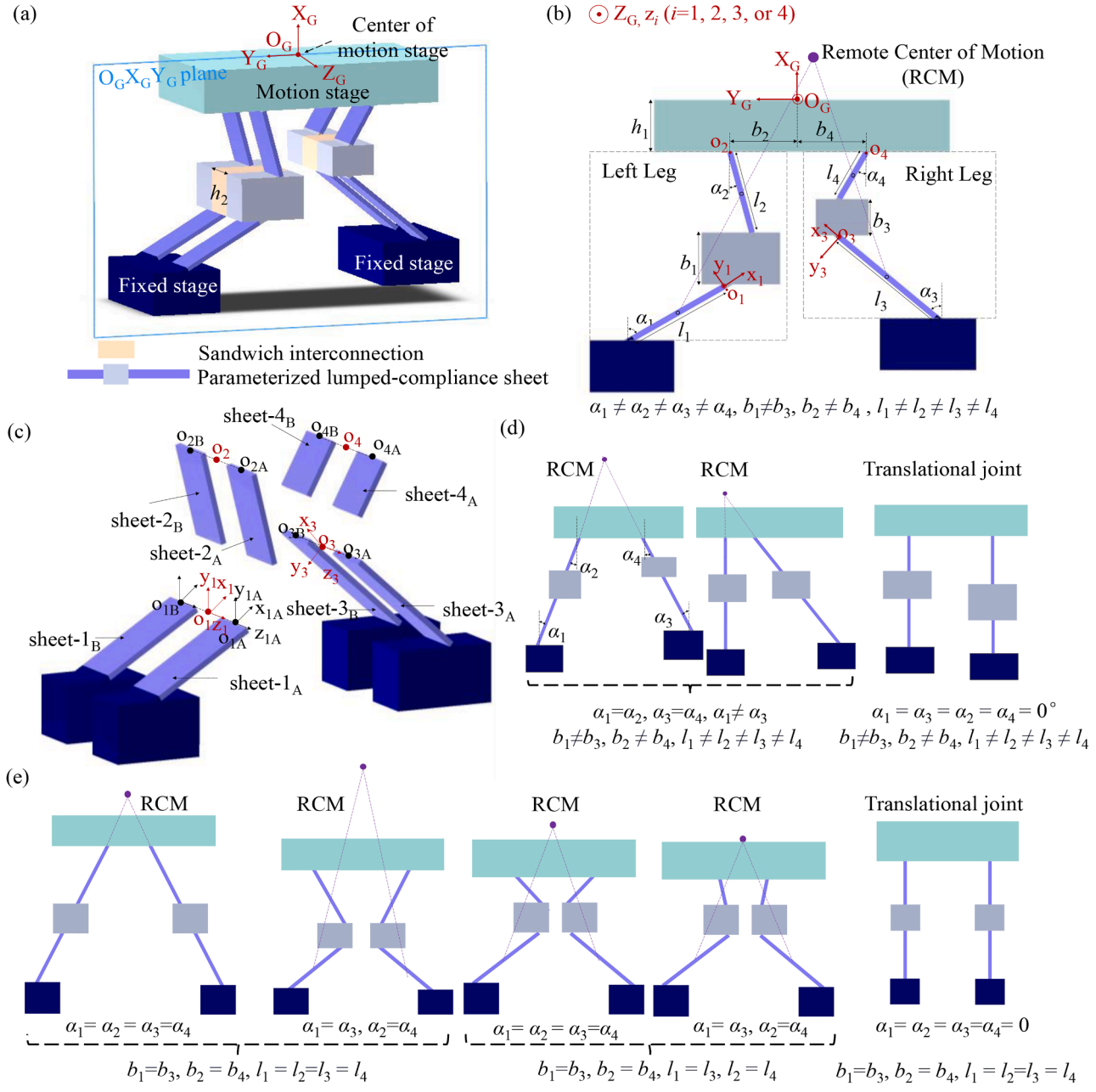


Fig. 2. The generalized sandwich designs. (a) Spatial display for the generalized model and the global coordinate system O_G-$X_GY_GZ_G$; (b) Front view of the model and geometric parameters; (c) Local coordinate systems for each sheet (o_j lies on the O_G-X_GY_G plane); (d) Examples of asymmetrical rotational and translational joints; (e) Examples of symmetrical rotational and translational joints. The relationships between their geometric parameters presented in the examples.

$\mathbf{o}_{i\mathrm{Am_}oi} = \mathbf{R}_i\mathbf{o}_{i\mathrm{A_}oi} + \mathbf{d}_i$.

$$\mathbf{D}_{pi\mathrm{B}} = \begin{bmatrix} & \begin{bmatrix} 0 & \mathbf{o}_{i\mathrm{Bm_}o_i}(3,1) & -\mathbf{o}_{i\mathrm{Bm_}o_i}(2,1) \\ -\mathbf{o}_{i\mathrm{Bm_}o_i}(3,1) & 0 & \mathbf{o}_{i\mathrm{Bm_}o_i}(1,1) \\ \mathbf{o}_{i\mathrm{Bm_}o_i}(2,1) & -\mathbf{o}_{i\mathrm{Bm_}o_i}(1,1) & 0 \end{bmatrix} \\ \mathbf{I}_{3\times3} & \\ \mathbf{0}_{3\times3} & \mathbf{I}_{3\times3} \end{bmatrix}, \tag{16}$$

$\mathbf{o}_{i\mathrm{Bm_}oi}$ denotes the normalized coordinates of $o_{i\mathrm{B}}$ with respect to o_i-$x_iy_iz_i$ in a deformed condition of the GSLS. It is given by $\mathbf{o}_{i\mathrm{Bm_}oi} = \mathbf{R}_i\mathbf{o}_{i\mathrm{B_}oi} + \mathbf{d}_i$.

3. GSRJ model

The generalized sandwich design for both rotational and translational joints is shown in Fig. 2(a). The individual geometric parameters of GSRJ are shown in Fig. 2(b). We denote each sheet as sheet-j_A and sheet-j_B (j = 1, 2, 3, or 4 throughout the paper), and the corresponding local coordinate systems (o_j-$x_jy_jz_j$) are shown in Fig. 2(c). By adjusting geometric parameters, various configurations of both rotational and translational joints can be generated, as depicted in Figs. 2(d) and (e). Among these, a series of rotational joints featuring the RCM is of particular interest. This section presents the derivation of the normalized analytical model for the GSRJ, which enables nonlinear spatial analysis of the joint's behavior. The nonlinear spatial analytical model for the GSTJ can then be obtained as a simplified case of the GSRJ model.

The modular unit of the GSRJ is the GSLS, whose normalized analytical model is presented in Section 2. We use l_3, l_4, α_3, α_4, b_3, and b_4 to denote the normalized sheet length, tilt angle, height of the rigid block, and horizontal distance between o_4 and O_G for the right leg of the GSRJ, respectively. The local coordinate systems for the right leg are established similarly to those described in Section 2. When geometric parameters and loading inputs are given, the displacements and rotations at O_G can be obtained by solving the GSLS model, compatibility condition, and loading condition of the GSRJ.

Step 1: GSLS model

This model is presented in Section 2.

Step 2: Compatibility condition of the GSRJ in a deformed condition

The rotational compatibility condition of the GSRJ is given by Eqs. (17) and (18).

$$\mathbf{R}_\mathrm{G} = \mathbf{R}_{z(\beta_1)}{}^{-1}\mathbf{R}_1\mathbf{R}_{z(\beta_2)}\mathbf{R}_2\mathbf{R}_{z(\beta_2)}{}^{-1}\mathbf{R}_{z(\beta_1)}, \tag{17}$$

$$\mathbf{R}_\mathrm{G} = \mathbf{R}_{z(\beta_3)}{}^{-1}\mathbf{R}_3\mathbf{R}_{z(\beta_4)}\mathbf{R}_4\mathbf{R}_{z(\beta_4)}{}^{-1}\mathbf{R}_{z(\beta_3)}, \tag{18}$$

where β_1=α_1; β_2=α_1+α_2; β_3=−α_3; β_4=−α_3−α_4. $\mathbf{R}_j$ denotes the rotational matrix at o_j with respect to o_j-$x_jy_jz_j$; $\mathbf{R}_\mathrm{G}$ denotes the rotational matrix at O_G with respect to O_G-$X_\mathrm{G}Y_\mathrm{G}Z_\mathrm{G}$.

The following equations outline the derivation of the rotational compatibility condition for the GSRJ. The normalized displacements with respect to o_2-$x_2y_2z_2$ and O_G-$X_\mathrm{G}Y_\mathrm{G}Z_\mathrm{G}$ can be expressed by those with respect to o_1-$x_1y_1z_1$, as shown in Eqs. (19) and (20), respectively.

$$\mathbf{d}_1 = \mathbf{R}_1\mathbf{R}_{z(\beta_2)}\mathbf{d}_2, \tag{19}$$

$$\mathbf{d}_1 = \mathbf{R}_{z(\beta_1)}\mathbf{d}_\mathrm{G}, \tag{20}$$

where $\mathbf{d}_j$ and $\mathbf{d}_\mathrm{G}$ denote the normalized displacements at o_j and O_G with respect to o_j-$x_jy_jz_j$ and O_G-$X_\mathrm{G}Y_\mathrm{G}Z_\mathrm{G}$, respectively; o_1-$x_1y_1z_1$ and o_3-$x_3y_3z_3$ are shown in Fig. 2(c); After the deformation of the sheet-1_A, sheet-1_B, sheet-3_A, and sheet-3_B, the coordinate systems o_2-$x_2y_2z_2$ and o_4-$x_4y_4z_4$ are located at o_2 and o_4, respectively.

According to our previous work [49], the mathematical relationship between the rotational angles of each sheet and those of the resulting compliant mechanism in terms of rotational sequences has been solved, so the rotational matrix of the left GSLS (denoted by $\mathbf{R}_\mathrm{LeftLeg}$) with respect to o_1-$x_1y_1z_1$ is given by Eq. (21). The relationship between $\mathbf{R}_\mathrm{G}$ and $\mathbf{R}_\mathrm{LeftLeg}$ can be given by Eq. (22).

$$\mathbf{R}_\mathrm{LeftLeg} = \mathbf{R}_1\mathbf{R}_{z(\beta_2)}\mathbf{R}_2\mathbf{R}_{z(\beta_2)}^{-1}, \tag{21}$$

$$\mathbf{R}_\mathrm{G} = \mathbf{R}_{z(\beta_1)}\mathbf{R}_\mathrm{LeftLeg}\mathbf{R}_{z(\beta_1)}^{-1}. \tag{22}$$

Substituting Eq. (21) into Eq. (22), the rotational compatibility condition between $\mathbf{R}_\mathrm{G}$, $\mathbf{R}_1$, and $\mathbf{R}_2$ can be obtained.

The normalized displacements with respect to o_4-$x_4y_4z_4$ and O_G-$X_\mathrm{G}Y_\mathrm{G}Z_\mathrm{G}$ can be expressed by those with respect to o_3-$x_3y_3z_3$, as shown in Eqs. (23) and (24), respectively.

$$\mathbf{d}_3 = \mathbf{R}_3\mathbf{R}_{z(\beta_4)}\mathbf{d}_4, \tag{23}$$

$$\mathbf{d}_3 = \mathbf{R}_{z(\beta_3)}\mathbf{d}_\mathrm{G}. \tag{24}$$

The rotational matrix of the right GSLS (denoted by $\mathbf{R}_\mathrm{RightLeg}$) with respect to o_3-$x_3y_3z_3$ is given by Eq. (25). The relationship between $\mathbf{R}_\mathrm{G}$ and $\mathbf{R}_\mathrm{RightLeg}$ can be given by Eq. (26). Substituting Eq. (25) into Eq. (26), the rotational compatibility condition between $\mathbf{R}_\mathrm{G}$, $\mathbf{R}_3$ and $\mathbf{R}_4$ can be obtained.

$$\mathbf{R}_\mathrm{RightLeg} = \mathbf{R}_3\mathbf{R}_{z(\beta_4)}\mathbf{R}_4\mathbf{R}_{z(\beta_4)}^{-1}, \tag{25}$$

$$\mathbf{R}_\mathrm{G} = \mathbf{R}_{z(\beta_3)}\mathbf{R}_\mathrm{RightLeg}\mathbf{R}_{z(\beta_3)}^{-1}, \tag{26}$$

The left GSLS is parallel with the right GSLS, so the translational compatibility condition of the GSRJ is given by Eqs. (27) and (30).

$$\mathbf{d}_\mathrm{G} = \mathbf{d}_\mathrm{LeftLeg} - \left(\mathbf{R}_\mathrm{G}\mathbf{o}_{2_\mathrm{G}} - \mathbf{o}_{2_\mathrm{G}}\right), \tag{27}$$

where $\mathbf{d}_\mathrm{LeftLeg}$ denotes the normalized displacements of the left GSLS in GSRJ with respect to O_G-$X_\mathrm{G}Y_\mathrm{G}Z_\mathrm{G}$, as given by Eq. (28); $\mathbf{o}_{2_o1}$ and $\mathbf{o}_{2_\mathrm{G}}$ denote the normalized coordinates of o_2 with respect to o_1-$x_1y_1z_1$ and O_G-$X_\mathrm{G}Y_\mathrm{G}Z_\mathrm{G}$ in a non-deformed condition of the GSRJ, respectively, as shown in Eq. (29).

$$\mathbf{d}_\mathrm{LeftLeg} = \mathbf{R}_{z(\beta_1)}^{-1}\left(\mathbf{R}_1\mathbf{R}_{z(\beta_2)}\right)\mathbf{d}_2 + \mathbf{R}_{z(\beta_1)}^{-1}(\mathbf{R}_1\mathbf{o}_{2_o1} - \mathbf{o}_{2_o1} + \mathbf{d}_1), \tag{28}$$

$$\mathbf{o}_{2_o1} = \mathbf{R}_{z(\beta_1)}\begin{bmatrix} -l_2\cos\alpha_2 - b_1 - (t\sin\alpha_1)/2 - (t\sin\alpha_2)/2 \\ -l_2\sin\alpha_2 \\ 0 \end{bmatrix}, \mathbf{o}_{2_\mathrm{G}} = \begin{bmatrix} -h_1 - (t\sin\alpha_2)/2 \\ b_2 \\ 0 \end{bmatrix} \tag{29}$$

Similarly, $\mathbf{d}_\mathrm{G}$ can also be expressed by Eq. (30).

$$\mathbf{d}_\mathrm{G} = \mathbf{d}_\mathrm{RightLeg} - \left(\mathbf{R}_\mathrm{G}\mathbf{o}_{4_\mathrm{G}} - \mathbf{o}_{4_\mathrm{G}}\right), \tag{30}$$

where $\mathbf{d}_\mathrm{RightLeg}$ denotes the normalized displacements of the right GSLS in GSRJ with respect to O_G-$X_\mathrm{G}Y_\mathrm{G}Z_\mathrm{G}$, as given by Eq. (31); $\mathbf{o}_{4_o3}$ and $\mathbf{o}_{4_\mathrm{G}}$ denote the normalized coordinates of o_4 with respect to o_3-$x_3y_3z_3$ and O_G-$X_\mathrm{G}Y_\mathrm{G}Z_\mathrm{G}$ in a non-deformed condition of the GSRJ, respectively, as given by Eq. (32).

$$\mathbf{d}_{\text{RightLeg}} = \mathbf{R}_{z(\beta_3)}{}^{-1}\left(\mathbf{R}_3\mathbf{R}_{z(\beta_4)}\right)\mathbf{d}_4 + \mathbf{R}_{z(\beta_3)}{}^{-1}\left(\mathbf{R}_3\mathbf{o}_{4_3} - \mathbf{o}_{4_3} + \mathbf{d}_3\right), \tag{31}$$

$\mathbf{o}_{2m_G}$ and $\mathbf{o}_{4m_G}$ denote the normalized coordinates of points o_2 and o_4 with respect to O_G-$X_GY_GZ_G$ in a deformed condition of the GSRJ, respectively; and $\mathbf{o}_{2m_G}=\mathbf{R}_G\mathbf{o}_{2_G}+\mathbf{d}_G$ and $\mathbf{o}_{4m_G}=\mathbf{R}_G\mathbf{o}_{4_G}+\mathbf{d}_G$.

$$\mathbf{o}_{4_o3} = \mathbf{R}_{z(\beta_3)}\begin{bmatrix} -l_4\cos\alpha_4 - b_3 - (t\sin\alpha_3)/2 - (t\sin\alpha_4)/2 \\ l_4\sin\alpha_4 \\ 0 \end{bmatrix},\ \mathbf{o}_{4_G} = \begin{bmatrix} -h_1 - (t\sin\alpha_4)/2 \\ -b_4 \\ 0 \end{bmatrix} \tag{32}$$

Step 3: Load-equilibrium condition of the GSRJ in a deformed condition

We use $\mathbf{f}_G$ and $\mathbf{m}_G$ to denote the normalized loading inputs with respect to O_G-$X_GY_GZ_G$ applied at O_G; use $\mathbf{f}_j$ and $\mathbf{m}_j$ to denote the normalized loads with respect to o_j-$x_jy_jz_j$. The load-equilibrium condition of the GSRJ is given by Eqs. (33), (34), (35) and (44).

$$\begin{bmatrix}\mathbf{f}_G \\ \mathbf{m}_G\end{bmatrix} = \mathbf{D}_{p2}^{T}\mathbf{R}_{Rz(\beta_1)}^{-1}\mathbf{R}_{R1}\mathbf{R}_{Rz(\beta_2)}\begin{bmatrix}\mathbf{f}_2 \\ \mathbf{m}_2\end{bmatrix} + \mathbf{D}_{p4}^{T}\mathbf{R}_{Rz(\beta_3)}^{-1}\mathbf{R}_{R3}\mathbf{R}_{Rz(\beta_4)}\begin{bmatrix}\mathbf{f}_4 \\ \mathbf{m}_4\end{bmatrix}, \tag{33}$$

$$\begin{bmatrix}\mathbf{f}_1 \\ \mathbf{m}_1\end{bmatrix} = \mathbf{D}_{p2mo1}^{T}\mathbf{R}_{R1}\mathbf{R}_{Rz(\beta_2)}\begin{bmatrix}\mathbf{f}_2 \\ \mathbf{m}_2\end{bmatrix}, \tag{34}$$

$$\begin{bmatrix}\mathbf{f}_3 \\ \mathbf{m}_3\end{bmatrix} = \mathbf{D}_{p4mo3}^{T}\mathbf{R}_{R3}\mathbf{R}_{Rz(\beta_4)}\begin{bmatrix}\mathbf{f}_4 \\ \mathbf{m}_4\end{bmatrix}, \tag{35}$$

where $\mathbf{D}_{p2}$, $\mathbf{D}_{p4}$, $\mathbf{D}_{p2mo1}$, and $\mathbf{D}_{p4mo3}$ are 6 × 6 translational matrices, which are given by Eqs. (36) through (39);

$$\boldsymbol{D}_{p2} = \begin{bmatrix} \mathbf{I}_{3\times3} & \begin{bmatrix} 0 & \mathbf{o}_{2m_G}(3,1) & -\mathbf{o}_{2m_G}(2,1) \\ -\mathbf{o}_{2m_G}(3,1) & 0 & \mathbf{o}_{2m_G}(1,1) \\ \mathbf{o}_{2m_G}(2,1) & -\mathbf{o}_{2m_G}(1,1) & 0 \end{bmatrix} \\ \mathbf{0}_{3\times3} & \mathbf{I}_{3\times3} \end{bmatrix}, \tag{36}$$

$$\mathbf{D}_{p4} = \begin{bmatrix} \mathbf{I}_{3\times3} & \begin{bmatrix} 0 & \mathbf{o}_{4m_G}(3,1) & -\mathbf{o}_{4m_G}(2,1) \\ -\mathbf{o}_{4m_G}(3,1) & 0 & \mathbf{o}_{4m_G}(1,1) \\ \mathbf{o}_{4m_G}(2,1) & -\mathbf{o}_{4m_G}(1,1) & 0 \end{bmatrix} \\ \mathbf{0}_{3\times3} & \mathbf{I}_{3\times3} \end{bmatrix}. \tag{37}$$

$$\mathbf{D}_{p2mo1} = \begin{bmatrix} \mathbf{I}_{3\times3} & \begin{bmatrix} 0 & \mathbf{o}_{2m_o1}(3,1) & -\mathbf{o}_{2m_o1}(2,1) \\ -\mathbf{o}_{2m_o1}(3,1) & 0 & \mathbf{o}_{2m_o1}(1,1) \\ \mathbf{o}_{2m_o1}(2,1) & -\mathbf{o}_{2m_o1}(1,1) & 0 \end{bmatrix} \\ \mathbf{0}_{3\times3} & \mathbf{I}_{3\times3} \end{bmatrix}, \tag{38}$$

$$\mathbf{D}_{p4mo3} = \begin{bmatrix} \mathbf{I}_{3\times3} & \begin{bmatrix} 0 & \mathbf{o}_{4m_o3}(3,1) & -\mathbf{o}_{4m_o3}(2,1) \\ -\mathbf{o}_{4m_o3}(3,1) & 0 & \mathbf{o}_{4m_o3}(1,1) \\ \mathbf{o}_{4m_o3}(2,1) & -\mathbf{o}_{4m_o3}(1,1) & 0 \end{bmatrix} \\ \mathbf{0}_{3\times3} & \mathbf{I}_{3\times3} \end{bmatrix}. \tag{39}$$

$\mathbf{o}_{2m_o1}$ denotes the normalized coordinates of point o_2 with respect to o_1-$x_1y_1z_1$ in a deformed condition of the GSRJ, and $\mathbf{o}_{4m_o3}$ denotes the normalized coordinates of point o_{4m} with respect to o_3-$x_3y_3z_3$ in a deformed condition of the GSRJ, as given by Eqs. (40) and (41), respectively; $\mathbf{O}_{G_3}$ denotes the normalized coordinates of O_G with respect to o_3-$x_3y_3z_3$.

$$\mathbf{o}_{2m_o1} = \mathbf{R}_{z(\beta_1)}\mathbf{R}_G\mathbf{o}_{2_G} + \mathbf{R}_{z(\beta_1)}\mathbf{d}_G + \boldsymbol{O}_{G_o1}, \tag{40}$$

$$\mathbf{o}_{4m_o3} = \mathbf{R}_{z(\beta_3)}\mathbf{R}_G\mathbf{o}_{4_G} + \mathbf{R}_{z(\beta_3)}\mathbf{d}_G + \mathbf{O}_{G_o3}, \tag{41}$$

$$\mathbf{O}_{G_o3} = \mathbf{R}_{z(\beta_3)}\begin{bmatrix} l_4\cos\alpha_4 + h_1 + t\sin\alpha_3/2 + b_2 + t\sin\alpha_4 \\ -l_4\sin\alpha_2 + b_4 \\ 0 \end{bmatrix}. \tag{42}$$

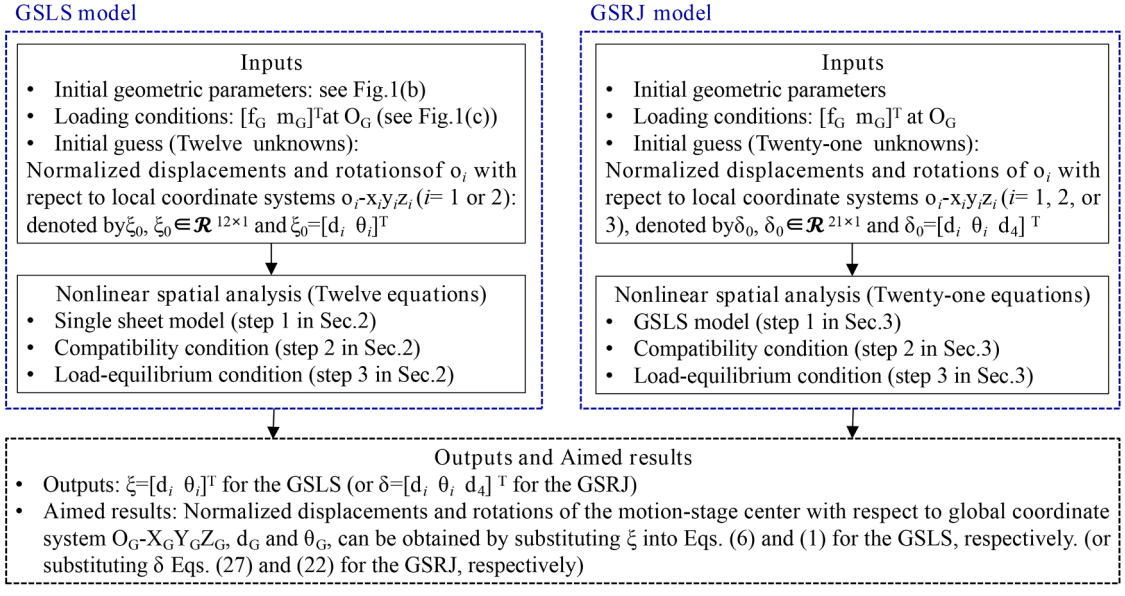


Fig. 3. The modeling procedure for the GSLS model and GSRJ model.

Table 1
Geometric parameters of the asymmetric GSRJ. (Length unit: mm).

	Parameters	Values		Parameters	Values
T	Sheet thickness	0.5	B_1, B_3	Height of the rigid block	B_1= 20, B_3= 20
L_j	Sheet length for sheet-j_A and sheet-j_B	L_1= 50, L_2= 30, L_3= 60, L_4= 30,	B_2, B_4	Horizontal distance between o_2 and O_G, o_4 and O_G.	B_2= 30, B_4= 30
U	Sheet width	10	H_1	Height of the motion stage	10
α_j	Tilt angle for sheet-j_A and sheet-j_B	α_1= 40°, α_2=10° α_3= 40°, α_4= 30°	H_2	Thickness of the sandwich interconnection (or space)	0 to 50 with a step of 10

$\mathbf{R}_{R1}$, $\mathbf{R}_{R3}$, and $\mathbf{R}_{Rz(\beta j)}$ are 6 × 6 rotational matrices, as given by Eq. (43).

$$\mathbf{R}_{R1}=\begin{bmatrix}\mathbf{R}_1 & \mathbf{0}_{3\times3}\\ \mathbf{0}_{3\times3} & \mathbf{R}_1\end{bmatrix},\ \mathbf{R}_{R3}=\begin{bmatrix}\mathbf{R}_3 & \mathbf{0}_{3\times3}\\ \mathbf{0}_{3\times3} & \mathbf{R}_3\end{bmatrix},\ \mathbf{R}_{Rz(\beta_j)}=\begin{bmatrix}\mathbf{R}_1 & \mathbf{0}_{3\times3}\\ \mathbf{0}_{3\times3} & \mathbf{R}_1\end{bmatrix} \tag{43}$$

We use $\mathbf{f}_{jA}$ and $\mathbf{m}_{jA}$ to denote the loads loading at o_{jA} with respect to o_{jA}-$x_{jA}y_{jA}z_{jA}$. Each leg consists of two parallel parameterized lumped-compliance sheets, so the load-equilibrium condition of each leg is given by Eq. (44).

$$\begin{bmatrix}\mathbf{f}_j\\ \mathbf{m}_j\end{bmatrix}=\mathbf{D}_{pAoj}^{T}\begin{bmatrix}\mathbf{f}_{jA}\\ \mathbf{m}_{jA}\end{bmatrix}+\mathbf{D}_{pBoj}^{T}\begin{bmatrix}\mathbf{f}_{jB}\\ \mathbf{m}_{jB}\end{bmatrix}, \tag{44}$$

where $\mathbf{D}_{pAoj}$ and $\mathbf{D}_{pBoj}$ denote the translational matrices, as given by Eq. (45); $\mathbf{o}_{jAm_oj}=\mathbf{R}_j\mathbf{o}_{jA_oj}+\mathbf{d}_j$ and $\mathbf{o}_{jBm_oj}=\mathbf{R}_j\mathbf{o}_{jB_oj}+\mathbf{d}_j$; $\mathbf{o}_{jA_oj}=[0,\ 0,\ (h_2+u)/2]^T$ and $\mathbf{o}_{jB_oj}=[0,\ 0,\ -(h_2+u)/2]^T$.

$$\mathbf{D}_{pAoj}=\begin{bmatrix}\mathbf{I}_{3\times3} & \begin{bmatrix}0 & \mathbf{o}_{jAm_oj}(3,1) & -\mathbf{o}_{jAm_oj}(2,1)\\ -\mathbf{o}_{jAm_oj}(3,1) & 0 & \mathbf{o}_{jAm_oj}(1,1)\\ \mathbf{o}_{jAm_oj}(2,1) & -\mathbf{o}_{jAm_oj}(1,1) & 0\end{bmatrix}\\ \mathbf{0}_{3\times3} & \mathbf{I}_{3\times3}\end{bmatrix}, \tag{45}$$

$$\mathbf{D}_{pBoj}=\begin{bmatrix}\mathbf{I}_{3\times3} & \begin{bmatrix}0 & \mathbf{o}_{jBm_oj}(3,1) & -\mathbf{o}_{jBm_oj}(2,1)\\ -\mathbf{o}_{jBm_oj}(3,1) & 0 & \mathbf{o}_{jBm_oj}(1,1)\\ \mathbf{o}_{jBm_oj}(2,1) & -\mathbf{o}_{jBm_oj}(1,1) & 0\end{bmatrix}\\ \mathbf{0}_{3\times3} & \mathbf{I}_{3\times3}\end{bmatrix}. \tag{46}$$

A modeling procedure of the GSLS and GSRJ is shown in Fig. 3.

4. Stiffness analysis and parametric analysis

The nonlinear spatial analytical model for the GSRJ is verified against FEA conducted in COMSOL 5.0. Building on this validation, a study on the normalized stiffness ratio between the GSRJ and its counterparts is performed. A parametric analysis is carried out to evaluate the behavior of both asymmetric and symmetric GSRJs. Finally, prototypes are manufactured, and their experimental results are compared with those from both the analytical model and FEA to complete the verification framework.

4.1. Analytical model verification of the GSRJ

In the FEA model, rigid parts do not require mesh sizing but should be set as "rigid domains" in COMSOL 5.0. The elastic sheets are made of aluminum, with a Young's modulus of 69 × 10^9 (Pa) and a Poisson's ratio of 0.3. Details of the FEA process can be found in Appendix B of [49].

The geometric parameters of GSRJ are shown in Table 1, and its model is shown in Fig. 4(c). When M_{xG}=M_{yG}=0.01 (N·m) and M_{zG}= 0.03 (N·m), and the thickness of the sandwich interconnection ranges from 0 to 50 (mm) with a step of 10 (mm), the analytical results (denoted by Ana) and FEA results (denoted by FEA) of the motion stage are shown in Figs. 4(a) and (b). The average errors between the FEA and analytical results are all <6.4%. The results indicate that out-of-plane displacement and rotations—D_{zG}, θ_{xG}, and θ_{yG}—decrease significantly with increasing thickness of the sandwich interconnection. The in-plane displacements and rotation—D_{xG}, D_{yG}, and θ_{zG}—remain unchanged, indicating that the sandwich interconnection does not affect in-plane stiffness. Its maximum deformation before yield stress is shown in Appendix A.

It has been found that the errors between the analytical model and FEA for all displacement results are acceptable when the sheet's translational displacement is <10% of its length, the rotation is <0.1 rad, and the aspect ratios of the elastic sheets are slightly violated (i.e., aspect ratios < 10, as listed in Table 1). When the sheet's translational displacement exceeds 10% of its length, the rotation exceeds 0.1 rad,

Table 2
Modelling sensitivity to the assumptions.

Assumptions: deformation <10%, rotation <0.1 rad	Assumption: aspect ratios >10	The sensitivity of the results to the assumptions
Satisfied	Satisfied	Results demonstrate excellent agreement between the analytical model and FEA, with all errors below 4%.
Violated	Satisfied	In-plane analytical results (OXY plane) agree well with the FEA; however, the out-of-plane analytical results deviate significantly with the FEA.
Satisfied	Violated	Errors for all the results are acceptable, with errors within 6.5%.
Violated	Violated	The modelling accuracy of both the in-plane and out-of-plane results is significantly affected.

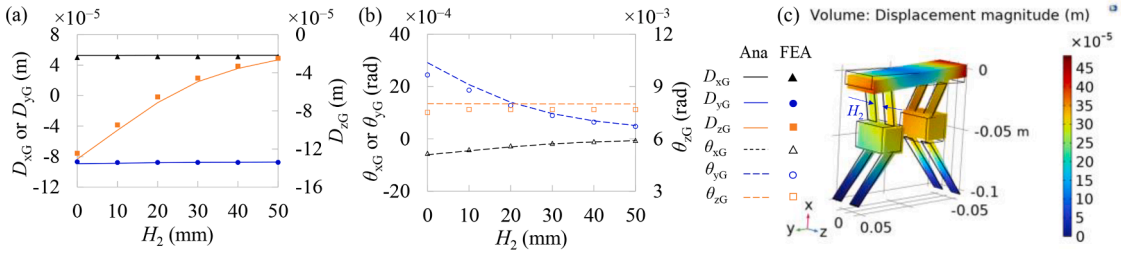


Fig. 4. The analytical and FEA results of the GSRJ versus increasing thickness of the sandwich interconnection H_2. (a) Analytical and FEA displacements; (b) Analytical and FEA rotations; (c) FEA simulation when H_2 =10 (mm).

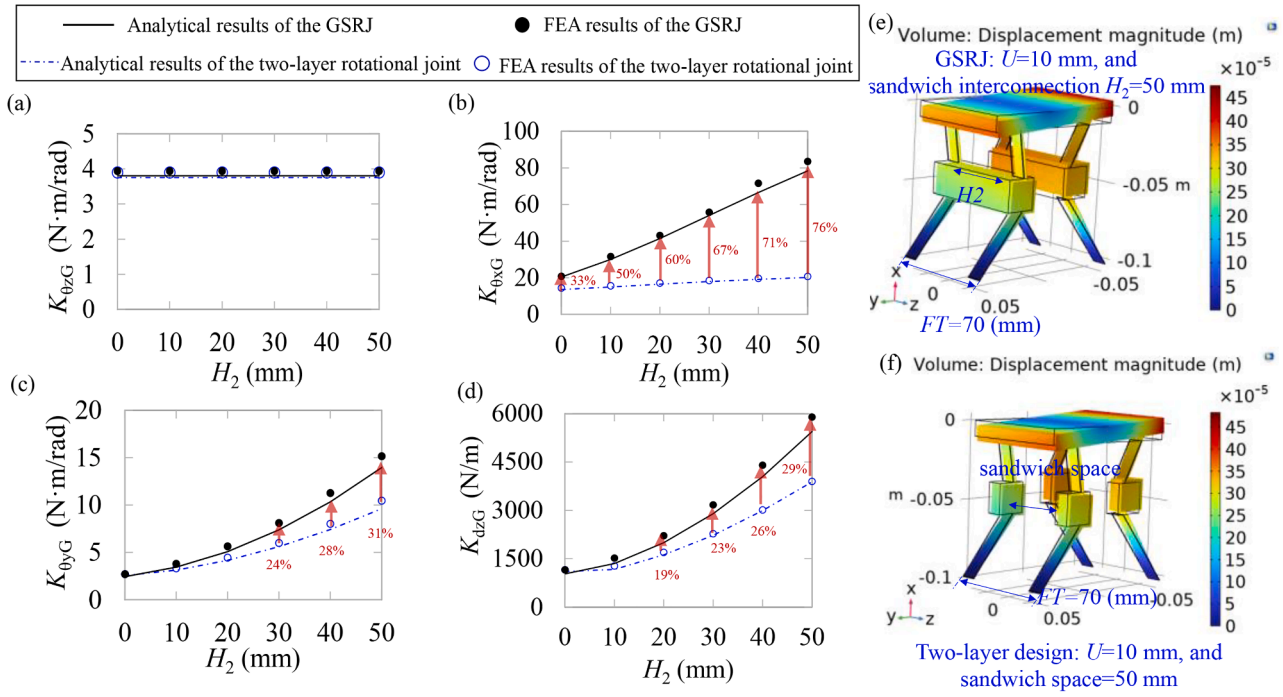


Fig. 5. The stiffness comparison between the GSRJ and the two-layer rotational joint versus increasing thickness of the sandwich interconnection H_2. (a) Primary motion (rotational) stiffness $K_{\theta zG}$; (b) Out-of-plane stiffness $K_{\theta xG}$; (c) Out-of-plane stiffness $K_{\theta yG}$; (d) Out-of-plane stiffness K_{dzG}; (e) The GSRJ; (f) The counterpart model: two-layer rotational joint.

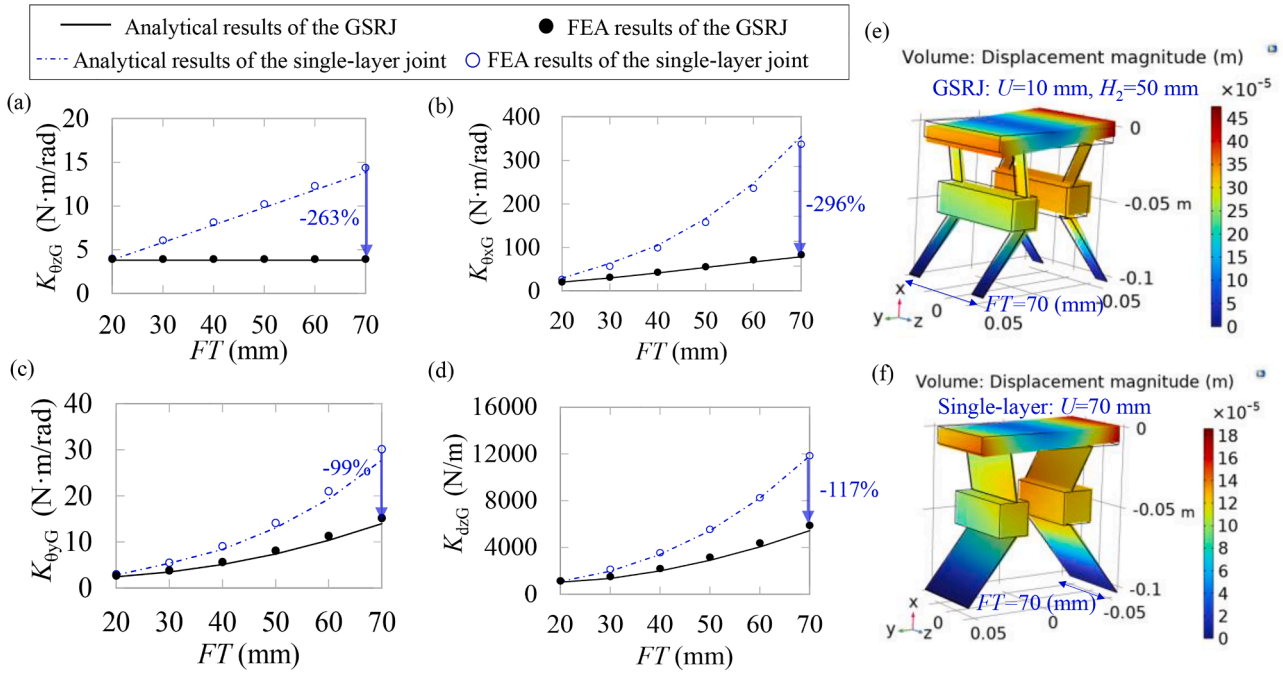


Fig. 6. The stiffness comparison between the GSRJ and the single-layer rotational joint versus increasing ***FT***. (a) Primary motion (rotational) stiffness $K_{\theta zG}$; (b) Out-of-plane stiffness $K_{\theta xG}$; (c) Out-of-plane stiffness $K_{\theta yG}$; (d) Out-of-plane stiffness K_{dzG}; (e) The GSRJ; (f) The counterpart model: single-layer rotational joint.

and the aspect ratios are greater than 10, only the modelling accuracy of the out-of-plane results is significantly affected. When the sheet's translational displacement exceeds 10% of its length, the rotation exceeds 0.1 rad, and the aspect ratios are <10, the modelling accuracy of both the in-plane and out-of-plane results is significantly affected. The sensitivity of the results to all the assumptions is also summarized in Table 2.

4.2. *Stiffness analysis for GSRJ and comparisons with counterpart designs*

The stiffness of the GSRJ (Table 1) is evaluated by comparing it against two types of counterparts, which refer to the work of [81,82]. The stiffness ratio is employed to further investigate the stiffness characteristics across various design configurations.

Table 3
Geometric parameters of the GSRJ and single-layer rotational joint under the same out-of-plane footprint. (Unit: mm).

	Parameters	Values for GSRJ	Values for the single-layer rotational joint
FT	Out-of-plane footprint, $FT=2U+H_2$	20 to 70 with a step of 10	
H_2	Thickness of the sandwich	$FT-2U$	0
U	Sheet width	10	FT

(1) Case 1: Stiffness comparison among the GSRJ, two-layer joint, and single-layer rotational joint under an identical out-of-plane footprint

The two-layer rotational joint has no sandwich interconnection and shares the same geometric parameters as the GSRJ, as illustrated in Fig. 5(f). This ensures that the stiffness comparison between the GSRJ and the two designs is conducted under the same out-of-plane footprint. This footprint, denoted by *FT*, is equal to $2U+H_2$. The nonlinear spatial analytical model of the two-layer rotational joint is detailed in Appendix B. $K_{\theta zG}$ is calculated by applying M_{zG} of 0.1 (N·m) and 0.12 (N·m) to the motion stage, and the results are presented in Fig. 5(a). $K_{\theta zG}$ of both designs remains constant with increasing thickness of the sandwich interconnection. Then, M_{zG} held constant at 0.03 (N·m), $K_{\theta xG}$ (or $K_{\theta yG}$) is obtained by applying M_{xG} (or M_{yG}) = 0.01 (N·m) and 0.012 (N·m); K_{dzG} is calculated by applying F_{zG} = 0.1 (N) and 0.12 (N). In Fig. 5 (b), $K_{\theta xG}$ of both designs increases significantly with the increase of H_2, while $K_{\theta yG}$ and K_{dzG} in Figs. 5(c) and (d) show a more gradual increase. When H_2 = 50 (mm), $K_{\theta xG}$, $K_{\theta yG}$, and K_{dzG} increase by 76%, 31%, and 29%, respectively.

The stiffness of the GSRJ is compared with that of the single-layer rotational joint under an identical out-of-plane footprint. The single-layer rotational joint is shown in Fig. 6(f). The geometric parameters of the GSRJ and the single-layer rotational joint are slightly different, as detailed in Table 3. All other parameters are identical to those listed in Table 1.

M_{zG} is held constant at 0.1 (N·m), and the DoF and the out-of-plane stiffness of the two designs are calculated following the same approach described earlier. These results indicate that both the rotational stiffness and out-of-plane stiffness of the single-layer rotational joint increase significantly with increasing *FT*. As demonstrated in Fig. 6(a), the GSRJ maintains stable primary motion (rotational) stiffness, while the single-layer rotational joint shows a progressive increase in stiffness. In Figs. 6 (b) to (d), the out-of-plane stiffness of the GSRJ increases less than that of the single-layer rotational joint under the same geometric conditions, indicating that the sheet width influences stiffness more significantly than H_2 does.

On the other hand, we compared their out-of-plane stiffness changes with the increase of primary moments. H_2 is equal to 50 (mm), and U of the single-layer rotational joint is 20 (mm), while the remaining geometric parameters of the GSRJ and its two counterparts are identical to those listed in Table 1. The out-of-plane stiffness for each joint is calculated as follows. Primary rotations (θ_{zG}) range from −0.06 (rad) to 0.06 (rad) with a step of 0.02 (rad) in the analytical and FEA models. For each θ_{zG}, $K_{\theta xG}$ is derived from a very small M_{xG} of 0.001 (N·m) [49]. $K_{\theta yG}$ can be obtained using an analogous procedure. K_{dzG} is calculated by applying a very small F_{zG} of 0.001 (N). The stiffness change of $K_{\theta xG}$ is defined by Eq. (47).

$$\frac{\left|K_{\theta xG_0}-K_{\theta xG}\right|_{Max}}{K_{\theta xG_0}}\times 100\%, \tag{47}$$

where $K_{\theta xG_0}$ denotes $K_{\theta xG}$ when θ_{zG} =0; $|K_{\theta xG_0}-K_{\theta xG}|_{Max}$ denotes the maximum absolute deviation of $K_{\theta xG}$ from $K_{\theta xG_0}$; all other stiffness changes can be solved using the same procedure.

Fig. 7 illustrates the out-of-plane stiffness and stiffness changes for the GSRJ and its two counterparts. The average errors between the analytical results and the corresponding FEA results for the GSRJ, two-layer GSRJ, and single-layer GSRJ are 6.8%, 8.7% and 20%, respectively. Note that some large errors can be explained by the conclusions in Table 2. The stiffness changes of the GSRJ are not less than those of the two counterparts. Moreover, in this design configuration, the out-of-plane stiffness slightly increases with the increase of the clockwise θ_{zG}. Appendix C presents the stiffness changes of two specific designs of the GSRJ, and all out-of-plane stiffness decreases with the increasing θ_{zG}. Fig. C5 depicts the out-of-plane stiffness and corresponding stiffness changes for the GSRJ ($\alpha_1=\alpha_2$, $\alpha_3=\alpha_4$) and its counterparts. The average errors for the GSRJ ($\alpha_1=\alpha_2$, $\alpha_3=\alpha_4$), two-layer GSRJ ($\alpha_1=\alpha_2$, $\alpha_3=\alpha_4$), and single-layer GSRJ ($\alpha_1=\alpha_2$, $\alpha_3=\alpha_4$) are 7.9%, 15.9% and 9%, respectively. Based on both analytical and FEA results as demonstrated in Figs. 7 and C5, although out-of-plane stiffness changes of the GSRJ are not the smallest among the evaluated three designs, the average out-of-plane stiffness of the GSRJ is still significantly (over 50%) higher than the other two counterpart designs. Fig. C10 illustrates the out-of-plane

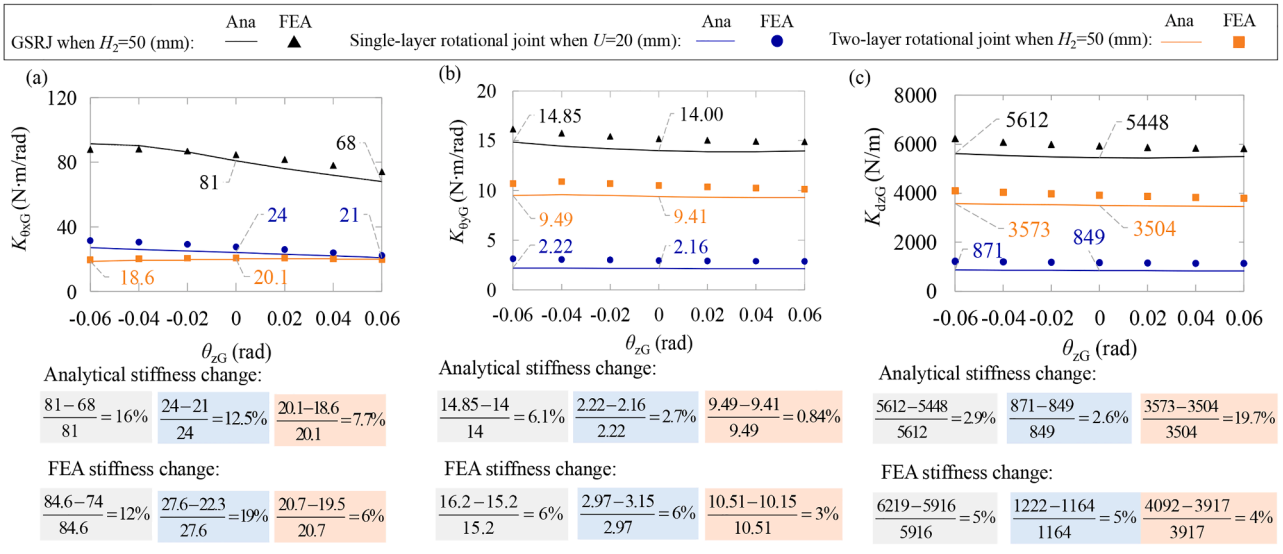


Fig. 7. The stiffness analysis among the GSRJ, the two-layer rotational joint, and the single-layer rotational joint with the increase of primary rotations. (a-c) Analytical and FEA results of $K_{\theta xG}$, $K_{\theta yG}$, K_{dzG}, and their stiffness changes.

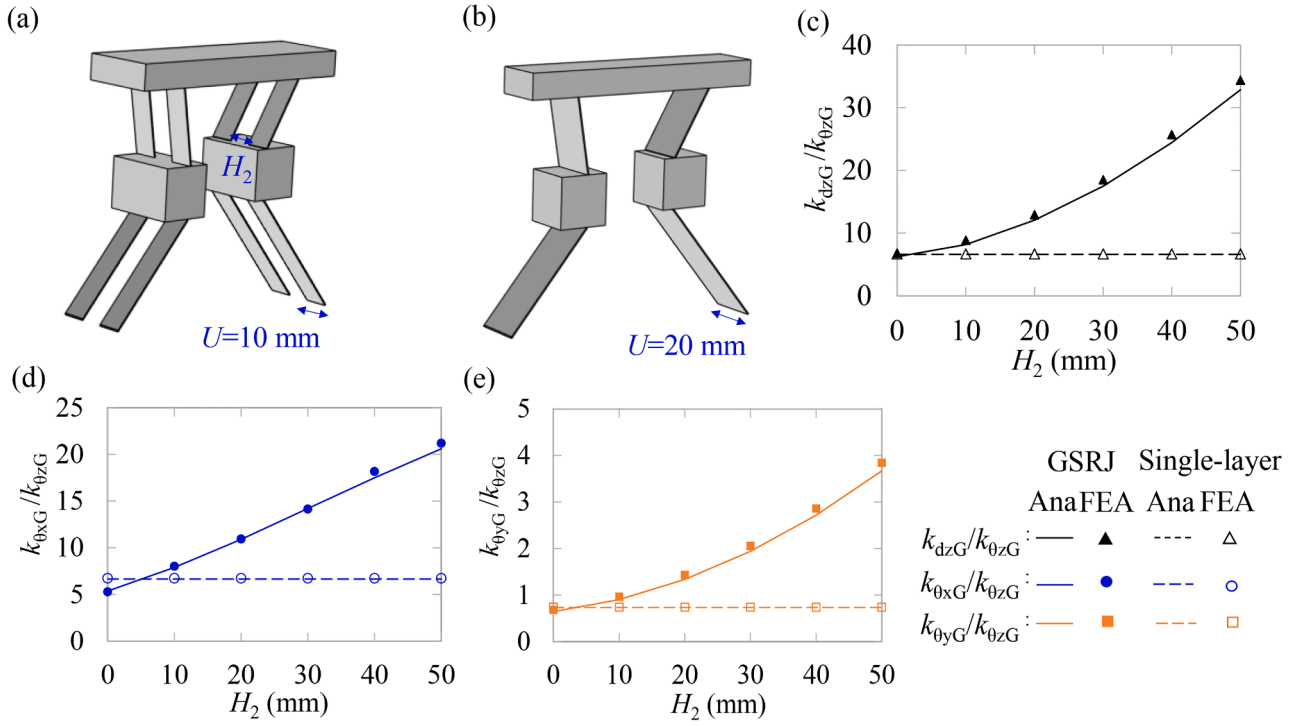


Fig. 8. Stiffness-ratio comparison between the GSRJ and the single-layer rotational joint. (a) GSRJ model (only H2 ranges from 0 to 50 mm); (b) The counterpart model: single-layer rotational joint; (c-e) Normalized stiffness ratios $k_{dzG}/k_{\theta zG}$, $k_{\theta xG}/k_{\theta zG}$, $k_{\theta yG}/k_{\theta zG}$ of the two joints, respectively.

stiffness and corresponding stiffness changes for the GSTJ and its counterparts. The average errors for the GSTJ, two-layer GSTJ, and single-layer GSTJ are 2.3%, 4.1% and 4.6%, respectively. GSTJ achieves the minimum stiffness changes specifically for $K_{\theta x}$ and K_{dz}.

In [81], the slow degradation of the out-of-plane stiffness in sandwich PFMs is well-explained by the reduced elastokinematic terms within the compliance matrix of a single flexure blade. However, this analytical deduction cannot be directly generalized to explain the stiffness changes observed in the GSRJ. The deformation behavior of the GSRJ is heavily dictated by intricate spatial deformation compatibility conditions, rather than a simple superposition of individual blade compliances. It is therefore challenging to provide a comprehensive mechanistic explanation for these highly specific stiffness variation differences at this stage, and the geometric parameters for the GSRJ should be selected with careful consideration, as its stiffness changes may not be minimal. We hypothesize that this behavior arises from the complex spatial nonlinear coupling effects during deformation, which remains an open topic for our future work.

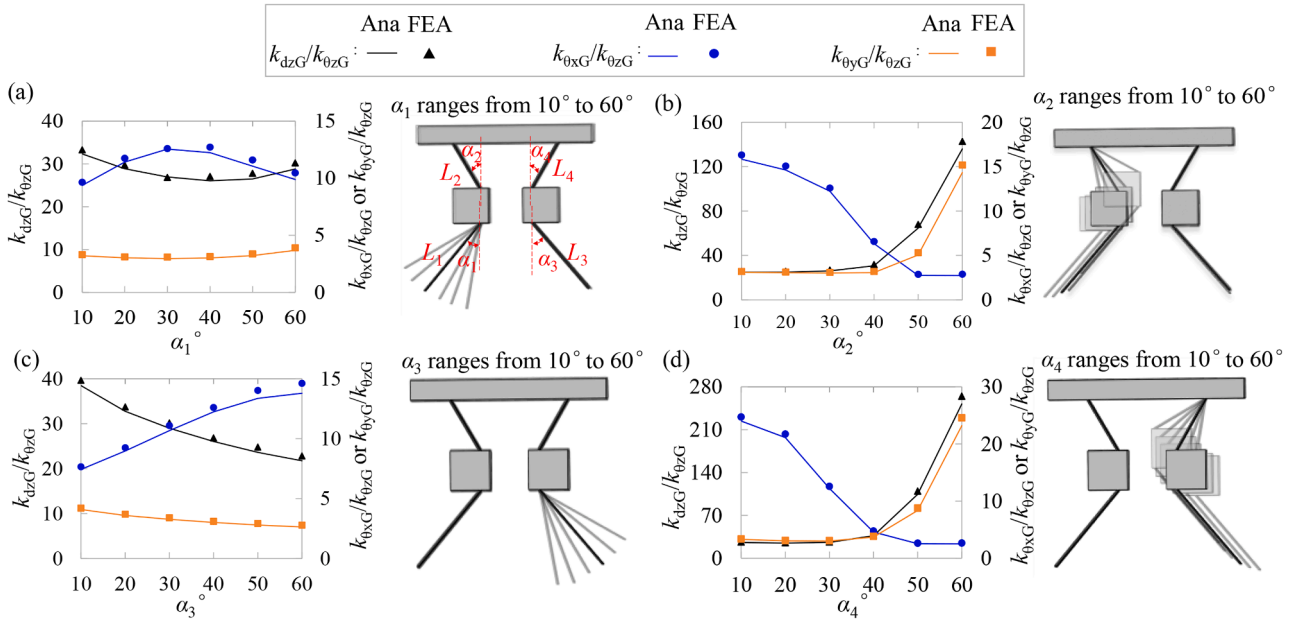


Fig. 9. The effects of sheet-tilt angles on normalized stiffness ratios. (a) Effects of α_1 on the normalized stiffness ratios (α_3=40°, α_2=α_4=30°); (b) Effects of α_2 on the normalized stiffness ratios (α_1=α_3=40°, α_4=30°); (c) Effects of α_3 on the normalized stiffness ratios (α_1=40°, α_2=α_4=30°); (d) Effects of α_4 on the normalized stiffness ratios (α_2=30°, α_1=α_3=40°).

(2) Case 2: stiffness ratio comparison under the same out-of-plane footprint of the sheets

The following analysis is conducted under the condition that the out-of-plane footprint of the sheets remains constant, i.e., the total sheet width is kept the same, as illustrated in Figs. 8(a) and (b). Additionally, the geometric parameters of the GSRJ and the single-layer rotational joint are identical except for H_2 and U. This ensures that both designs achieve the same in-plane rotational stiffness, enabling a fair comparison of their normalized stiffness ratios—that is, the ratio of the normalized out-of-plane stiffness to the normalized in-plane rotational stiffness—as shown in Fig. 8(c) to (e). Thus, the normalized stiffness ratios are expressed in dimensionless form and are used to evaluate the influence of H_2 on the out-of-plane stiffness. Compared to the single-layer rotational joint, the GSRJ exhibits a significant increase in the normalized stiffness ratios with increasing H_2.

The GSRJ (α_1=α_2, α_3=α_4) and GSTJ are two specific configurations within the GSRJ framework. The verification of their analytical models via FEA, along with a stiffness comparison with their respective counterparts, is detailed in Appendix C. These results collectively demonstrate the accuracy of the proposed nonlinear spatial analytical model.

4.3. Parametric analysis of GSRJ

In this section, the influence of sheet-tilt angles and sheet length on normalized stiffness ratios is studied in the GSRJ, with comparisons between analytical models (Ana) and FEA results.

(1) Asymmetric features of the GSRJ

The symmetric parameters of the GSRJ are first specified as follows: L_1=L_3=50 (mm), L_2=L_4=30 (mm), B_1=B_3=20 (mm), B_2=B_4=30 (mm), α_1=α_3=40°, and α_2=α_4=30° The impact of the sheet angle on the stiffness ratios of the GSRJ is investigated as below. We varied each sheet angle individually, keeping the other geometric parameters constant. The normalized stiffness ratios of the asymmetric and symmetric joints are compared under a constant global bending moment of M_{ZG}=0.2 (N·m) and H_2=50 (mm). In practical applications, rotational joints primarily bear the moment in the primary DoF direction. Therefore, the following stiffness ratios are calculated under a constant M_{zG}. The out-of-plane stiffness for each discretion can be calculated as we did in Fig. 7.

In Fig. 9, each subplot investigates how the normalized stiffness ratios ($k_{dzG}/k_{\theta zG}$, $k_{\theta xG}/k_{\theta zG}$, and $k_{\theta yG}/k_{\theta zG}$) change as α_1, α_2, α_3, or α_4 varies. In Figs. 9(a) and (c), $k_{dzG}/k_{\theta zG}$ and $k_{\theta xG}/k_{\theta zG}$ are highly sensitive to variations in α_1 and α_3, whereas $k_{\theta yG}/k_{\theta zG}$ remains largely unaffected by such variations. The parameters α_1 and α_3 exert opposite effects on the ratios $k_{dzG}/k_{\theta zG}$ and $k_{\theta xG}/k_{\theta zG}$. An optimal balance for simultaneously achieving high $k_{dzG}/k_{\theta zG}$ and $k_{\theta xG}/k_{\theta zG}$ ratios is found at α_1 = 20° and α_3≈32°In Fig. 9(b), $k_{dzG}/k_{\theta zG}$ (or $k_{\theta xG}/k_{\theta zG}$, or $k_{\theta yG}/k_{\theta zG}$) has the same trend as that in Fig. 9(d) and their values are different. As α_2 or α_4 increases, both $k_{dzG}/k_{\theta zG}$ and $k_{\theta yG}/k_{\theta zG}$ increase, with $k_{dzG}/k_{\theta zG}$ exhibiting a markedly greater rise (from 24 to 135 vs. 3 to 15 for $k_{\theta yG}/k_{\theta zG}$). Conversely, $k_{\theta xG}/k_{\theta zG}$ decreases from 15 to 2. A design compromise is α_2 = 42° and α_4≈40°, though they can be adjusted according to specific loading conditions and performance requirements.

On the other hand, we study how the sheet length affects the normalized stiffness ratios of the GSRJ. Each sheet length is varied individually (Fig. 10(a)), keeping the other geometric parameters constant. As illustrated in Figs. 10(b) and (d), stiffness ratios exhibit a consistent trend whether L_1 or L_3 is increased. The slight value differences may result from the prescribed M_{zG}. $k_{dzG}/k_{\theta zG}$ and $k_{\theta xG}/k_{\theta zG}$ are more sensitive to the changes in L_1 and L_3, respectively. When L_1 or L_3 is equal to 50 (mm), $k_{\theta xG}/k_{\theta zG}$ reaches its maximum of 12. However, $k_{dzG}/k_{\theta zG}$ and $k_{\theta yG}/k_{\theta zG}$ remain relatively low at 26 and 3, respectively. Increasing L_1 or L_3 to 80 (mm) results in a moderate decline of $k_{\theta xG}/k_{\theta zG}$ to 8, yet yields considerably higher values for $k_{dzG}/k_{\theta zG}$ (41) and $k_{\theta yG}/k_{\theta zG}$ (5). Therefore, setting either L_1 or L_3 to 80 (mm) is the optimal choice for maximizing $k_{dzG}/k_{\theta zG}$ and $k_{\theta yG}/k_{\theta zG}$ with a minimal reduction in $k_{\theta xG}/k_{\theta zG}$.

Similarly, a consistent trend is observed in Figs. 10(c) and (e) when either L_2 or L_4 is increased. $k_{dzG}/k_{\theta zG}$ and $k_{\theta yG}/k_{\theta zG}$ are more sensitive to the changes in L_2 and L_4. When L_2 is 60 (mm), $k_{\theta yG}/k_{\theta zG}$ reaches its maximum of 40, despite a relatively lower $k_{dzG}/k_{\theta zG}$ of 180. In comparison, increasing L_2 to 70 (mm) reduces $k_{\theta yG}/k_{\theta zG}$ to 33 but

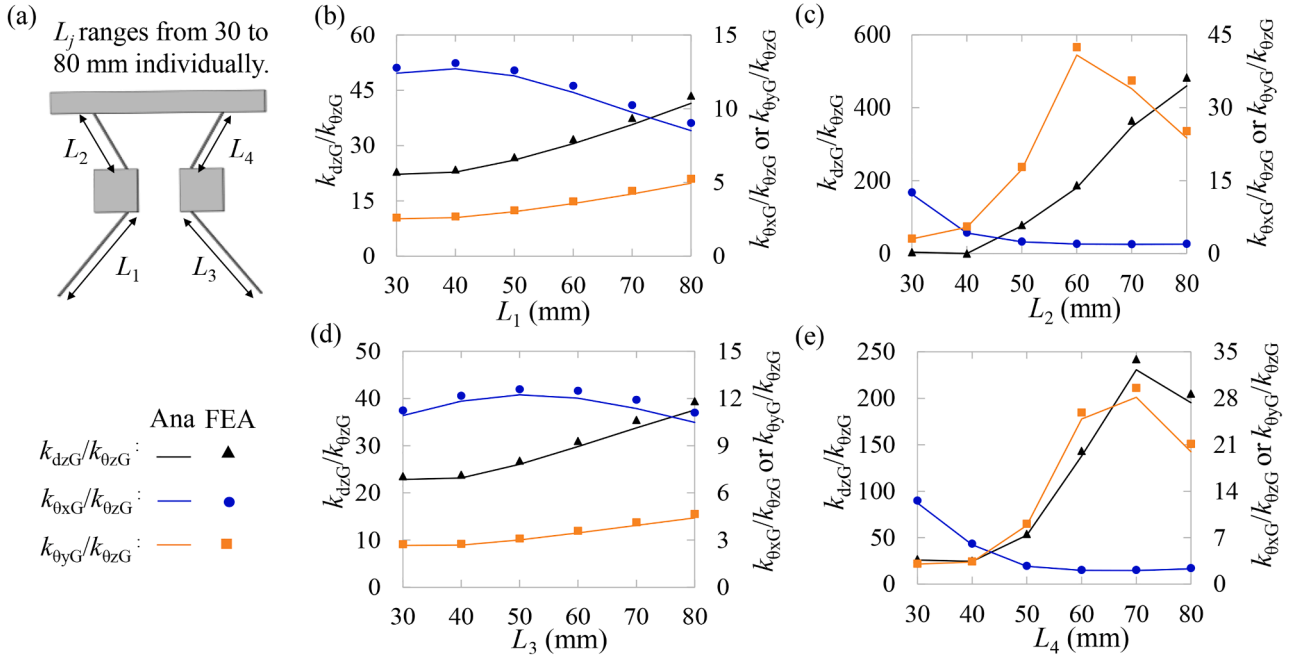


Fig. 10. The effects of sheet length on normalized stiffness ratios. (a) Geometric parameters to be varied for the four study cases (j = 1,2,3 or 4); (b) Effects of L_1 on the normalized stiffness ratios (L_3=50 mm, L_2=L_4=30 mm); (c) Effects of L_2 on the normalized stiffness ratios (L_1=L_3=50 mm, L_4= 30 mm); (d) Effects of L_3 on the normalized stiffness ratios (L_1= 50 mm, L_2=L_4=30 mm); (e) Effects of L_4 on the normalized stiffness ratios (L_1=L_3=50 mm, L_2= 30 mm).

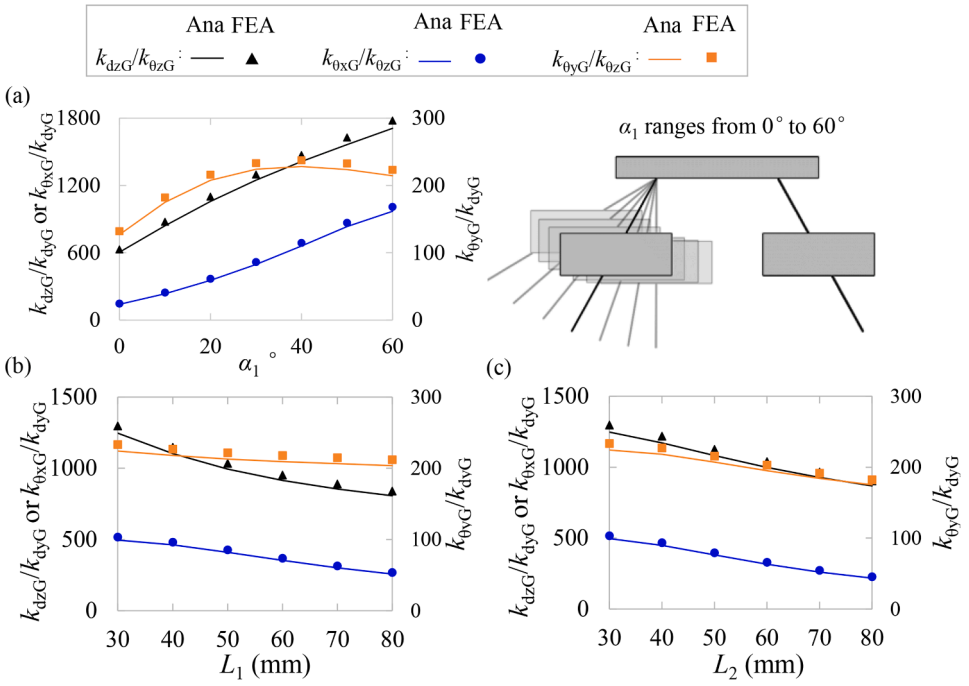


Fig. 11. The effects of the sheet angle and the sheet length on normalized stiffness ratios. (a) Effects of α_1 on the normalized stiffness ratios (α_1=α_2, α_3=α_4=30°); (b) Effects of L_1 on the normalized stiffness ratios (L_2=L_3=L_4=30 (mm)); (c) Effects of L_2 on the normalized stiffness ratios (L_1=L_3=L_4=30 (mm)).

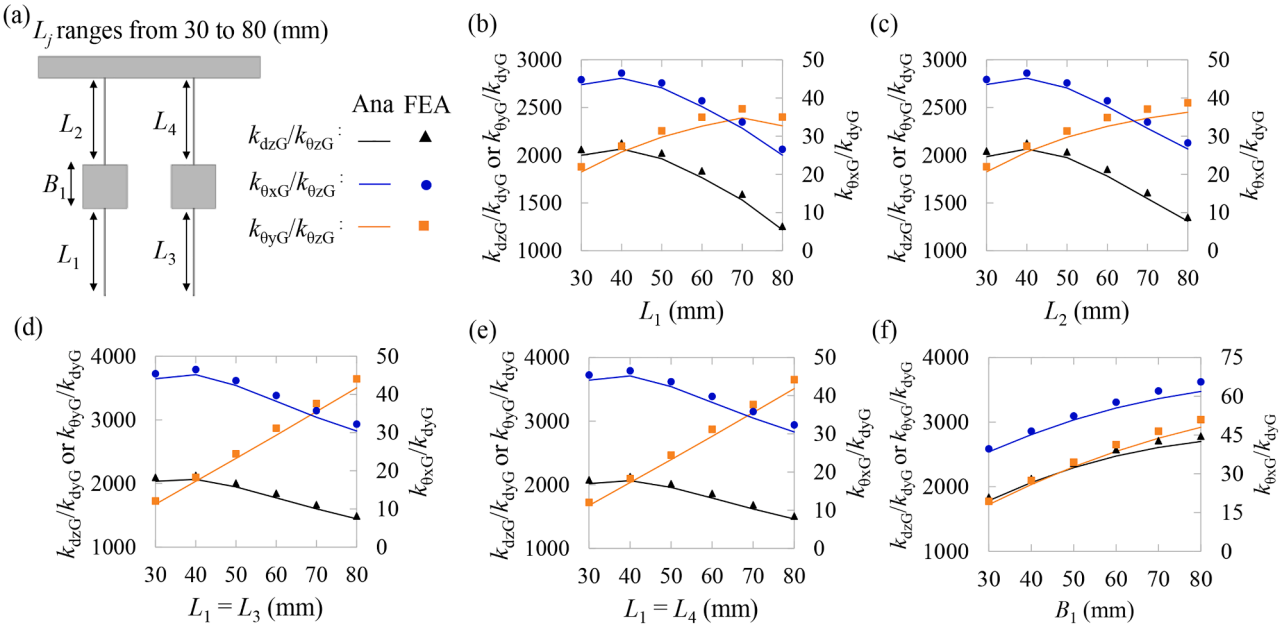


Fig. 12. The effects of sheet length and rigid-block thickness on normalized stiffness ratios. (a) Geometric parameters to be varied for the five study cases (j = 1,2,3 or 4); (b) Effects of L_1 on the normalized stiffness ratios where L_1 ranges from 30 to 80 mm; (c) Effects of L_2 on the normalized stiffness ratios where L_2 ranges from 30 to 80 mm; (d) Combined effects of L_1 and L_3 on the normalized stiffness ratios where L_1 and L_3 ranges from 30 to 80 mm; (e) Combined effects of L_2 and L_4 on the normalized stiffness ratios where L_2 and L_4 ranges from 30 to 80 mm; (f) Effects of B_1 on the normalized stiffness ratios.

significantly increases $k_{dzG}/k_{\theta zG}$ to 347. Therefore, setting L_2 to 75 (mm) is determined to be the optimal choice, as it further prioritizes the maximization of $k_{dzG}/k_{\theta zG}$ while accepting only a minimal additional reduction in $k_{\theta yG}/k_{\theta zG}$. For a related but distinct parameter group, an L_4 value of 70 (mm) is identified as optimal.

In summary, for angle parameters, α_1 and α_3 affect both $k_{dzG}/k_{\theta zG}$ and $k_{\theta xG}/k_{\theta zG}$, but have almost no influence on $k_{\theta yG}/k_{\theta zG}$. In contrast, α_2 and α_4 greatly affect all three stiffness ratios. Regarding sheet length parameters, L_1 and L_3 affect $k_{dzG}/k_{\theta zG}$ (with less impact on the others), while L_2 and L_4 greatly affect $k_{dzG}/k_{\theta zG}$ and $k_{\theta yG}/k_{\theta zG}$ (with less impact on $k_{\theta xG}/k_{\theta zG}$). Therefore, normalized stiffness ratios can be adjusted by tuning the asymmetric parameters, and directional stiffness optimization can be achieved.

(2) Asymmetric features of the GSRJ (α_1=α_2, α_3=α_4)

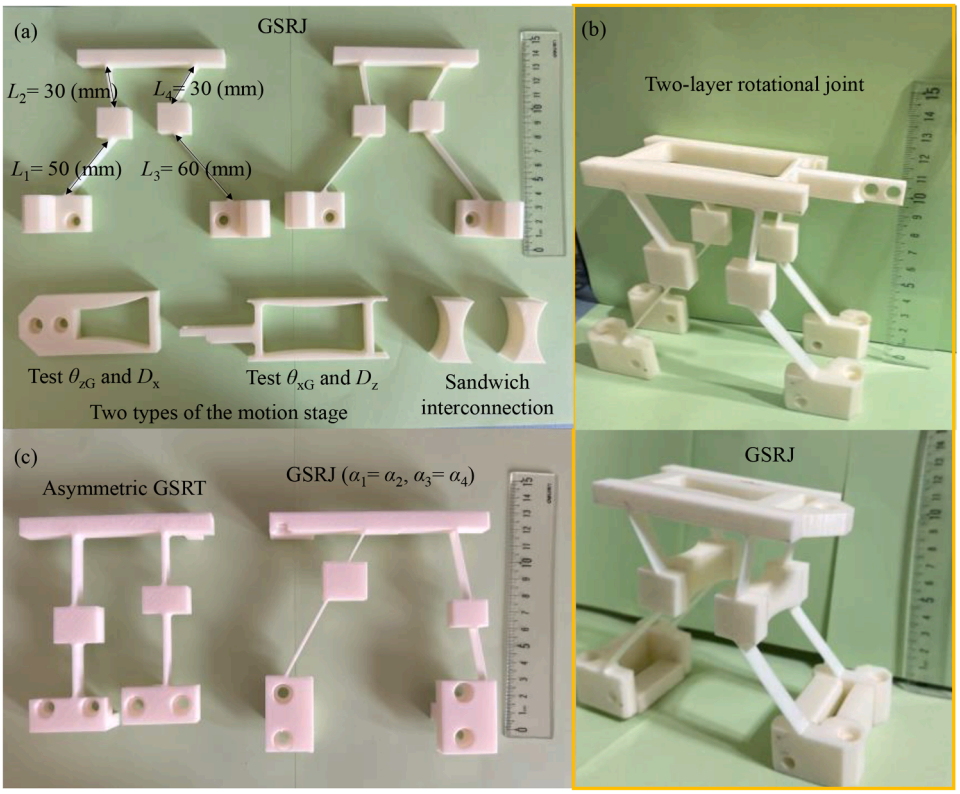


Fig. 13. The parts for fabricating the prototypes. (a) Parts for the GSRJ; (b) Prototype examples: two-layer rotational joint and GSRJ; (c) Some parts of the single-layer GSTJ and GSRJ.

Since the GSRJ (α_1=α_2, α_3=α_4) is a special case of the GSRJ, we investigate its asymmetric characteristics to enable a more comprehensive analysis. The symmetric parameters of the GSRJ (α_1=α_2, α_3=α_4) are L_1=L_2=L_3=L_4=30 (mm), B_1=B_3=20 (mm), B_2=B_4=30 (mm), α_1=α_2=α_3=α_4=30° As shown in Fig. 11(a), $k_{\theta yG}/k_{\theta zG}$ exhibits a slight decrease after an initial rise with the increase of α_1, and the other two ratios show a consistent increase. Therefore, α_1= 60° is the best value for high overall stiffness. In Fig. 11(b) and (c), except for $k_{\theta yG}/k_{\theta zG}$, the other two stiffness ratios are more sensitive to sheet length. All three stiffness ratios decrease with increasing L_1 and L_2. Consequently, maximizing the stiffness ratios requires all parameters L_i (i = 1,2,3,4) to be set to a common minimum value.

(3) Asymmetric features of the GSTJ

In this part, the influence of sheet length on normalized stiffness ratios is studied for the GSTJ. The normalized stiffness ratios of the asymmetric and symmetric joints are compared under a constant global horizontal force of F_{yG} = 0.1 (N) and H_2 = 50 (mm). The stiffness components can be determined as we did above. The symmetric parameters for the GSTJ are L_1=L_3= L_2=L_4= 40 (mm), B_1=B_3= B_2=B_4=20 (mm). Fig. 12(a) indicates the geometric parameters to be varied for this part.

Modifying mirror-symmetric geometric parameters in a GSRJ can produce a consistent trend on stiffness ratios. This is further illustrated by the GSTJ, a specific type of GSRJ. As shown in Fig. 12(b) and (c), the trends of the three normalized stiffness ratios are identical whether L_1 or L_2 is increased. The above analysis confirms that altering any single sheet length in a GSTJ yields the same consistent trend. The ratios k_{dzG}/k_{dyG} and $k_{\theta yG}/k_{dyG}$ decrease with the increase of L_i, whereas $k_{\theta xG}/k_{dyG}$ increases (i = 1, 2, 3 or 4). A comparison of Fig. 12(b) with (d) and (e) reveals that the overall trend related to sheet length remains consistent, when L_1 changes in conjunction with either L_3 or L_4, despite differences in specific values. In Fig. 12(f), all out-of-plane stiffness ratios increase with B_1. However, the rate of increase for $k_{\theta yG}/k_{dyG}$ is greater in Fig. 12 (b), indicating that increasing the sheet length is more effective at raising this value than increasing B_1.

Variations in any individual sheet length exert a uniform effect on the three stiffness ratios. When multiple sheet lengths change concurrently, their combined influence operates in a cumulative manner.

4.4. Manufacture and experiment

For experimental validation, two prototypes (the GSRJ and the two-layer rotational joint) are fabricated and tested, with their results compared against both the analytical and FEA simulation results. The two prototypes share the same geometric parameters, as shown in Table 1, but with a sheet thickness of 1 (mm) and H_2 = 40 (mm). They are printed using a Zortrax M200 plus 3D printer. The 3D printing material is selected to be Z-ULTRAT, whose Young's modulus is 1.85 (GPa) and Poisson's ratio is 0.35. The fill density is set to be 30%. The parts for assembling the GSRJ, as shown in Fig. 13(a), are connected with super glue, with the prototypes shown in Fig. 13(b). The other prototypes can be fabricated similarly, and examples are shown in Fig. 13(c).

As shown in Fig. 14(a), an S-type tension and compression force sensor, with a maximum capacity of 2 (kg) and an accuracy of 0.03% (i.e., 6×10^{-4} kg), is used to exert a series of forces on point o_E of the motion stage. The force sensor is mounted on XYZ positioning stages with an accuracy of 0.01 (mm). The forces applied at o_E are then transformed to point O_G with respect to O_G-$X_GY_GZ_G$ using Eq. (48). The layer resolution of the 3D printer is 90 to 390 (μm), and 90 (μm) is selected for the prototypes. The accuracy of L400-C universal force control instrument is 1‰ (N). The experiments are conducted at room temperature to avoid the influence of temperature on the prototype's Young's modulus.

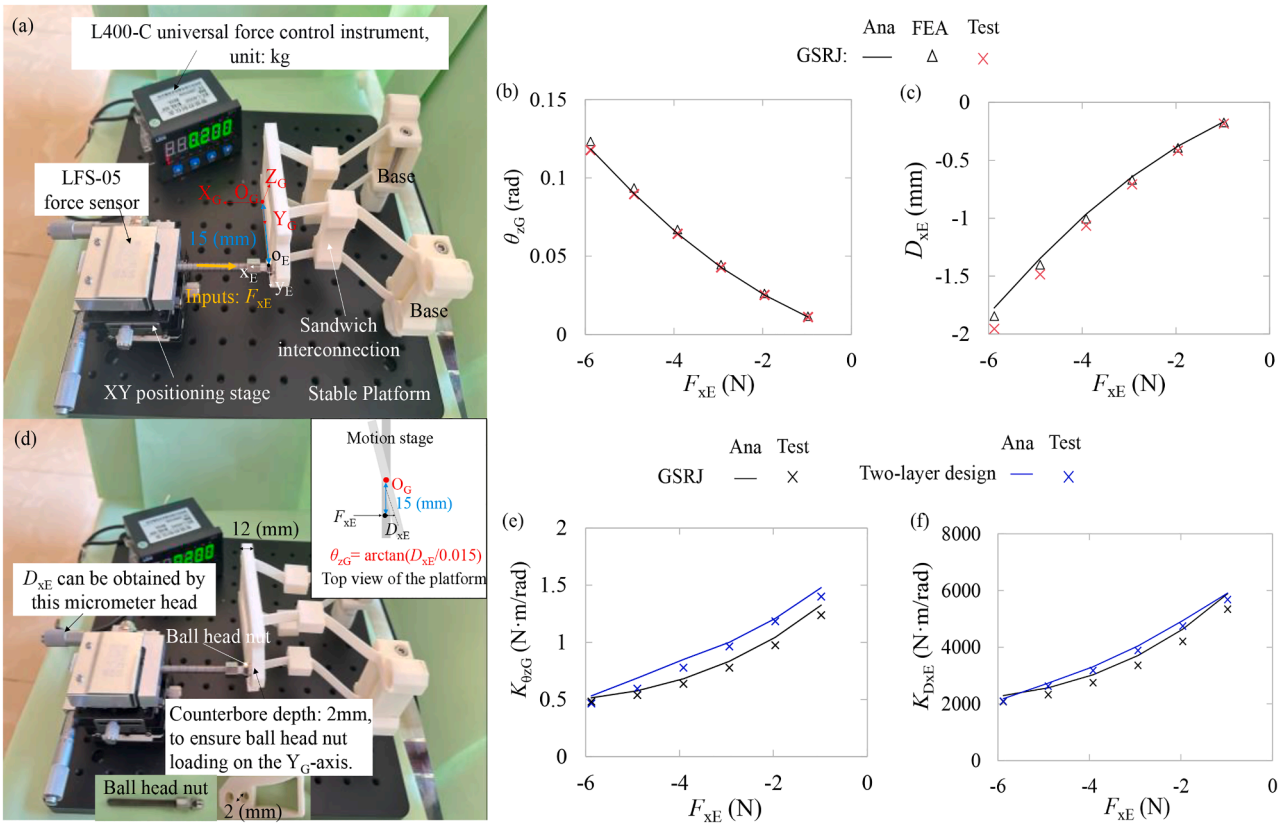


Fig. 14. Experiments on the θ_{zG} and D_{xE} of the two-layer rotational joint and the GSRJ. (a) Test of the GSRJ; (b) Analytical, FEA, and experimental results of θ_{zG} for the GSRJ; (c) Analytical, FEA, and experimental results of D_{xE} for the GSRJ; (d) Test of the two-layer design; (e) Experimental $K_{\theta zG}$ for the GSRJ and two-layer rotational joint; (f) Experimental K_{DxE} for the GSRJ and two-layer rotational joint (K_{DxE} denotes the stiffness calculated by using D_{xE} and F_{xE}).

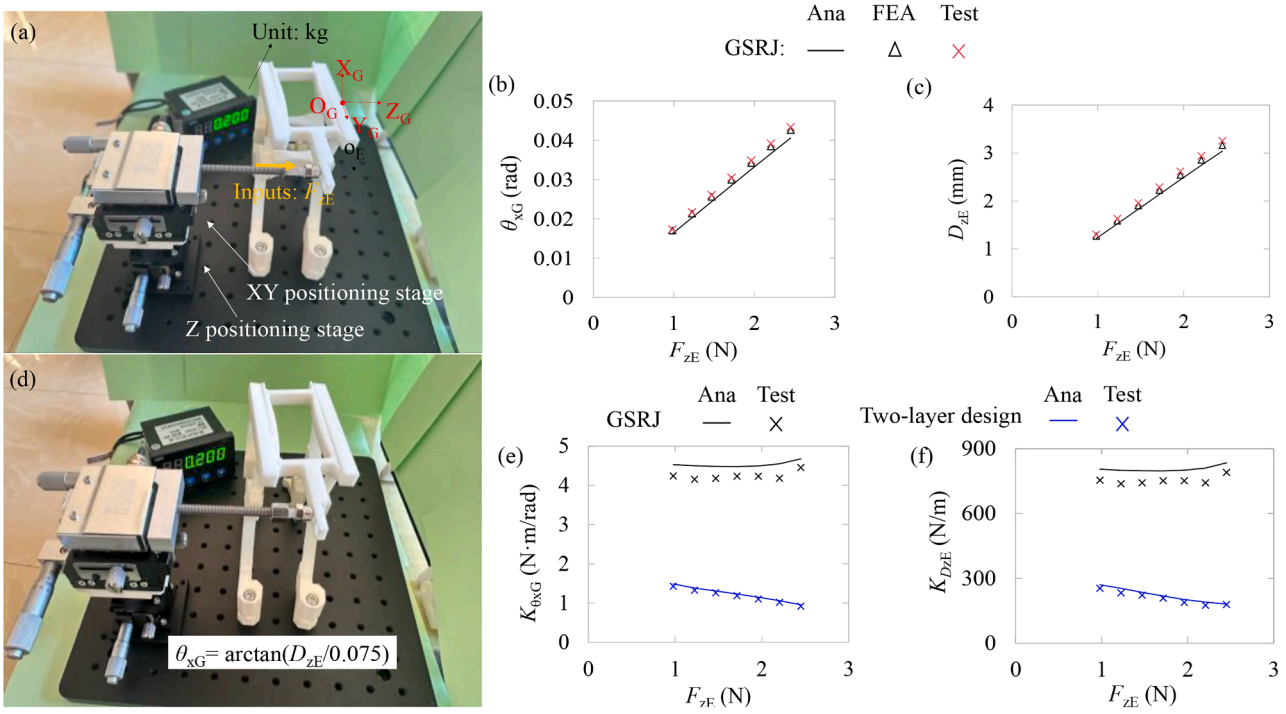


Fig. 15. Experiments on the θ_{xG} and D_{zG} of the two-layer rotational joint and the GSRJ. (a) Test of the GSRJ; (b) Analytical, FEA, and experimental results of θ_{xG} for the GSRJ; (c) Analytical, FEA, and experimental results of D_{zE} for the GSRJ; (d) Test of the two-layer design; (e) Experimental $K_{\theta xG}$ for the GSRJ and the two-layer rotational joint; (f) Experimental K_{DzE} for the GSRJ and two-layer rotational joint (K_{DzE} denotes the stiffness calculated by using D_{zE} and F_{zE}).

$$\begin{bmatrix} \mathbf{f}_G \\ \mathbf{m}_G \end{bmatrix} = \mathbf{D}_{pE}^{T} \begin{bmatrix} \mathbf{f}_E \\ \mathbf{m}_E \end{bmatrix}, \tag{48}$$

where $[\mathbf{f}_E, \mathbf{m}_E]^T$ denotes the loads loading at o_E with respect to o_E-$x_E y_E z_E$; $\mathbf{D}_{pE}$ denotes a 6 × 6 translational matrix, as given by Eq. (49). $\mathbf{D}_{pE}^{T}$ denotes the transpose of $\mathbf{D}_{pE}$.

$$\mathbf{D}_{pE} = \begin{bmatrix} \mathbf{I}_{3\times3} & \begin{bmatrix} 0 & \mathbf{o}_{E_G}(3,1) & -\mathbf{o}_{E_G}(2,1) \\ -\mathbf{o}_{E_G}(3,1) & 0 & \mathbf{o}_{E_G}(1,1) \\ \mathbf{o}_{E_G}(2,1) & -\mathbf{o}_{E_G}(1,1) & 0 \end{bmatrix} \\ \mathbf{0}_{3\times3} & \mathbf{I}_{3\times3} \end{bmatrix}. \tag{49}$$

where $\mathbf{o}_{E_G}$ is the corresponding coordinate with respect to O_G-$X_G Y_G Z_G$.

(1) Input 1: F_{xE} at o_E

In Figs. 14(a) and (d), the aim of this loading condition is to test θ_{zG} and D_{xE}, where θ_{zG} and D_{xE} denote the rotations of the motion stage and the displacements at o_E with respect to O_G-$X_G Y_G Z_G$, respectively. A controlled force (F_{xE}) is applied, ranging from –0.98 N to –5.88 N in increments of –0.98 N (equivalent to –0.1 kg to –0.6 kg in –0.1 kg steps), applied at o_E. $\mathbf{o}_{E_G}$ denotes the coordinates of point o_E with respect to O_G-$X_G Y_G Z_G$ and $\mathbf{o}_{E_G} = [0, 0.015, 0]^T$ (m).

We use f_{xE} to denote the normalized value of F_{xE}, and $[\mathbf{f}_G, \mathbf{m}_G]^T$ can be calculated by substituting f_{xE} into Eq. (48). Then the analytical θ_{zG} can be obtained by substituting $[\mathbf{f}_G, \mathbf{m}_G]^T$ into the analytical model. The experimental θ_{zG} can be calculated as outlined in Fig. 14(d). The analytical D_{xE} is equal to $o_E^*(1,1)$, where $o_E^* = \mathbf{R}_G \cdot \mathbf{o}_{E_G}$. The experimental D_{xE} is measured directly using the XY stage's micrometer. The FEA and experimental results validate the analytical results, as shown in Figs. 14(b) and (c). The maximum error is smaller than 7.5%. The results in Figs. 14(e) and (f) show that the in-plane stiffness of the GSRJ closely matches that of the two-layer rotational joint. This demonstrates that the sandwich interconnection does not enhance the in-plane stiffness. Furthermore, both the rotational stiffness $K_{\theta zG}$ and in-plane stiffness K_{DxE} for the two prototypes exhibit a similar load-dependent nonlinearity, decreasing at comparable rates under an increasing lateral force F_{xE}.

(2) Input 2: F_{zE} at o_E

The aim of this loading condition is to test θ_{xG} and D_{zE} for the GSRJ and the two-layer rotational joint, as shown in Figs. 15(a) and (d). Similar to the case in Input 1, a controlled force (F_{zE}) is applied, ranging from 0.98 N to 2.45 N in increments of 0.98 N (equivalent to 0.1 kg to 0.25 kg in 0.025 kg steps). $\mathbf{o}_{E_G}$ is equal to $[0, 0.075, 0]^T$ (m) in this case. The analytical and experimental θ_{xG} and D_{zE} can be obtained similarly to how we did in Input 1. The FEA and experimental results validate the analytical results, as shown in Figs. 15(b) and (c). In Figs. 15(e) and (f), $K_{\theta xG}$ and K_{dzE} of the GSRJ can be increased by 78% and 81% compared to those of the two-layer rotational joint, respectively. This demonstrates that the sandwich interconnection enhances the out-of-plane stiffness. The out-of-plane stiffness $K_{\theta xG}$ and K_{dzE} of the GSRJ remain nearly constant under increasing axial loading F_{zE}. In contrast, the corresponding stiffness metrics for the two-layer rotational joint exhibit a significant decrease. This result demonstrates how structural configuration critically modulates nonlinear mechanical behavior, with the GSRJ maintaining superior stiffness stability across the loading range compared to its two-layer counterpart.

Measurement errors in the experimental setup primarily originate from four sources: 3D printing fabrication tolerances, assembly inaccuracies, non-ideal contact conditions, and misalignment between the force sensor and the prototype. First, 3D printing fabrication errors such as dimensional deviations and surface roughness are inherent to the 3D printing process, which slightly alter the actual stiffness of the prototype. The dimensions of the prototype's elastic sheets exhibit a small deviation of 0.01 (mm). Assembly errors may arise because the sandwich interconnections and motion stages are bonded to the prototype using super glue. Contact errors occur because the ball-head nut (shown in Fig. 14(d)) experiences frictional or non-ideal point contact with the counterbore. Finally, alignment errors are introduced because the actual loading positions are manually calibrated via the XYZ stages, which may deviate slightly from the positions specified in the analytical model. To minimize the impact of these factors and ensure reliable results, each test was repeated five times under identical conditions, with the load being incrementally and slowly applied during each cycle. The data points presented in Figs. 14 and 15 represent the mean values of these repeated measurements.

The standard deviations of the means, are presented in Fig. 16. Notably, the standard deviation incrementally increases with the applied loads in general, indicating that the accumulation of errors due to misalignment at loading position under large deformations. More importantly, the GSRJ demonstrates significantly higher repeatability and robustness compared to the counterpart two-layer design. The maximum standard deviation for the GSRJ is approximately 0.0356 (mm) and 0.0329 (mm) in X and Z directions, respectively. Conversely, the maximum standard deviation of the two-layer design is roughly twice higher in the X direction (0.0766 mm) and is about six times higher in the Z direction (0.18 mm).

5. Center shift of GSRJ and optimization

The main parasitic motion of the rotational joint is the center shift, which reduces the precision and accuracy of the joint. In this section, the center shift of the GSRJ with respect to O_G-$X_G Y_G Z_G$ is derived and optimized, and the case of the GSRJ (α_1=α_2, α_3=α_4) can be treated as a special example.

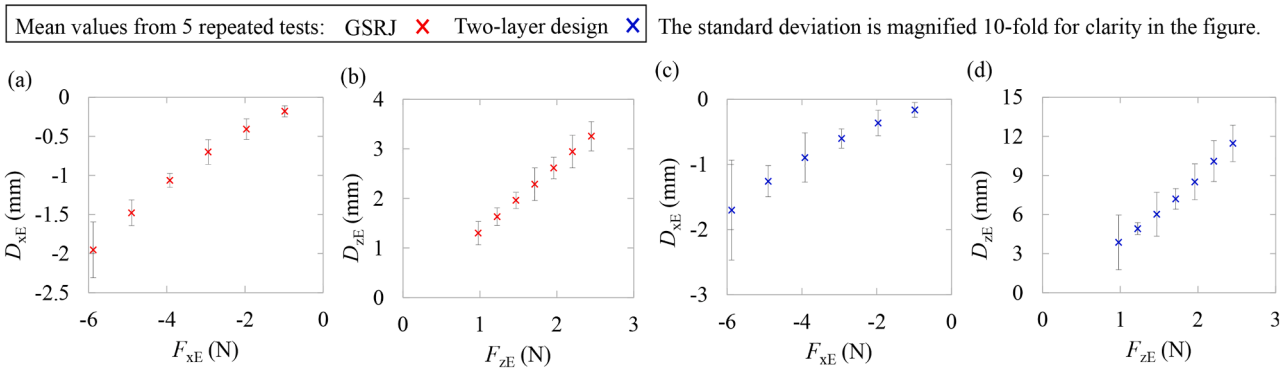


Fig. 16. The standard deviation of the GSRJ and the two-layer design.

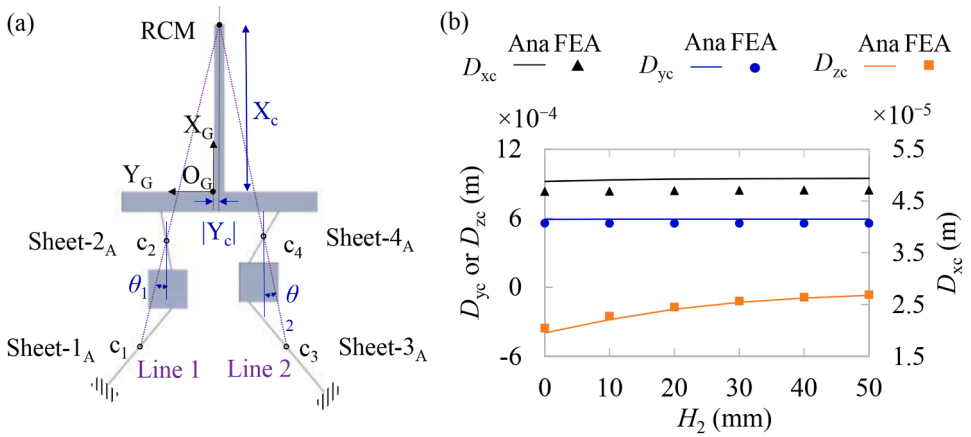


Fig. 17. The spatial center shift of the GSRJ. (a) Method on how to determine the RCM; (b) Analytical and FEA results of the spatial center shift.

5.1. Derivation of the center shift

As illustrated in Fig. 17(a), we use c_j (j = 1, 2, 3 or 4) to denote the sheet center for sheets-j_A, and use $\mathbf{c}_j$ to denote the normalized coordinates. Their equations are given by Eq. (50). Line 1 is formed by points c_1 and c_2, and Line 2 is formed by points c_3 and c_4. RCM of the GSRJ is the projection of the intersection point of Line 1 and Line 2 onto the O_G-X_GY_G plane (This plane is shown in Fig. 2(a)).

$$\mathbf{c}_1 = \begin{bmatrix} -(l_1\cos\alpha_1 + l_2\cos\alpha_2 + t\sin\alpha_1)/2 - h_1 - b_1 - t\sin\alpha_2 \\ b_2 + (l_1\sin\alpha_1)/2 - l_2\sin\alpha_2 \\ 0 \end{bmatrix}, \mathbf{c}_2 = \begin{bmatrix} -h_1 - (l_2\cos\alpha_2 + t\sin\alpha_2)/2 \\ b_2 - (l_2\sin\alpha_2)/2 \\ 0 \end{bmatrix}$$

$$\mathbf{c}_3 = \begin{bmatrix} -(l_3\cos\alpha_3 + t\sin\alpha_3)/2 - l_4\cos\alpha_4 - t\sin\alpha_4 - h_1 - b_3 \\ (-l_3\sin\alpha_3)/2 + l_4\sin\alpha_4 - b_4 \\ 0 \end{bmatrix}, \mathbf{c}_4 = \begin{bmatrix} -(l_4\cos\alpha_4 + t\sin\alpha_4)/2 - h_1 \\ -b_4 + (l_4\sin\alpha_4)/2 \\ 0 \end{bmatrix} \tag{50}$$

The normalized mathematical equations for Line 1 and Line 2 with respect to O_G-$X_GY_GZ_G$ are given by Eqs. (51) and (52), respectively.

$$A_1x_1 + D_1y_1 + W_1 = 0, \tag{51}$$

$$A_2x_2 + D_2y_2 + W_2 = 0, \tag{52}$$

where A_i, D_i, and W_i denote the coefficients of the normalized mathematical equations.

$$A_1 = \mathbf{c}_1(2,1) - \mathbf{c}_2(2,1), D_1 = \mathbf{c}_2(1,1) - \mathbf{c}_1(1,1),$$
$$W_1 = \mathbf{c}_1(1,1)\cdot\mathbf{c}_2(2,1) - \mathbf{c}_2(1,1)\cdot\mathbf{c}_1(2,1)$$

$$A_2 = \mathbf{c}_3(2,1) - \mathbf{c}_4(2,1), D_2 = \mathbf{c}_4(1,1) - \mathbf{c}_3(1,1),$$
$$W_2 = \mathbf{c}_3(1,1)\cdot\mathbf{c}_4(2,1) - \mathbf{c}_4(1,1)\cdot\mathbf{c}_3(2,1)$$

The normalized coordinates of the intersection point (i.e., the rotational center) of the Line 1 and Line 2 with respect to O_G-$X_GY_GZ_G$ are given by Eq. (53),

$$x_c = (D_1W_2 - D_2W_1)/Q,\ y_c = (A_2W_1 - A_2W_2)/Q,\ \text{and}\ z_c = 0, \tag{53}$$

where $[x_c, y_c, z_c]^T$ denotes the normalized coordinates of the rotational center of the GSRJ with respect to O_G-$X_GY_GZ_G$; $Q = A_1D_2 - A_2D_1$; note that if $Q = 0$, the design no longer functions as a rotational joint, and this condition is excluded from further analysis.

As illustrated in Fig. 17(b), the components of the distance between the green point and the black point along the X_G, Y_G, and Z_G axes are defined as the spatial center shift. We use $\mathbf{d}_C = [d_{xc}, d_{yc}, d_{zc}]^T$ to denote the normalized center shift of the GSRJ with respect to O_G-$X_GY_GZ_G$, as given by Eq. (54).

$$\mathbf{d}_C = \mathbf{R}_G \begin{bmatrix} x_c \\ y_c \\ z_c \end{bmatrix} - \begin{bmatrix} x_c \\ y_c \\ z_c \end{bmatrix} + \mathbf{d}_G, \tag{54}$$

where the definition of $\mathbf{d}_G$ is detailed in Eq. (20) and $\mathbf{d}_G$ is given by Eq. (27).

Under the loading condition of Case 1 in Section 4.1, the normalized equations of Line 1 and Line 2 with respect to O_G-$X_GY_GZ_G$ are obtained as Eq. (55). The coordinates of the rotational center with respect to O_G-$X_GY_GZ_G$ are $[X_c, Y_c, Z_c]^T$ = [0.08485, 1.1435 × 10^{-4}, 0]^T (m), where $X_c = x_cL_d$; $Y_c = y_cL_d$; and Z_c=0. Fig. 17(c) compares the analytical and FEA results of the GSRJ center shift, showing an average discrepancy of <6.8%. The results show that the out-of-plane center shift, i.e., d_{zc}, decreases with the increase of H_2. The equations for Line 1 and Line 2 are provided in Eqs. (55) and (56), respectively.

$$\text{Line 1}: \quad 0.01346x_G + 0.0541y_G - 0.0011487 = 0, \tag{55}$$

$$\text{Line 2}: \quad -0.01178x_G + 0.0563y_G + 9.934 \times 10^{-4} = 0. \tag{56}$$

In this paper, the center shift is calculated through the vector difference between the deformed and undeformed spatial coordinates of the designated intersection point (rotational center) under a spatial loading (including translational and rotational loadings). As demonstrated by Verotti et al. [85], the pole of displacement criterion offers a mathematically rigorous and unified interpretation of parasitic motion for planar joints, perfectly accommodating both rotation and translation. In our future work, we plan to derive a spatial pole of displacement criterion (i.e., pure rotational center) utilizing the quaternion method. By mathematically representing spatial motion as a rotation by a specific angle about an arbitrary axis in 3D space, this quaternion-based approach is inherently path-independent. It can provide a stable, singularity-free solution for evaluating spatial center shift,

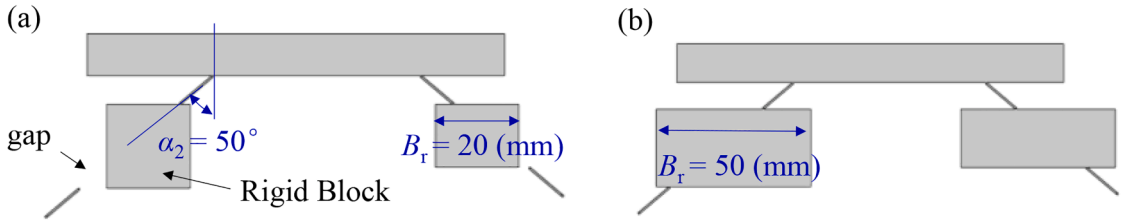


Fig. 18. B_r can be conditionally adjusted since it does not affect the analytical model. (a) The gap occurs when α_i exceeds 30°; (b) The design after revising B_r.

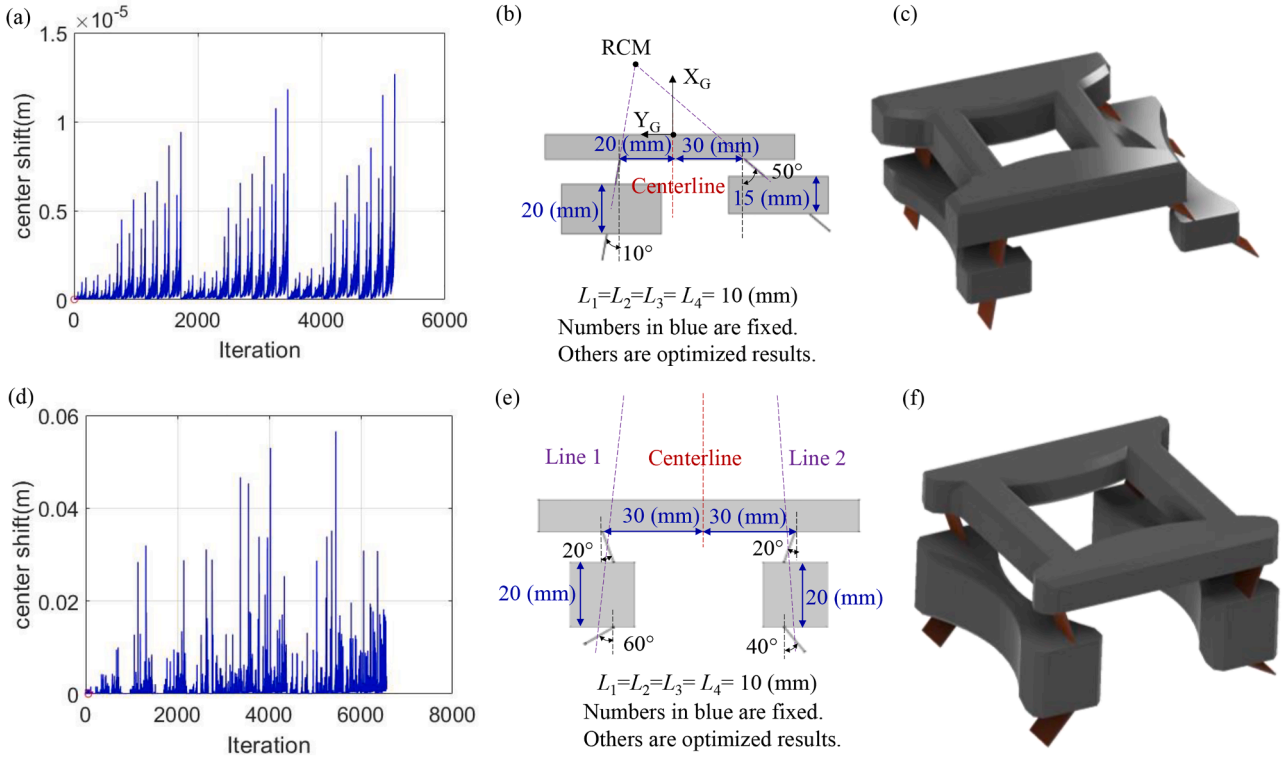


Fig. 19. Optimization of GSRJ. (a) Center shifts of GSRJ ($\alpha_1=\alpha_2$, $\alpha_3=\alpha_4$) at each combination of the geometric parameters; (b) Optimal solution for GSRJ ($\alpha_1=\alpha_2$, $\alpha_3=\alpha_4$), with the blue numbers corresponding to those presented in Table C1 of Appendix C; (c) Weight-reduced design of the GSRJ ($\alpha_1=\alpha_2$, $\alpha_3=\alpha_4$), with the blue numbers corresponding to those presented in Table 1; (d) Center shifts of GSRJ at each combination of the geometric parameters; (e) Optimal solution for GSRJ; (f) Weight-reduced design of the GSRJ.

regardless of how large or extreme the nonlinear bending and twisting deformations of the compliant mechanism may be.

5.2. Optimization of the center shift

In this section, we use the GSRJ and GSRJ ($\alpha_1=\alpha_2$, $\alpha_3=\alpha_4$) as two examples to demonstrate the optimization process. Each case employs a two-stage strategy: first, the analytical model is utilized in MATLAB to optimize the configuration by minimizing the center shift to satisfy design constraints; subsequently, mass topology optimization is performed in Autodesk Inventor to minimize the overall mass while preserving both the aesthetic design and the stiffness of the sandwich interconnections.

The optimization approach is based on a global scan of multiple parameter combinations with objective function minimization. The problem of reducing the center shift is formulated as a multi-variable (L_j and α_j (j = 1, 2, 3 or 4)) and multi-objective optimization problem [86–88], with the objective of minimizing the center shift $\boldsymbol{D}_C$, where $\boldsymbol{D}_C = [D_{xc}, D_{yc}, D_{zc}]^T = \mathbf{d}_C \cdot L_d$. M_x, M_y, and M_z are all constant at 0.01 (N·m) in this part. The optimization process begins with a global grid search using nested loops to iterate through all possible combinations of the geometric parameters (L_j and α_j). This exhaustive approach ensures that the entire predefined design space is explored, thereby guaranteeing the identification of the global optimum rather than a local one.

Starting from the GSRJ configuration with the constraint $\alpha_1=\alpha_2$ and $\alpha_3=\alpha_4$, six geometric parameters are optimized, with the rest kept fixed. Specifically, H_2 is set to 50 (mm), and the other parameters are consistent with those listed in Table C1 of Appendix C. The objective function and constraints are:

Objective function: $D_{C_min} = \text{norm}(\boldsymbol{D}_C)$ or $= (D_{xc}^2 + D_{yc}^2 + D_{zc}^2)^{1/2}$

Constraints: $10 \le L_j \le 50$ (mm) and the step is 20 (mm)

$10° \le \alpha_j \le 80°$ and the step is 10°, j = 1,2,3 or 4

$\alpha_1=\alpha_2$, $\alpha_3=\alpha_4$

$Q \neq 0$, where Q is given by Eq. (53)

In the current implementation, the total number of parameter combinations amounts to $3^4 \times 8^2 = 5184$. After each offset computation, the result is compared with the current minimum offset value. If a smaller value is obtained, both the minimum center shift and the corresponding optimal parameters are updated accordingly. Since the analytical model is independent of the rigid block's length (denoted by B_r, Figs. 18(a) and (b)), this parameter does not affect the optimization results. In this study, B_r is set to 20 (mm); however, when α_i exceeds 30°, a gap appears

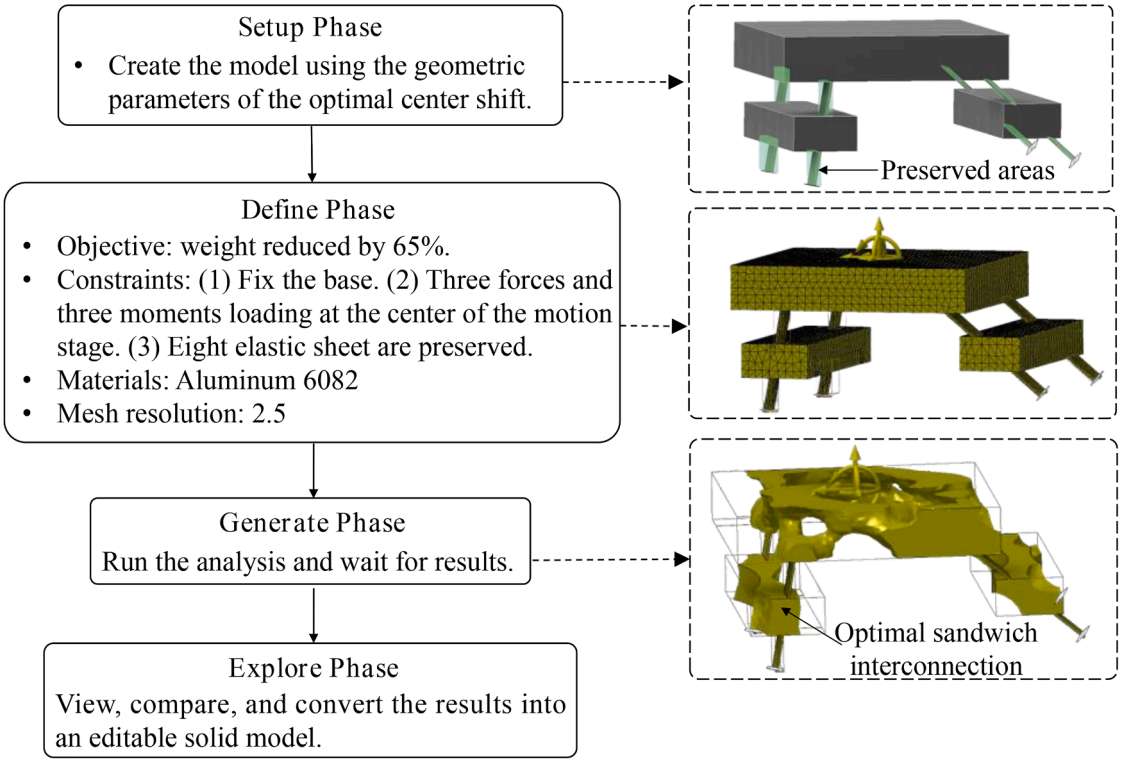


Fig. 20. Flowchart of the mass topology optimization based on Autodesk Inventor software (including objective and constraints).

between the sheets and the rigid block, so B_r can be conditionally adjusted, as shown in Fig. 18(b).

As illustrated in Fig. 19(a), the optimal solution of the GSRJ (α_1=α_2, α_3=α_4) is highlighted on the curves. The optimized design parameters for this GSRJ configuration are as follows: L_1= L_2= L_3= L_4= 10 (mm), α_1=α_2=10°, α_3=α_4=50°, yielding a minimum value of D_{C_min}=1.2685 × 10^{-8}(m). The corresponding optimal configuration is depicted in Fig. 19 (b), where the coordinates of the rotational center relative to the reference frame O_G-$X_GY_GZ_G$ are $[0.02638, 0.01358, 0]^T$ (m), and the center shift is $[5.1449 \times 10^{-6}, -1.0010 \times 10^{-5}, -4.2826 \times 10^{-9}]^T$ (m). The total computing time for this optimization process is 130.93 s. Additionally, a weight-reduced GSRJ (α_1=α_2, α_3=α_4) is designed via topology optimization, as shown in Fig. 19(c). This weight-reduced model is generated using Autodesk Inventor and the detailed generation process is shown in Fig. 20.

In the case of the GSRJ, eight geometric parameters are optimized with the remaining parameters held constant. Specifically, H_2 is set to 50 (mm), and the other parameters are consistent with those listed in Table 1. The objective function and constraints are:

Objective function: D_{C_min}= norm ($\boldsymbol{D}_C$)

Constraints: $10 \leq L_j \leq 50$ (mm) and the step is 20 (mm)

$20° \leq \alpha_j \leq 60°$ and the step is 20°, (j = 1, 2, 3 or 4)

$Q \neq 0$, $D_1 \neq 0$, $D_2 \neq 0$, where D_1 and D_2 are in Eqs. (51) and (52), respectively. If $Q = 0$, Line 1 and Line 2 (see Fig. 17(a)) do not intersect; if D_1 or D_2 =0, Line 1 or Line 2 is parallel to the Y_G-axis.

In the current implementation, the total number of parameter combinations amounts to $3^4 \times 3^4 = 6561$. As illustrated in Fig. 19(d), the optimal solution is highlighted on the curves to facilitate result verification. The optimized design parameters for the GSRJ are as follows: L_1= L_2= L_3= L_4= 10 (mm), α_1= 60°, α_2 = 20°, α_3= 40°, α_4 = 20°, yielding a minimum value of D_{C_min}=1.20386 × 10^{-5} (m). The corresponding optimal configuration of the GSRJ is depicted in Fig. 19(e), with the coordinates of the rotational center relative to the reference frame O_G-$X_GY_GZ_G$ being $[0.3687, -0.008247, 0]^T$ (m), and the center shift being $[-2.3122 \times 10^{-7}, -2.6518 \times 10^{-6}, -6.6667 \times 10^{-7}]^T$ (m). The total computing time for this optimization process is 80.82 s, and the weight-reduced design for the optimal solution is shown in Fig. 19 (f).

From the optimal results in both cases, we can observe that all sheet lengths have been selected to be 10 (mm), which may suggest that a shorter sheet length corresponds to a smaller center shift. The optimal center shift in GSRJ (α_1=α_2, α_3=α_4) is on the order of 10^{-8}(m). This minimal deviation makes it an ideal choice for precision engineering applications. Conversely, the optimal center shift in GSRJ is on the order of 10^{-5}(m), which is relatively larger and is highly suitable for applications such as assistive hinges for knee rehabilitation, where the increased center shift can help compensate for the misalignment between the artificial hinge and the human knee joint.

Additional constraints can also be imposed based on practical engineering requirements to obtain the desired design, such as limiting the rotational center position within a prescribed range and restricting the maximum allowable deformation. The angle step can be reduced to 10 degrees or less to increase solution resolution, though this refinement will proportionally extend the total calculation time.

6. Conclusions

A novel generalized compliant joint utilizing eight elastic sheets has been developed and spatially analyzed. This design facilitates the creation of multiple joint types and is specifically engineered to achieve the RCM. Sandwich interconnection is implemented to enhance the out-of-plane stiffness of the generalized joint [81,82]. A nonlinear spatial analytical model for the generalized sandwich design is developed using the Beam Constraint Model and Free-Body Diagram methods. This analytical model offers a significant advantage in capturing the nonlinear characteristics of the stiffness. Its accuracy is validated by nonlinear FEA, with a maximum error below 7% and a minimum error under 1%. Building on the advantages of the analytical model, the out-of-plane stiffness between a generalized sandwich design and its counterparts is studied. This analysis first confirms a well-established principle: the sandwich interconnection effectively enhances out-of-plane stiffness, a conclusion consistent with most prior studies

[81,82]. The replication of this effect further validates the predictive accuracy of our proposed model. Notably, a critical divergence from existing research is identified: while prior work asserts that the sandwich design results in a smaller stiffness change than the single-layer counterpart, this study demonstrates that this conclusion is only valid for symmetric PFM and cannot be extended to the generalized sandwich design. Instead, the stiffness change is shown to be highly dependent on the structural configuration of elastic sheets. Furthermore, parametric studies have been performed by varying key geometric parameters (i.e., sheet length and tilt angle) to investigate their effects on the stiffness ratios between asymmetric and symmetric generalized sandwich designs. The results reveal that the three out-of-plane stiffness ratios exhibit distinct sensitivities to geometric parameters. The variation trends and optimal parameters are summarized in the main text. Prototypes of the generalized sandwich design and the two-layer rotational joint have been fabricated for their in-plane and out-of-plane stiffness. Experimental results confirm the accuracy of both the proposed analytical model and the nonlinear FEA.

Finally, a generalized method has been introduced to calculate the center shift in rotational joints composed of elastic sheets or rods. Using this method, optimizations have been performed to reduce the center shift in generalized sandwich rotational joints within given ranges of geometric parameters. Furthermore, a generalized topology optimization framework is proposed and successfully applied to achieve weight reduction in the sandwich interconnection. It should be noted that while the generalized sandwich design has improved the bearing stiffness without affecting the primary motion stiffness, it does introduce several potential problems. These include the increased footprint in the out-of-plane direction, the manufacturing difficulty, and the overall weight. Therefore, in practical applications, careful tradeoffs must be considered between the enhancement of stiffness and these inherent constraints.

Overall, the proposed generalized sandwich design expands the design envelope of compliant joints and is particularly beneficial for nano-positioning systems and micro-electro-mechanical systems, where positioning precision is critical. Stiffness ratios can be directionally adjusted by leveraging our findings on asymmetric features. Additionally, the generalized equations for the center shift for the compliant rotational joint provide a foundation for selecting geometric parameters through objective function optimization under practical engineering constraints.

CRediT authorship contribution statement

Shiyao Li: Writing – review & editing, Writing – original draft, Validation, Funding acquisition, Data curation. **Jiaxiang Zhu:** Resources. **Guangbo Hao:** Supervision, Project administration, Methodology, Formal analysis, Conceptualization.

Declaration of competing interest

The authors declare that they have no known competing financial interests or personal relationships that could have appeared to influence the work reported in this paper.

Acknowledgement

This research was supported by project of Liaoning Provincial Education Department, China (Nos. 20240213 and 20240153; Funder ID: 10.13039/501100013099); supported by the fundamental research funds for the universities of LiaoNing province (LJ212510143018 and LJ212510143040);

Appendix A. The maximum deformation of the asymmetric GSRJ and GSTJ

We select AL 6082 alloy (EU standard), and its yield strength is 276 (MPa). The geometric parameters of the GSRJ, GSRJ (α_1=α_2, α_3=α_4), and GSTJ are shown in Tables 1, C1, and C2, and their maximum deformations are shown below.

In Figs. A1(a) and (b), the primary rotation is 0.11 (rad) about the Z-axis, when M_z=0.9 (N·m). The maximum primary rotation of the GSRJ about the Z-axis is 0.03 (rad), limited by the yield strength under the specific sheet arrangement, as shown in Fig. A1(c).

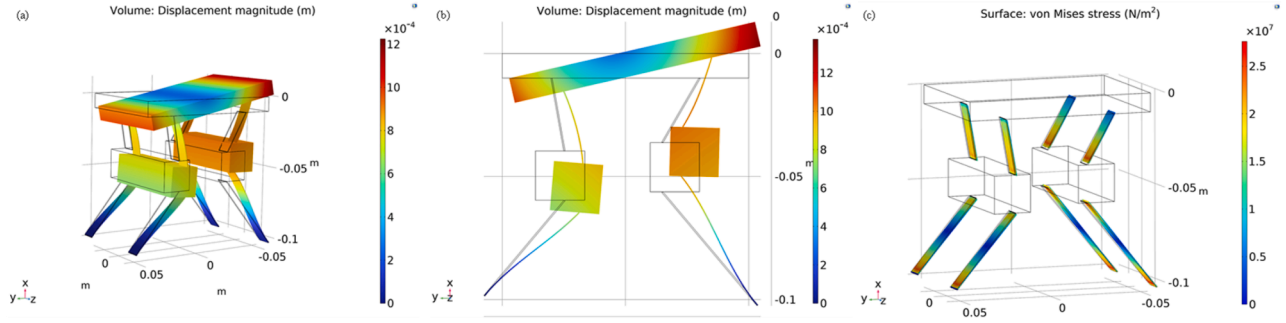


Fig. A1. The maximum deformation analysis of the GSRJ. (a) Spatial display of the GSRJ; (b) Displacement magnitude; (c) Von Mises stress. The scale factor of the deformation in the FEA for displaying deformation is set to 10 in this figure.

The maximum primary rotation of the GSRJ (α_1=α_2, α_3=α_4) is shown in Fig. A2, limited by the yield strength under the 20 (mm) short sheet of the model, as shown in Fig. A2(c).

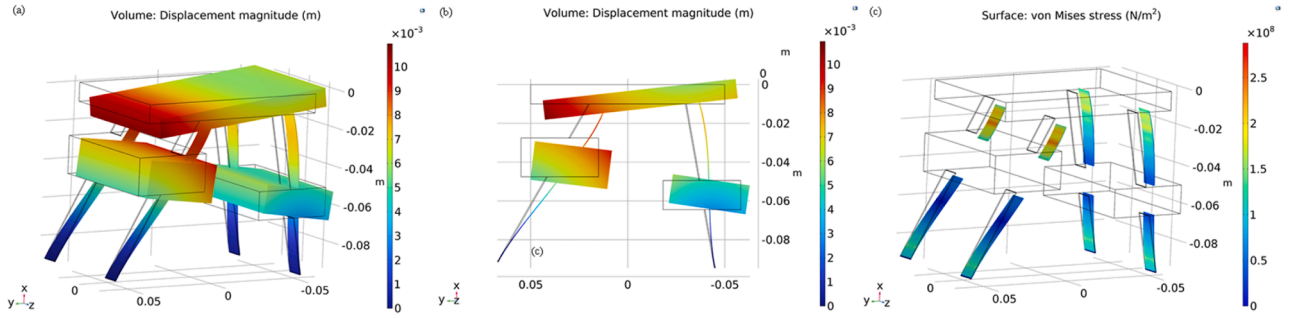


Fig. A2. The maximum deformation analysis of the GSRJ (α_1=α_2, α_3=α_4). (a) Spatial display of the GSRJ (α_1=α_2, α_3=α_4); (b) Displacement magnitude; (c) Von Mises stress. The scale factor of the deformation in the FEA for displaying deformation is set to 1 in this figure.

The maximum primary translation of the GSTJ along the Y-axis is 1.8 (mm), as shown in Fig. A3.

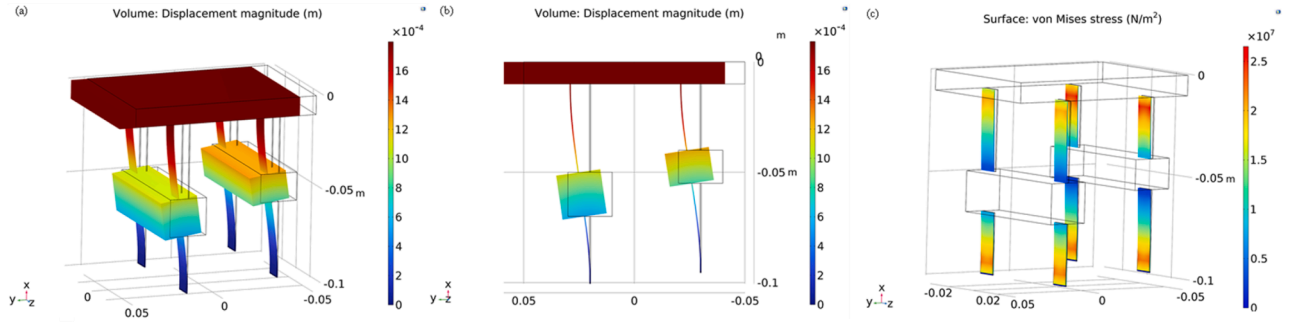


Fig. A3. The maximum deformation analysis of the GSTJ. (a) Spatial displacement magnitude; (b) Plane displacement magnitude; (c) Von Mises stress. The scale factor of the deformation in the FEA for displaying deformation is set to 5 in this figure.

Appendix B. The nonlinear spatial analytical model of the two-layer rotational joint

The two-layer rotational joint consists of four parameterized lumped-compliance sheets arranged in parallel. The compatibility conditions and loading conditions are derived as follows.

Step 1: GSLS model

This model is presented in Section 2.

Step 2: Compatibility conditions of the two-layer rotational joint in a deformed condition.

The compatibility conditions of the two-layer rotational joint can be derived similarly according to the Step 2 in Section 3. We take the compatibility condition between $\mathbf{R}_G$, $\mathbf{R}_{1A}$, and $\mathbf{R}_{1\&2A}$ as an example, where $\mathbf{R}_{1\&2A}$ denotes the rotational matrix with respect to o_{1A}-$x_{1A}y_{1A}z_{1A}$.

The rotational compatibility condition of the two-layer is given by Eqs. (B.1) and (B.2).

$$\mathbf{R}_G = \mathbf{R}_{z(\beta_1)}{}^{-1}\mathbf{R}_{1A}\mathbf{R}_{z(\beta_2)}\mathbf{R}_{2A}\mathbf{R}_{z(\beta_2)}{}^{-1}\mathbf{R}_{z(\beta_1)}, \tag{B.1}$$

$$\mathbf{R}_G = \mathbf{R}_{z(\beta_3)}{}^{-1}\mathbf{R}_{3A}\mathbf{R}_{z(\beta_4)}\mathbf{R}_{4A}\mathbf{R}_{z(\beta_4)}{}^{-1}\mathbf{R}_{z(\beta_3)}, \tag{B.2}$$

where, $\mathbf{R}_{jA}$ are the rotational matrix of sheet-j_A with respect to O_{jA}-$X_{jA}Y_{jA}Z_{jA}$.; j = 1,2,3 or 4; others are same as those of Eq. (17).

The normalized displacements with respect to o_{2A}-$x_{2A}y_{2A}z_{2A}$ and O_G-$X_GY_GZ_G$ can be expressed by those with respect to o_{1A}-$x_{1A}y_{1A}z_{1A}$, as shown in Eqs. (B.3) and (B.4), respectively.

$$\mathbf{d}_{1A} = \mathbf{R}_{1A}\mathbf{R}_{z(\beta_2)}\mathbf{d}_{2A}, \tag{B.3}$$

$$\mathbf{d}_{1A} = \mathbf{R}_{z(\beta_1)}\mathbf{d}_G, \tag{B.4}$$

where, $\mathbf{d}_{1A}$ and $\mathbf{d}_{2A}$ denote the normalized displacements with respect to o_{1A}-$x_{1A}y_{1A}z_{1A}$ and o_{2A}-$x_{2A}y_{2A}z_{2A}$, respectively.

$\mathbf{R}_{1\&2A}$ can be derived as Eq. (B.5). The relationship between $\mathbf{R}_G$ and $\mathbf{R}_{1\&2A}$ can be given by Eq. (B.6). Substituting Eq. (B.5) into Eq. (B.6), the rotational compatibility condition between $\mathbf{R}_G$, $\mathbf{R}_{1A}$, and $\mathbf{R}_{1\&2A}$ can be obtained.

$$\mathbf{R}_{1\&2A} = \mathbf{R}_{1A}\mathbf{R}_{z(\beta_2)}\mathbf{R}_{2A}\mathbf{R}^{-1}_{z(\beta_2)}, \tag{B.5}$$

$$\mathbf{R}_G = \mathbf{R}_{z(\beta_1)}\mathbf{R}_{1\&2A}\mathbf{R}^{-1}_{z(\beta_1)}. \tag{B.6}$$

We use $\mathbf{R}_{1\&2B}$, $\mathbf{R}_{3\&4A}$ and $\mathbf{R}_{3\&4B}$ denote the rotational matrices with respect to o_{1B}-$x_{1B}y_{1B}z_{1B}$, o_{3A}-$x_{3A}y_{3A}z_{3A}$, and o_{3A}-$x_{3B}y_{3B}z_{3B}$, respectively. The rotational compatibility condition between $\mathbf{R}_G$ and $\mathbf{R}_{3\&4A}$ (or $\mathbf{R}_{1\&2B}$, or $\mathbf{R}_{3\&4B}$) can be obtained similarly.

Step 3: Load-equilibrium condition of the two-layer rotational joint in a deformed condition

The load-equilibrium condition is given by Eqs. (B.7) to (B.11).

$$\begin{bmatrix}\mathbf{f}_G\\ \mathbf{m}_G\end{bmatrix} = \mathbf{D}^T_{p2A}\mathbf{R}^{-1}_{Rz(\beta_1)}\mathbf{R}_{R1A}\mathbf{R}_{Rz(\beta_2)}\begin{bmatrix}\mathbf{f}_{2A}\\ \mathbf{m}_{2A}\end{bmatrix} + \mathbf{D}^T_{p4A}\mathbf{R}^{-1}_{Rz(\beta_3)}\mathbf{R}_{R3A}\mathbf{R}_{Rz(\beta_4)}\begin{bmatrix}\mathbf{f}_{4A}\\ \mathbf{m}_{4A}\end{bmatrix} + \mathbf{D}^T_{p2B}\mathbf{R}^{-1}_{Rz(\beta_1)}\mathbf{R}_{R1B}\mathbf{R}_{Rz(\beta_2)}\begin{bmatrix}\mathbf{f}_{2B}\\ \mathbf{m}_{2B}\end{bmatrix} + \mathbf{D}^T_{p4A}\mathbf{R}^{-1}_{Rz(\beta_3)}\mathbf{R}_{R3A}\mathbf{R}_{Rz(\beta_4)}\begin{bmatrix}\mathbf{f}_{4B}\\ \mathbf{m}_{4B}\end{bmatrix}, \tag{B.7}$$

$$\begin{bmatrix}\mathbf{f}_{1A}\\ \mathbf{m}_{1A}\end{bmatrix} = \mathbf{D}^T_{p2Amo1A}\mathbf{R}_{R1A}\mathbf{R}_{Rz(\beta_2)}\begin{bmatrix}\mathbf{f}_{2A}\\ \mathbf{m}_{2A}\end{bmatrix}, \tag{B.8}$$

$$\begin{bmatrix}\mathbf{f}_{1B}\\ \mathbf{m}_{1B}\end{bmatrix} = \mathbf{D}^T_{p2Bmo1B}\mathbf{R}_{R1B}\mathbf{R}_{Rz(\beta_2)}\begin{bmatrix}\mathbf{f}_{2B}\\ \mathbf{m}_{2B}\end{bmatrix}, \tag{B.9}$$

$$\begin{bmatrix}\mathbf{f}_{3A}\\ \mathbf{m}_{3A}\end{bmatrix} = \mathbf{D}^T_{p4Amo3A}\mathbf{R}_{R3A}\mathbf{R}_{Rz(\beta_4)}\begin{bmatrix}\mathbf{f}_{4A}\\ \mathbf{m}_{4A}\end{bmatrix}, \tag{B.10}$$

$$\begin{bmatrix}\mathbf{f}_{3B}\\ \mathbf{m}_{3B}\end{bmatrix} = \mathbf{D}^T_{p4Bmo3B}\mathbf{R}_{R3B}\mathbf{R}_{Rz(\beta_4)}\begin{bmatrix}\mathbf{f}_{4B}\\ \mathbf{m}_{4B}\end{bmatrix}, \tag{B.11}$$

where, we use $\mathbf{f}_{jA}$ and $\mathbf{m}_{jA}$ to denote the loads with respect to o_{jA}-$x_{jA}y_{jA}z_{jA}$, and use $\mathbf{f}_{jB}$ and $\mathbf{m}_{jB}$ to denote the loads with respect to o_{jB}-$x_{jB}y_{jB}z_{jB}$.

$\mathbf{D}_{p2A}$, $\mathbf{D}_{p4A}$, $\mathbf{D}_{p2Amo1A}$, and $\mathbf{D}_{p4Amo3A}$ are 6×6 translational matrices, which can be derived in a similar manner according to Eqs. (36) through (39). These translational matrices are derived using the corresponding coordinates after deformation. To obtain these matrices for the two-layer rotational joint, the Z-axis coordinate in the original corresponding coordinate should be updated from 0 to $h_2/2$.

$\mathbf{D}_{p2B}$, $\mathbf{D}_{p4B}$, $\mathbf{D}_{p2Bmo1B}$, and $\mathbf{D}_{p4Bmo3B}$ are 6×6 translational matrices, which can be derived in a similar manner according to Eqs. (36) through (39). These translational matrices are derived using the corresponding coordinates after deformation. To obtain these matrices for the two-layer rotational joint, the Z-axis coordinate in the original corresponding coordinate should be updated from 0 to $-h_2/2$.

Appendix C. Stiffness analysis for two special designs of the GSRJ

The two specific configurations studied in this appendix are derived from the GSRJ, as introduced in Section 3. They are the GSRJ (α_1=α_2, α_3=α_4) and GSTJ (α_1=α_2=α_3=α_4=0). The analytical models for the two designs can be directly obtained by substituting the corresponding geometric parameters into the GSRJ model.

C1: Analytical model verification of the two special designs

(1) Case 1: Analytical model verification of GSRJ (α_1=α_2, α_3=α_4)

The geometric parameters of the GSRJ (α_1=α_2, α_3=α_4) are shown in Table C1, and its FEA model is shown in Fig. C1(c). When M_{xG}=M_{yG}=M_{zG}=0.1 (N·m), and the thickness of the sandwich interconnection ranges from 0 to 50 (mm) with a step of 10 (mm), the analytical and FEA results of the motion stage are shown in Fig. C1. The average errors between the FEA and analytical results are all smaller than 5.8%, confirming the accuracy of the proposed analytical model. The results indicate that the out-of-plane displacement and rotations, D_{zG}, θ_{xG}, and θ_{yG}, decrease significantly with increasing thickness of the sandwich interconnection. In-plane displacements and rotation, D_{xG}, D_{yG}, and θ_{zG}, remain unchanged, indicating that the sandwich interconnection does not affect the in-plane stiffness.

Table C1
Geometric parameters of the asymmetric GSRJ (α_1=α_2). (Length unit: mm).

	Parameters	Values		Parameters	Values
T	Sheet thickness	0.5	B_1, B_3	Height of the rigid block	B_1= 20, B_3= 15
L_j	Sheet length for sheet-j_A and sheet-j_B	L_1= 50, L_2= 20, L_3= 30, L_4= 40,	B_2, B_4	Horizontal distance between o_2 and O_G, o_4 and O_G.	B_2= 20, B_4= 30
U	Sheet width	10	H_1	Height of the motion stage	10
α_j	Tilt angle for sheet-j_A and sheet-j_B	α_1= 30°, α_2= 30° α_3= 10°, α_4= 10°	H_2	Thickness of the sandwich interconnection (or space)	0 to 50 with a step of 10

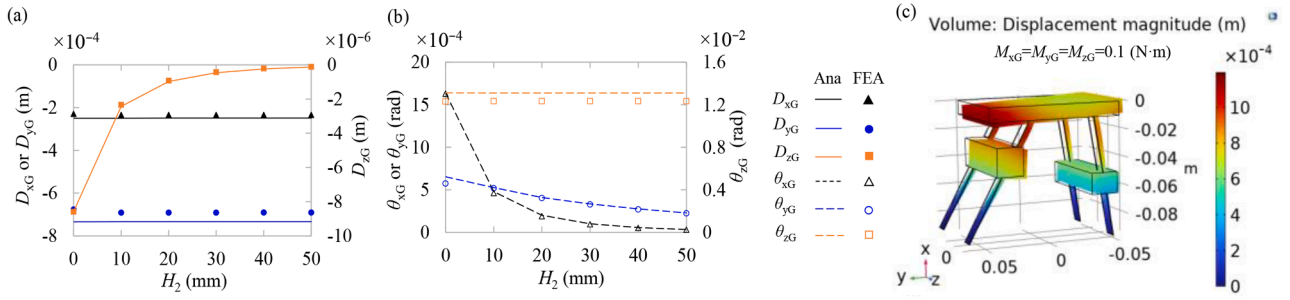


Fig. C1. The analytical and FEA results of the GSRJ ($\alpha_1=\alpha_2$, $\alpha_3=\alpha_4$) versus increasing thickness of the sandwich interconnection. (a) Displacements; (b) Rotations; (c) FEA simulation for H_2 =50 (mm).

(2) Case 2: Analytical model verification of GSTJ

The symmetric sandwich translational joint was comprehensively studied in [81]. In this section, we focus on studying the asymmetric GSTJ, and its geometric parameters are shown in Table C2.

Table C2
Geometric parameters of the asymmetric GSTJ. (Length unit: mm).

	Parameters	Values		Parameters	Values
T	Sheet thickness	0.5	B_1, B_3	Height of the rigid block	B_1= 20, B_3= 15
L_j	Sheet length for sheet-j_A and sheet-j_B	L_1= 30, L_2= 40, L_3= 40, L_4= 30,	B_2, B_4	Horizontal distance between o_2 and O_G, o_4 and O_G.	B_2= 20, B_4= 30
U	Sheet width	10	H_1	Height of the motion stage	10
α_j	Tilt angle for sheet-j_A and sheet-j_B (i = 1,2,3 or 4)	α_i= 0°	H_2	Thickness of the sandwich interconnection (or space)	0 to 50 with a step of 10

When F_{xG}= F_{zG}=0.5 (N), F_{yG}= 1(N), and the thickness of the sandwich interconnection ranges from 0 to 50 (mm) with a step of 10 (mm), the analytical and FEA results of the motion stage are shown in Fig. C2. The average errors between the FEA and analytical results are all smaller than 4%. The results indicate that out-of-plane rotations θ_{xG} and θ_{yG} decrease significantly with increasing thickness of the sandwich interconnection. The out-of-plane displacement D_{zG} is too small and shows a minimal variation. In-plane displacements and rotation D_{xG}, D_{yG} and θ_{zG} remain unchanged, indicating that the sandwich interconnection does not affect the in-plane stiffness.

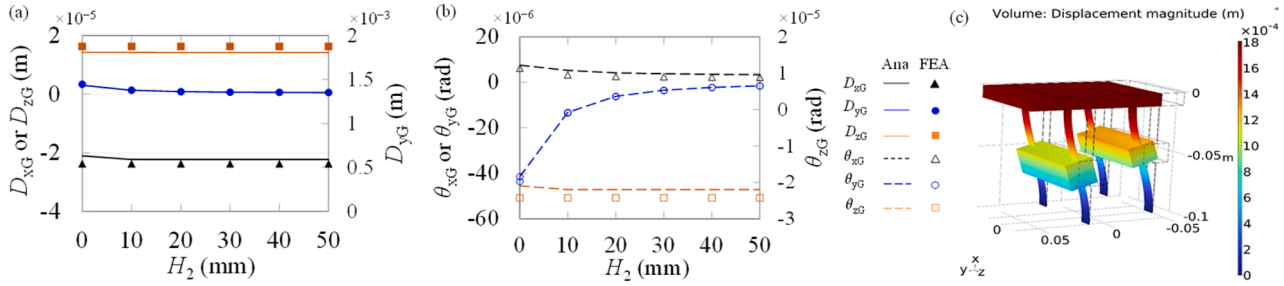


Fig. C2. The analytical and FEA results of the GSTJ versus increasing thickness of the sandwich interconnection H_2. (a) Analytical and FEA displacements; (b) Analytical and FEA rotations; (c) FEA simulation for H_2 =50 (mm).

C2: Stiffness analysis for the GSRJ ($\alpha_1=\alpha_2$, $\alpha_3=\alpha_4$) and comparisons with counterpart designs

(1) Case 1: Stiffness comparison among the GSRJ, two-layer joint, and single-layer rotational joint under an identical out-of-plane footprint

The primary motion (rotational) stiffness of the GSRJ and the two-layer rotational joint, denoted as $K_{\theta zG}$, is calculated by applying pure moment M_{zG} (specifically, 0.1 N·m and 0.12 N·m) to the motion stage. The corresponding results are presented in Fig. C3(a). $K_{\theta zG}$ of both designs remains constant with increasing thickness of the sandwich interconnection. In other words, the sandwich interconnection or sandwich space does not affect the rotational stiffness. Then, with M_{zG} held constant at 0.2 (N·m) to preload the joint, the out-of-plane stiffness $K_{\theta xG}$ is determined by applying a moment M_{xG} of 0.01 (N·m) and 0.012 (N·m), while out-of-plane stiffness $K_{\theta yG}$ is determined by applying a moment M_{yG} of the same magnitudes; out-of-plane stiffness K_{dzG} is calculated by applying a force F_{zG} of 0.01 (N) and 0.012 (N). Both $K_{\theta xG}$ and K_{dzG} of the GSRJ in Fig. C3(b) and (d) increase significantly with increasing sandwich thickness compared with those of the two-layer rotational joint, while $K_{\theta yG}$ shows a gradual increase in Fig. C3 (c). When H_2 = 50 (mm), $K_{\theta xG}$, $K_{\theta yG}$ and K_{dzG} increase by 82%, 39%, and 361%, respectively.

$K_{\theta zG}$ of both joints remains constant, but the out-of-plane stiffness of the GSRJ is significantly improved than that of the two-layer rotational joint.

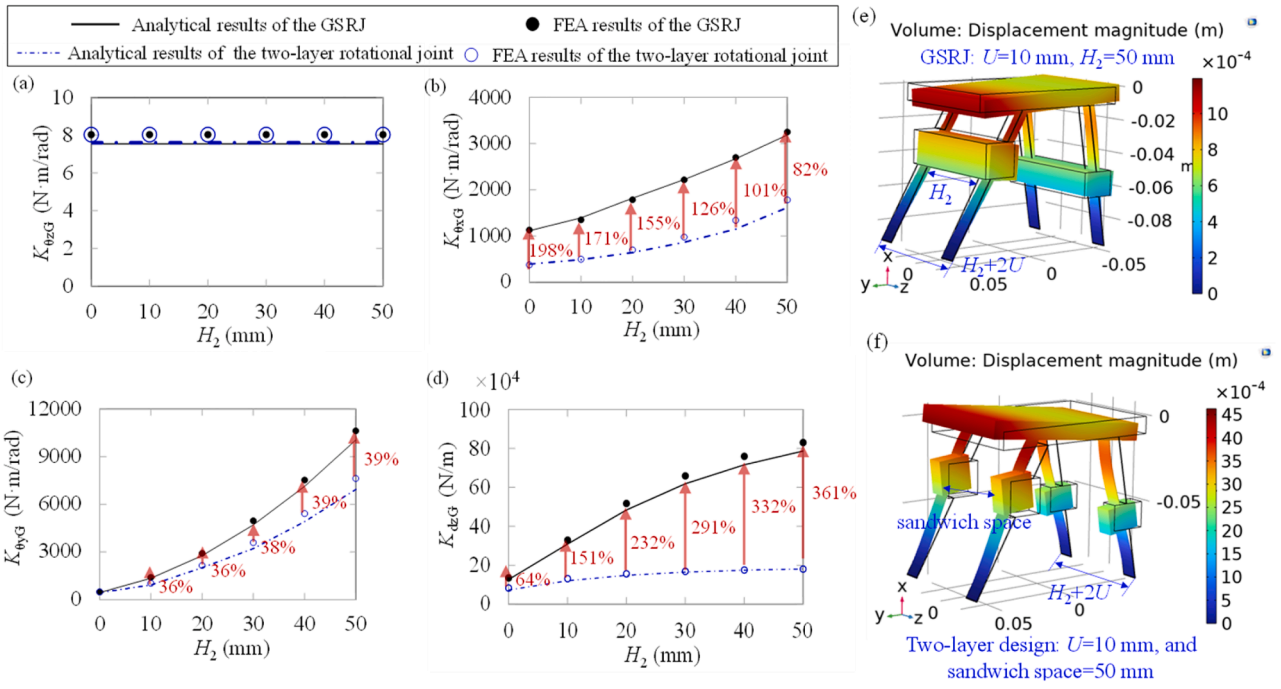


Fig. C3. The stiffness comparison between the GSRJ (α_1=α_2, α_3=α_4) and the two-layer rotational joint versus increasing thickness of the sandwich interconnection H_2. (a) Rotational stiffness $K_{\theta zG}$; (b) Out-of-plane stiffness $K_{\theta xG}$; (c) Out-of-plane stiffness $K_{\theta yG}$; (d) Out-of-plane stiffness K_{dzG}; (e) The GSRJ; (f) The counterpart model: a two-layer rotational joint.

To compare their stiffness under the same *FT*, the geometric parameters of the GSRJ and the single-layer rotational joint are slightly different, as provided in Table 1 of Section 4.1. All other parameters are identical to those listed in Table C1.

M_{zG} is held constant at 0.1 (N·m), and the primary motion (rotational) stiffness and out-of-plane stiffness of the two designs are calculated using the same approach described earlier. These results indicate that both the rotational stiffness and out-of-plane stiffness of the single-layer rotational joint increase significantly with increasing *FT*. As demonstrated in Fig. C4(a), the GSRJ maintains a stable rotational stiffness, while the single-layer rotational joint shows a progressive increase in both rotational stiffness and out-of-plane stiffness. In Figs. C4(b) to (d), the out-of-plane stiffness of the GSRJ does not increase as much as that of the single-layer rotational joint under this geometric condition, which means the sheet width has a significantly greater influence on the stiffness than the thickness of the sandwich interconnection.

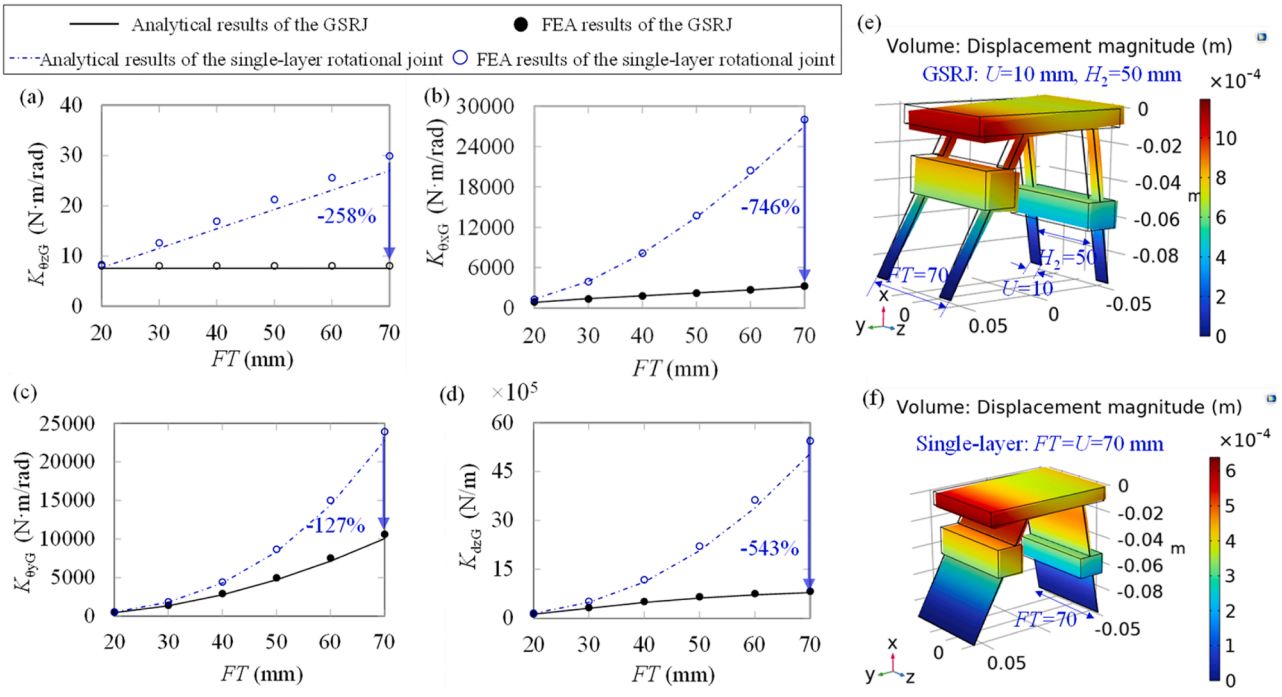


Fig. C4. The stiffness comparison between the GSRJ (α_1=α_2, α_3=α_4) and the single-layer rotational joint versus increasing *FT*. (a) Primary motion (rotational) stiffness $K_{\theta zG}$; (b) Out-of-plane stiffness $K_{\theta xG}$; (c) Out-of-plane stiffness $K_{\theta yG}$; (d) Out-of-plane stiffness K_{dzG}; (e) The GSRJ; (f) The counterpart model: single-layer rotational joint.

Then we study the stiffness changes of the GSRJ, a single-layer rotational joint, and a two-layer rotational joint under increasing primary rotations (θ_{ZG}). As shown in Figs. C5, all three designs exhibit similar stiffness trends, albeit with different magnitudes. However, the GSRJ consistently demonstrates the highest out-of-plane stiffness. The single-layer rotational joint exhibits the smallest stiffness changes in $K_{\theta xG}$ and $K_{\theta yG}$, followed by GSRJ. Stiffness change in $K_{\theta yG}$ of the GSRJ is the smallest.

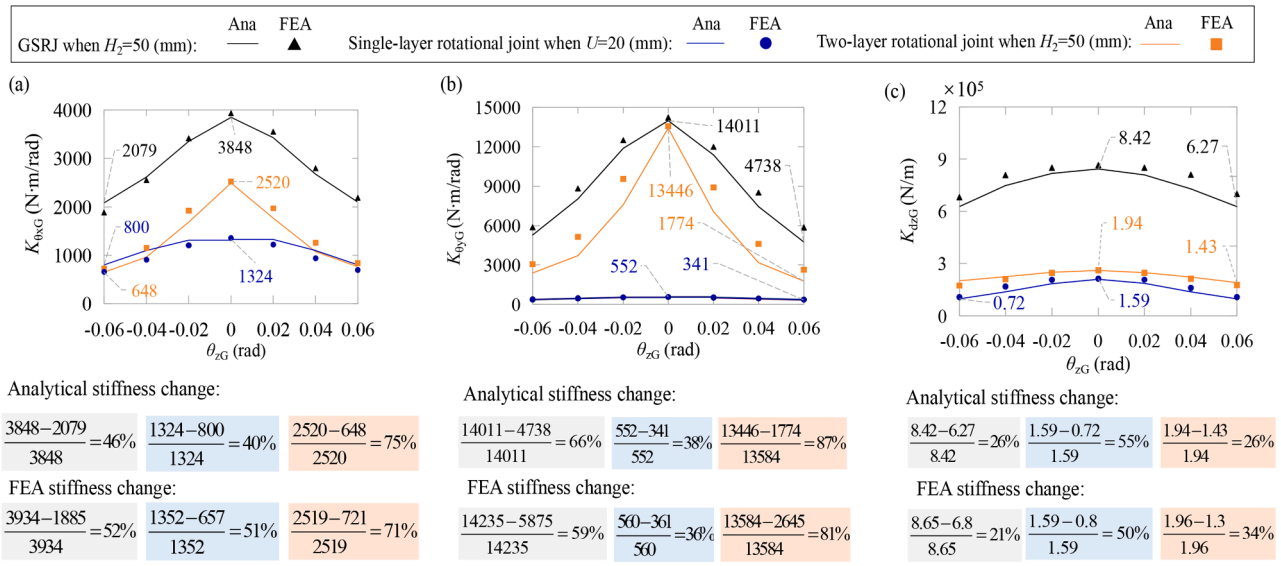


Fig. C5. The stiffness change comparison between the GSRJ (α_1=α_2, α_3=α_4), the two-layer rotational joint, and the single-layer rotational joint. (a-c) Analytical and FEA results of $K_{\theta xG}$, $K_{\theta yG}$, K_{dzG}, and their stiffness changes.

(2) Case 2: stiffness ratio comparison under the same out-of-plane footprint of the sheets

The above results are analyzed under the condition of a consistent out-of-plane footprint (i.e., FT is constant and equal to H_2+2U) across all designs. The following analysis is conducted under the condition that the out-of-plane footprint of the sheets remains constant—that is, the total sheet width is kept the same, as illustrated in Fig. C6(a) and (b). Additionally, the geometric parameters of the GSRJ and the single-layer joint are identical except for H_2 and U. This ensures that both designs achieve the same in-plane rotational stiffness, allowing for a fair comparison of their normalized stiffness ratios—namely, the ratio of the normalized out-of-plane stiffness to the normalized in-plane rotational stiffness—as shown in Fig. C6(c) to (e). The normalized stiffness ratios are expressed in a dimensionless form and are used to evaluate the influence of H_2 on the out-of-plane stiffness. Compared to the single-layer rotational joint, the results of the GSRJ show a significant increase in the normalized stiffness ratios with increasing H_2.

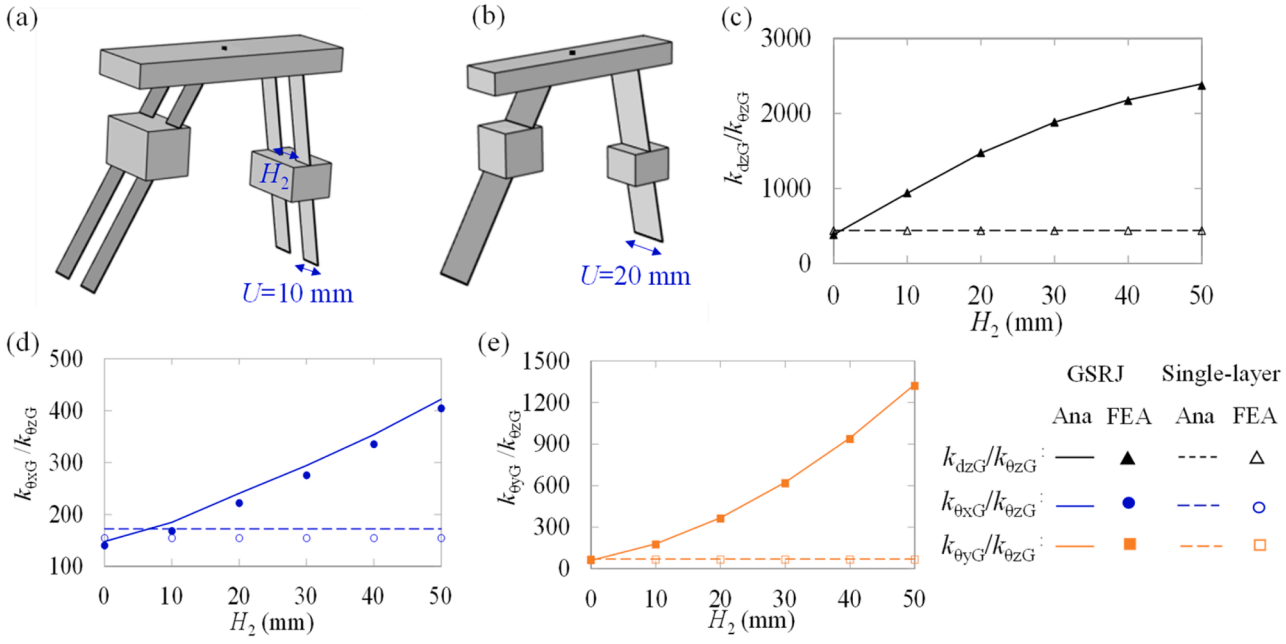


Fig. C6. The normalized stiffness ratios comparison between the GSRJ and the single-layer rotational joint. (a) GSRJ (α_1=α_2, α_3=α_4) (only H_2 ranges from 0 to 50 mm); (b) Single-layer rotational joint; (c-e) Normalized stiffness ratio $k_{\theta xG}/k_{\theta zG}$, $k_{\theta yG}/k_{\theta zG}$, and $k_{dzG}/k_{\theta zG}$, respectively.

(3) Case 3: Stiffness of GSRJ versus geometric parameters

A parametric analysis is conducted to investigate the influence of geometric parameters α_1 and α_2 on the stiffness of the GSRJ with H_2 fixed at 50 (mm). α_1 and α_3 range from 10° to 80° with increments of 5° The remaining parameters are consistent with those specified in Table C1. The primary motion (rotational) stiffness and out-of-plane stiffness results are shown in Fig. C7. $K_{\theta xG}$ increases with the increase of the two tilt angles while $K_{\theta yG}$ and K_{dzG} decrease.

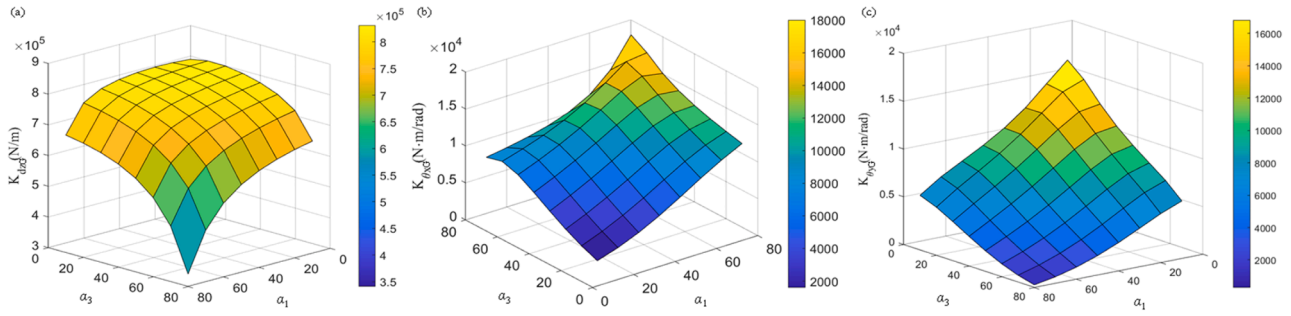


Fig. C7. Influence of tilt angles on the out-of-plane stiffness of the GSRJ ($\alpha_1 = \alpha_2$, $\alpha_3 = \alpha_4$): (a-c) Analytical K_{dzG}, $K_{\theta xG}$, and $K_{\theta yG}$.

C3: Stiffness analysis for the GSTJ and comparisons with counterpart designs

(1) Case 1: Stiffness comparison among the GSTJ, two-layer joint, and single-layer rotational joint under an identical out-of-plane footprint

The two-layer translational joint shares the same geometric parameters as the GSTJ (Fig. C9(f)). The primary motion (translational) stiffness of the GSTJ and the two-layer translational joint is K_{dyG}, which can be calculated by applying F_{yG} of 1 (N) and 1.2 (N) to the motion stage. The corresponding results are presented in Fig. C8(a). K_{dyG} of both designs remains constant with increasing H_2. Then, with $F_{xG} = F_{zG} = 0.5$ (N) and $F_{yG} = 1$(N), $K_{\theta xG}$ (or $K_{\theta yG}$) is obtained using M_{xG} (or M_{yG}) of 0.01 (N·m) and 0.012 (N·m); K_{dzG} is calculated using F_{zG} of 0.5 (N) and 0.6 (N). In Fig. C8(b) and (c), both $K_{\theta xG}$ and K_{dzG} increase significantly with the increase of H_2, while $K_{\theta yG}$ in Fig. C8(c) shows a more gradual increase. When $H_2 = 50$ (mm), $K_{\theta xG}$, $K_{\theta yG}$ and K_{dzG} increase by 83%, 36%, and 81%, respectively. K_{dyG} of both joints remains constant but the out-of-plane stiffness of GSTJ is significantly improved over that of the two-layer translational joint.

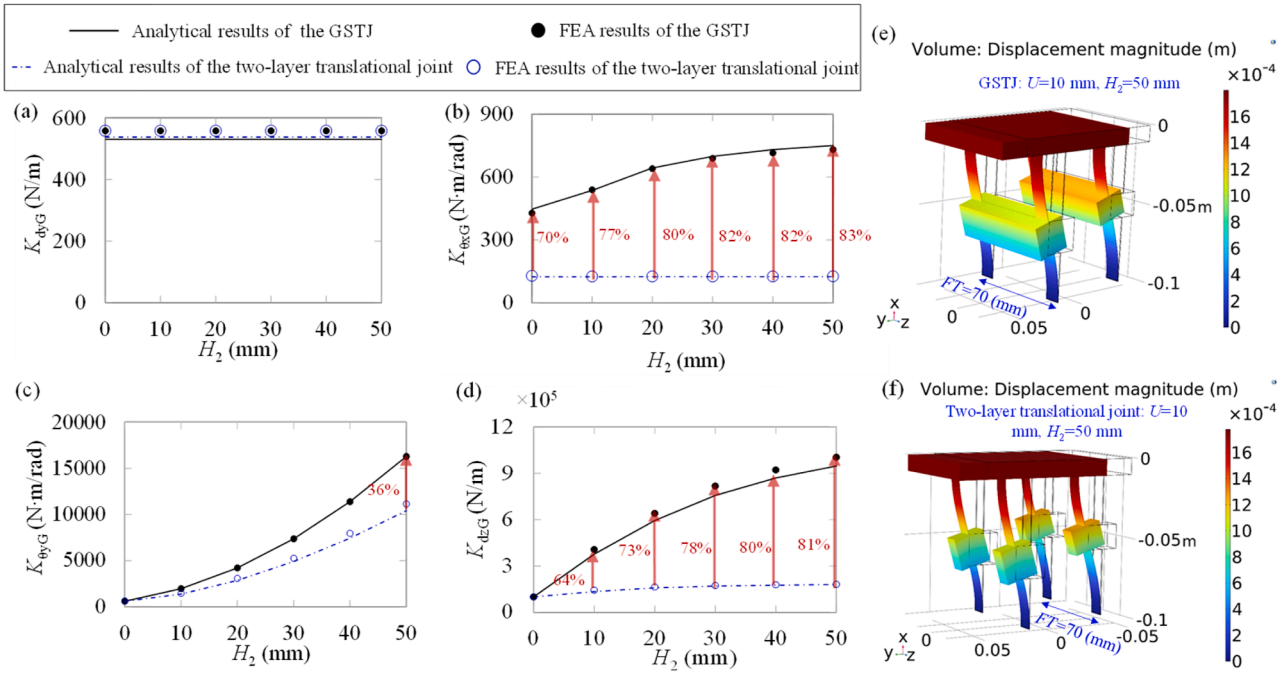


Fig. C8. The stiffness comparison between the GSTJ and the two-layer translational joint versus increasing thickness of the sandwich interconnection H_2. (a) Primary motion (translational) stiffness K_{dyG}; (b) Out-of-plane stiffness $K_{\theta xG}$; (c) Out-of-plane stiffness $K_{\theta yG}$; (d) Out-of-plane stiffness K_{dzG}; (e) GSTJ; (f) Counterpart model: the two-layer translational joint.

Stiffness comparison between the GSTJ and the single-layer translational joint is as follows. The single-layer translational joint is shown in Fig. C9 (f). The geometric parameters of the GSTJ and the single-layer translational joint are slightly different, as detailed in Table 3. All other parameters are identical to those listed in Table C2.

The loading conditions are the same as those in Case 2 of this section. As demonstrated in Fig. C9(a), the GSTJ maintains stable translational stiffness, while the single-layer translational joint shows a progressive increase in both translational stiffness and out-of-plane stiffness. In Fig. C9(b) to (d), the out-of-plane stiffness of the GSTJ increases gradually compared with that of the single-layer joint.

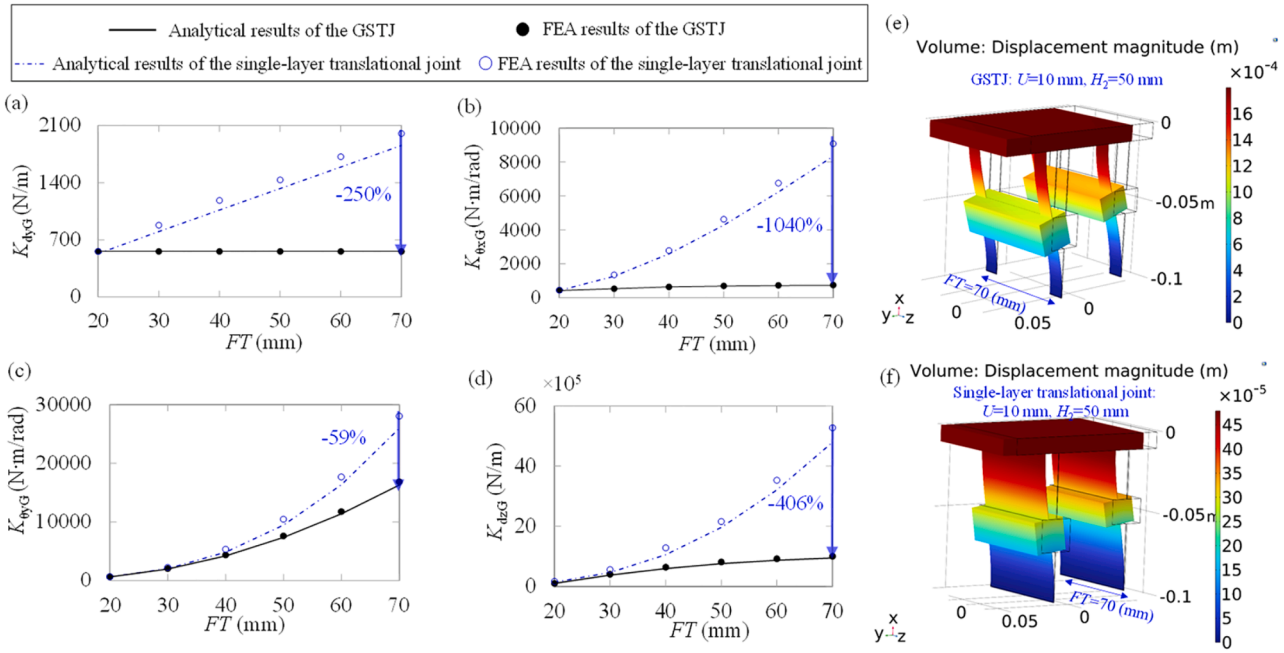


Fig. C9. The stiffness comparison between the GSTJ and the single-layer translational joint versus increasing *FT*. (a) Translational stiffness K_{dyG}; (b) Out-of-plane stiffness $K_{\theta xG}$; (c) Out-of-plane stiffness $K_{\theta yG}$; (d) Out-of-plane stiffness K_{dzG}; (e) The GSTJ; (f) The counterpart model: single-layer translational joint.

H_2 is set to 50 (mm), while the remaining geometric parameters are identical to those listed in Table C2. Fig. C10 illustrates the out-of-plane stiffness $K_{\theta xG}$, $K_{\theta yG}$, and K_{dzG} of the GSTJ, the two-layer translational joint, and the single-layer translational joint. Prescribed primary displacements are applied at the motion stage center. The stiffness changes of $K_{\theta xG}$ and K_{dzG} in the GSTJ are the smallest, while the stiffness change of $K_{\theta yG}$ in the single-layer design is the smallest.

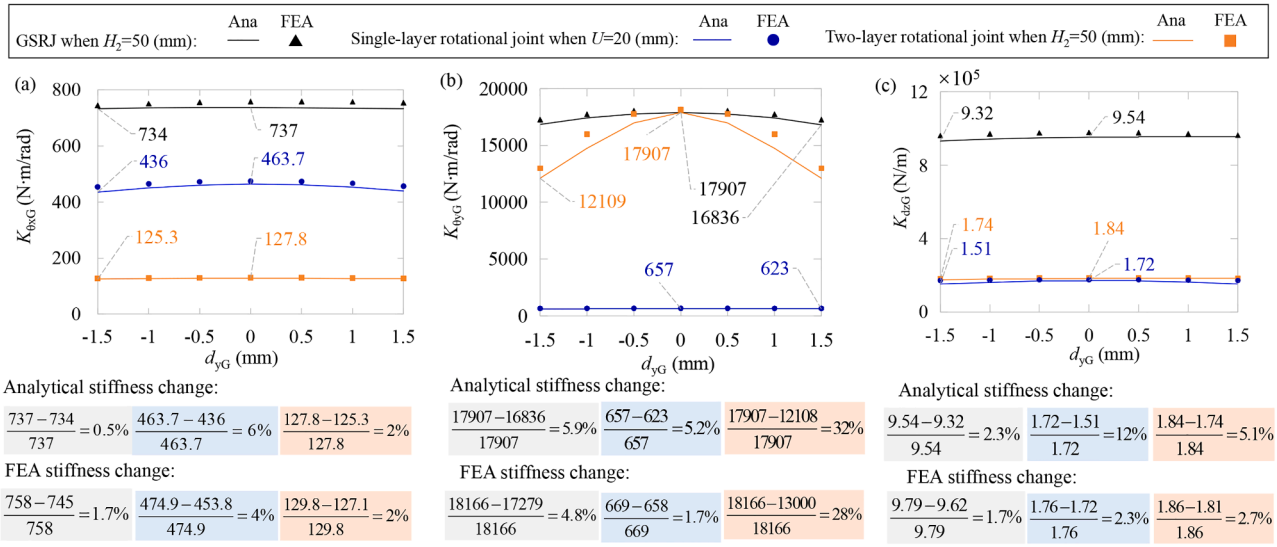


Fig. C10. Stiffness change comparison of the GSTJ, the two-layer translational joint, and the single-layer translational joint. (a-c) Analytical and FEA results of $K_{\theta xG}$, $K_{\theta yG}$, K_{dzG}, and their stiffness changes.

(2) Case 2: stiffness ratio comparison under the same out-of-plane footprint of the sheets

A comparison is made between the normalized stiffness ratios of the GSTJ and the single-layer translational joint, as shown in Figs. C11(a) and (b). It is observed that the stiffness ratios increase markedly with increasing H_2, as illustrated in Fig. C11(c) to (e).

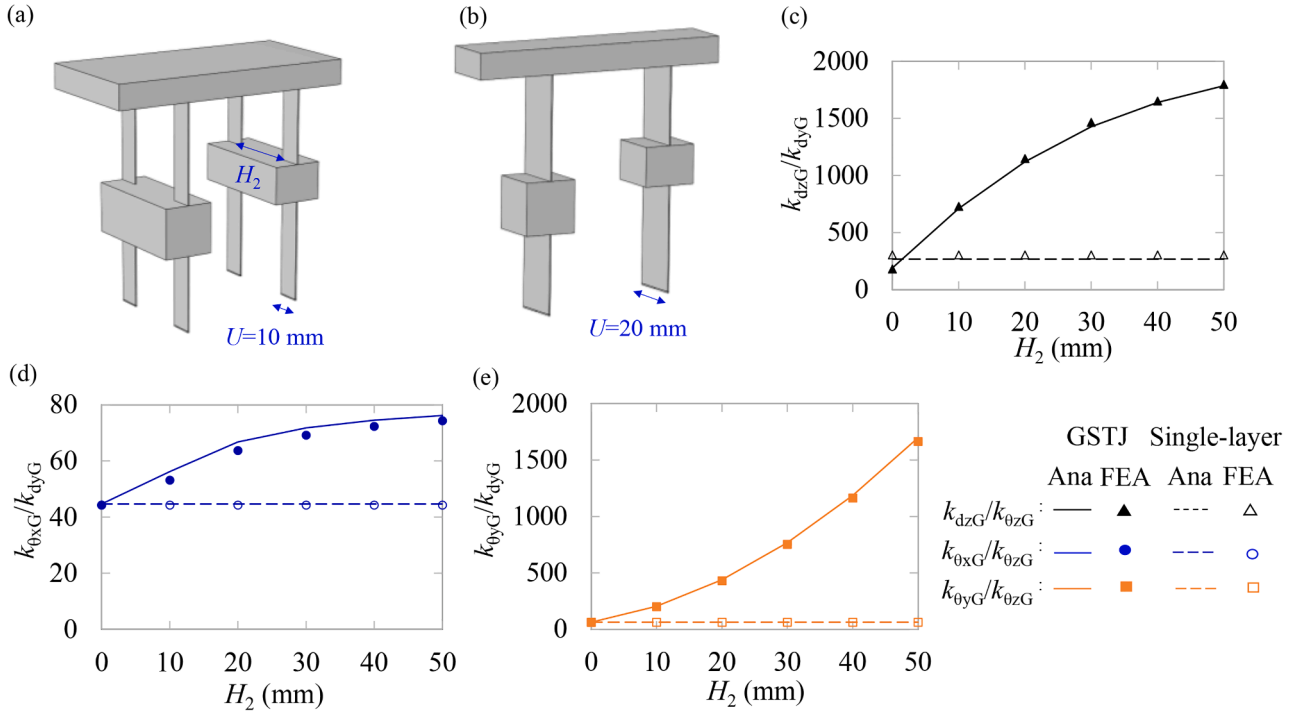


Fig. C11. The normalized stiffness ratio comparison between the GSTJ and the single-layer translational joint. (a) GSTJ model (only H_2 ranges from 0 to 50 mm); (b) the single-layer translational joint model; (c) Normalized stiffness ratio $k_{\theta xG}/k_{dyG}$; (d) Normalized stiffness ratio $k_{\theta yG}/k_{dyG}$; (e) Normalized stiffness ratio k_{dzG}/k_{dyG}.

Appendix D. Nomenclature in the text is indicated as follows

Table D1, Table D2.

Table D1
Abbreviations.

BCM	Beam Constraint Model.
DoF	Degree of Freedom.
DoC	Degree of Constraint.
FEA	Finite Element Analysis.
GSRJ	A generalized sandwich design for the rotational joint.
GSTJ	A generalized sandwich design for the translational joint.
GSLS	A generalized sandwich design for the lumped-compliance sheet.
RCM	Remote center of motion.

Table D2
Symbols. (i = 1 or 2 and j = 1, 2, 3, or 4 in this table).

A_i	Coefficients of the normalized mathematical equations for Line 1 and Line 2.
B_r	Length of the rigid block.
B_1 and B_3	Height of the rigid block.
B_2	Horizontal distance between o_2 and O_G for the left leg of the GSRJ.
B_4	Horizontal distance between o_4 and O_G for the right leg of the GSRJ.
c_j	Sheet center for sheet-j_A and j_B.
$\mathbf{c}_j$	Normalized coordinates of c_j.
D_i	Coefficients of the normalized mathematical equations for Line 1 and Line 2.
$\boldsymbol{D}_C$	Center shift of the GSRJ with respect to O_G-$X_GY_GZ_G$.
$\boldsymbol{D}_{C_min}$	The minimum center shift of the GSRJ.
$\mathbf{d}_C$	Normalized center shift of GSRJ.
D_x, D_y, D_z	Displacements of the motion-stage center.
D_{xc}, D_{yc}, D_{zc}	Center shift with respect to O_G-$X_GY_GZ_G$.
$\mathbf{d}_j$	Normalized displacements at o_j with respect to o_j-$x_jy_jz_j$
$\mathbf{d}_G$	Normalized displacements at O_G with respect to O_G-$X_GY_GZ_G$.
$\mathbf{d}_{LeftLeg}$	Normalized displacements of the left GSLS in GSRJ with respect to O_G-$X_GY_GZ_G$
$\mathbf{d}_{RightLeg}$	Normalized displacements of the right GSLS in GSRJ with respect to O_G-$X_GY_GZ_G$
$\mathbf{D}_{p2}$, $\mathbf{D}_{p4}$,	6 × 6 translational matrices built based on o_{2m_G} and o_{4m_G}, respectively.
$\mathbf{D}_{p2mo1}$, $\mathbf{D}_{p4mo3}$	6 × 6 translational matrices built based on $\mathbf{o}_{2m_o1}$ and $\mathbf{o}_{4m_o3}$, respectively.
$\mathbf{D}_{pAoj}$, $\mathbf{D}_{pBoj}$	6 × 6 translational matrices built based on $\mathbf{o}_{jAm_oj}$ and $\mathbf{o}_{jBm_oj}$, respectively.

(*continued on next page*)

Table D2 (*continued*)

E	Young's Modulus of the material.
F_x, F_y, F_z	Forces loading at O_G with respect to O_G-$X_GY_GZ_G$.
FT	Out-of-plane footprint of the GSRJ.
$\mathbf{f}_G$	Normalized forces loading at O_G with respect to O_G-$X_GY_GZ_G$.
$\mathbf{f}_j$	Normalized forces loading at o_j with respect to o_j-$x_jy_jz_j$.
$\mathbf{f}_{jA}$	Normalized forces loading at o_{jA} with respect to o_{jA}-$x_{jA}y_{jA}z_{jA}$
H_1	Height of the motion stage.
H_2	Sandwich thickness.
I_z	Cross-section moment.
K_{dx}, K_{dy}, K_{dz}	Displacement stiffness with respect to the X_G-axis, Y_G-axis, and Z_G-axis, respectively.
$K_{\theta x}$, $K_{\theta y}$, $K_{\theta z}$	Rotational stiffness with respect to the X_G-axis, Y_G-axis, and Z_G-axis, respectively.
k_{dx}, k_{dy}, k_{dz}	Normalized displacement stiffness with respect to the X_G-axis, Y_G-axis, and Z_G-axis, respectively.
$k_{\theta x}$, $k_{\theta y}$, $k_{\theta z}$	Normalized rotational stiffness with respect to the X_G-axis, Y_G-axis, and Z_G-axis, respectively.
L_j	Sheet length
L_d	Characteristic length for normalization.
M_x, M_y, M_z	Moments loading at O_G with respect to O_G-$X_GY_GZ_G$.
$\mathbf{m}_G$	Normalized moments loading at O_G with respect to O_G-$X_GY_GZ_G$.
$\mathbf{m}_j$	Normalized moments loading at o_j with respect to o_j-$x_jy_jz_j$.
$\mathbf{m}_{jA}$	Normalized moments loading at o_{jA} with respect to o_{jA}-$x_{jA}y_{jA}z_{jA}$
o_j	Midpoint between o_{iA} and o_{iB}.
o_j-$x_jy_jz_j$	Local coordinate system at o_j.
o_{jA}, o_{jB}	Free end of each sheet.
o_{jA}-$x_{jA}y_{iA}z_{jA}$	Local coordinate system at sheet-j_A.
o_{jB}-$x_{jB}y_{jB}z_{jB}$	Local coordinate system at sheet-j_B.
$\mathbf{o}_{iA_oi}$, $\mathbf{o}_{iB_oi}$	Normalized coordinates of o_{iA} and o_{iB} with respect to o_i-$x_iy_iz_i$.
$\mathbf{o}_{2_o1}$	Normalized coordinates of o_2 with respect to o_1-$x_1y_1z_1$ in a non-deformed condition.
$\mathbf{o}_{2_G}$	Normalized coordinates of o_2 with respect to O_G-$X_GY_GZ_G$ in a non-deformed condition.
$\mathbf{o}_{2m_G}$	Normalized coordinates of o_2 with respect to O_G-$X_GY_GZ_G$ in a deformed condition of the GSRJ.
$\mathbf{o}_{4_o3}$	Normalized coordinates of o_4 with respect to o_3-$x_3y_3z_3$ in a non-deformed condition.
$\mathbf{o}_{4_G}$	Normalized coordinates of o_4 with respect to O_G-$X_GY_GZ_G$ in a non-deformed condition.
$\mathbf{o}_{4m_G}$	Normalized coordinates of o_4 with respect to O_G-$X_GY_GZ_G$ in a deformed condition of the GSRJ.
$\mathbf{o}_{jA_oj}$	Normalized coordinates of o_{jA} with respect to o_j-$x_jy_jz_j$ in a non-deformed condition.
$\mathbf{o}_{jB_oj}$	Normalized coordinates of o_{jB} with respect to o_j-$x_jy_jz_j$ in a non-deformed condition.
$\mathbf{O}_{jAm_oj}$	Normalized coordinates of $\mathbf{O}_{jAm_oj}$ with respect to o_j-$x_jy_jz_j$ in a deformed condition of the GSRJ.
$\mathbf{O}_{jBm_oj}$	Normalized coordinates of $\mathbf{O}_{jAm_oj}$ with respect to o_j-$x_jy_jz_j$ in a deformed condition of the GSRJ.
O_G	Center of the motion stage.
$\mathbf{O}_{G_oi}$	Normalized coordinates of O_G with respect to o_j-$x_jy_jz_j$ in the non-deformed condition
O_G-$X_GY_GZ_G$	Global coordinate system of the GSRJ with the origin located at O_G.
Q	Coefficients for calculation the rotational center of GSRJ.
$\mathbf{R}_G$	3×3 Rotational matrices with respect to O_G-$X_GY_GZ_G$. denotes the
$\mathbf{R}_j$	3×3 Rotational matrices with respect to o_i-$x_iy_iz_i$.
$\mathbf{R}_{jA}$ and $\mathbf{R}_{iB}$	3×3 Rotational matrices with respect to o_{iA}-$x_{iA}y_{iA}z_{iA}$.
$\mathbf{R}_{z(\beta j)}$	3×3 Rotational matrix with respect to the Z_G-axis.
$\mathbf{R}_{R1}$, $\mathbf{R}_{R3}$, $\mathbf{R}_{Rz(\beta j)}$	6×6 rotational matrices building with $\mathbf{R}_1$, $\mathbf{R}_3$, and $\mathbf{R}_{z(\beta j)}$ respectively.
$\mathbf{R}_{LeftLeg}$	3×3 Rotational matrix of the left GSLS in GSRJ with respect to o_1-$x_1y_1z_1$
$\mathbf{R}_{RightLeg}$	3×3 Rotational matrix of the right GSLS in GSRJ with respect to o_3-$x_3y_3z_3$
T	Sheet thickness
U	Sheet width
W_i	Coefficients of the normalized mathematical equations.
$[X_c, Y_c, Z_c]^T$	Coordinates of the rotational center of the GSRJ with respect to O_G-$X_GY_GZ_G$.
β_j	Rotational angle for $\mathbf{R}_{z(\beta j)}$
θ_{xj}, θ_{yj}, θ_{zj}	Rotations with respect to o_j-$x_jy_jz_j$.
θ_x, θ_y, θ_z	Rotations of the motion stage with respect to O_G-$X_GY_GZ_G$.

Data availability

Data will be made available on request.

References

[1] Xie Y, Yu J, Zhao H. Deterministic design for a compliant parallel universal joint with constant rotational stiffness. J Mech Robot 2018;10(3):32–5.

[2] Palmieri G, Palpacelli MC, Callegari M. Study of a fully compliant u-joint designed for minirobotics applications. J Mech Des Trans ASME. 2012;134(11):111003.

[3] Jensen BD, Howell LL. The modeling of cross-axis flexural pivots. Mech Mach Theory 2002;37(5):461–76.

[4] Gan J, Xie W, Yang W, Lei S, Lei B. Design of a novel Z-shaped flexure hinge and a 2DOF XY precision positioning platform. Precis Eng 2025;93(February):459–69.

[5] Chen W, Wang R, Liu K. Activate compliant mechanisms for optimized actuation by LCE-based artificial muscles. Mech Mater 2024;189:104879.

[6] Dang MP, Le TD, Le HG, Tran CT. Design and optimization of a novel compliant Z-positioner for the nanoindentation testing device. Machines 2025;13(485): 13060485.

[7] Zhao Y, Xi F, Hao G, Tian Y, Li L, Wang J. Kineto-static analysis of a hybrid manipulator consisting of rigid and flexible limbs with locking function for planar. Mech Mach Theory 2024;203:105802.

[8] Bilancia P, Baggetta M, Hao G, Berselli G. A variable section beams based Bi-BCM formulation for the kinetostatic analysis of cross-axis flexural pivots. Int J Mech Sci 2021;205(June):106587.

[9] Runciman M, Darzi A, Mylonas GP. Soft robotics in minimally invasive surgery. Soft Robot 2019;(00):00.

[10] Simaan N. Snake-like units using flexible backbones and actuation redundancy for enhanced miniaturization. In: Proc - IEEE Int Conf Robot Autom. 2005; 2005. p. 3012–7.

[11] Zhang T, Ping Z, Zuo S. Miniature continuum manipulator with 3-DOF force sensing for retinal microsurgery. J Mech Robot 2021;13(4):041002.

[12] Li S, Abdelaziz S, Wang L, Hao G. Design and kinetostatic analysis of a tip-stiffness improved compliant continuum robot using anti-buckling universal joints. Int J Rob Res 2025:1–33. 0(0).

[13] Wang X, Liu C, Gu J, Zhang W. A parametric model for rotational compliance of a cracked right circular flexure hinge. Int J Mech Sci 2015;94-95:168–73.

[14] Wu L, Crawford R, Roberts J. Dexterity analysis of three 6-DOF continuum robots combining concentric tube mechanisms and cable-driven mechanisms. IEEE Robot Autom Lett 2017;2(2):514–21.

[15] Hannan MW, Walker ID. Novel kinematics for continuum robots. Adv Robot Kinemat 2000:227–38.

[16] Hassan T, Cianchetti M, Mazzolai B, Laschi C, Dario P. Active-braid, a bioinspired continuum manipulator. IEEE Robot Autom Lett 2017;2(4):2104–10.
[17] Wu C, Zhao P, Chen P, Ni Z, Yue S, Li L, et al. Design, dynamic modelling and experimental study on a tether-net system for active debris removal. Mech Mach Theory 2025;208:105958.
[18] Zhu J, Li S, Hao G. Nonlinear design of a general single-translation constraint and the resulting general spherical joint. J Mech Des 2025;147(10):1–22.
[19] Hao G, Kong X. A novel large-range XY compliant parallel manipulator with enhanced out-of-plane stiffness. J Mech Des Trans ASME. 2012;134(6):061009.
[20] Chen G, Kang Y, Liang Z, Zhang Z, Wang H. Kinetostatics modeling and analysis of parallel continuum manipulators. Mech Mach Theory 2021;163:104380.
[21] Dearden J, Grames C, Orr J, Jensen BD, Magleby SP, Howell LL. Cylindrical cross-axis flexural pivots. Precis Eng 2018;51:604–13.
[22] Liang H, Hao G, Olszewski OZ. Pakrashi V. Ultra-low wide bandwidth vibrational energy harvesting using a statically balanced compliant mechanism. Int J Mech Sci 2022;219:107130.
[23] Hargrove B, Nastevska A, Frecker M, Jovanova J. Pseudo rigid body model for a nonlinear folding compliant mechanism. Mech Mach Theory 2022;176:105017.
[24] Blad TWA, Van Ostayen RAJ, Herder JL. Tolou N. A statically balanced compliant ortho-planar mechanism for low-frequency energy harvesting. J Mech Des 2022; 144(7):1–7.
[25] Ma X, Wilson A, Rahn CD, Trolier-McKinstry S. Efficient energy harvesting using piezoelectric compliant mechanisms: theory and experiment. J Vib Acoust 2016; 138(2):1–9.
[26] Dong X, Palmer D, Axinte D, Kell J. In-situ repair/maintenance with a continuum robotic machine tool in confined space. J Manuf Process 2019;38(1):313–8.
[27] Mohammad A, Russo M, Fang Y, Dong X, Axinte D, Kell J. An efficient follow-the-leader strategy for continuum robot navigation and coiling. IEEE Robot Autom Lett 2021;6(4):7493–500.
[28] Dong X, Raffles M, Guzman SC, Axinte D, Kell J. Design and analysis of a family of snake arm robots connected by compliant joints. Mech Mach Theory 2014;77: 73–91.
[29] Dong X, Raffles M, Cobos-Guzman S, Axinte D, Kell J. A novel continuum robot using twin-pivot compliant joints: design, modeling, and validation. J Mech Robot 2016;8(2):021010.
[30] che Chang J, H Dai, Wang X, Axinte D, Dong X. Development of a continuum robot with inflatable stiffness-adjustable elements for in-situ repair of aeroengines. Robot Comput Integr Manuf 2025;95(February):103018.
[31] Russo M, Sadati SMH, Dong X, Mohammad A, Walker I, Bergeles C, et al. Continuum robots: an overview. Adv Intell Syst 2025;5(5).
[32] Yuan P, Sun C, Chang X, Dong X, Song Z, Sun T, et al. Design of a deployable continuum robot(DCR) with coiling mechanism. IEEE/ASME Trans Mechatronics 2025;95:103018.
[33] Xu K, Simaan N. Analytic formulation for kinematics, statics, and shape restoration of multibackbone continuum robots via elliptic integrals. J Mech Robot 2010;2(1): 1–13.
[34] Xu K, Liu Z, Zhao B, Liu H, Zhu X. Composed continuum mechanism for compliant mechanical postural synergy: an anthropomorphic hand design example. Mech Mach Theory 2018.
[35] Dai ZC, Wu ZH, Zhao JR, Xu K. A robotic laparoscopic tool with enhanced capabilities and modular actuation. Sci China Technol Sci 2019;62(1):47–59.
[36] Xu K, Zhao J, Fu M. Development of the SJTU unfoldable robotic system (SURS) for single port laparoscopy. IEEE/ASME Trans Mechatronics 2015;20(5):2133–45.
[37] Zhao H, Bi S, Yu J. A novel compliant linear-motion mechanism based on parasitic motion compensation. Mech Mach Theory 2012;50:15–28.
[38] Bi S, Zhao H, Yu J. Modeling of a cartwheel flexural pivot. J Mech Des Trans ASME. 2009;131(6):061010.
[39] Pei X, Yu J, Zong G, Bi S, Hu Y. A novel family of leaf-type compliant joints: combination of two isosceles-trapezoidal flexural pivots. J Mech Robot 2009;1(2): 021005.
[40] Awtar S, Slocum AH. Constraint-based design of parallel kinematic XY flexure mechanisms. J Mech Des Trans ASME. 2007;129(8):816–30.
[41] Nastevska A, Jovanova J, Frecker M. Design of compliant joints for large scale structures. In: ASME 2020 Conf Smart Mater Adapt Struct Intell Syst SMASIS 2020; 2020. p. 1–10.
[42] Awtar S, Shimotsu K, Sen S. Elastic averaging in flexure mechanisms: a three-beam parallelogram flexure case study. J Mech Robot 2010;2(4).
[43] Awtar S, Slocum AH, Sevincer E. Characteristics of beam-based flexure modules. J Mech Des Trans ASME. 2007;129(6):625–39.
[44] Pei X, Yu J, Zong G, Bi S, Yu Z. Analysis of rotational precision for and isosceles-trapezoidal flexural pivot. J Mech Des Trans ASME. 2008;130(5):052302.
[45] Hao G, Yu J, Liu Y. Compliance synthesis of a class of planar compliant parallelogram mechanisms using the position space concept. In: 2018 Int Conf Reconfigurable Mech Robot ReMAR 2018 - Proc; 2018. June.
[46] Chen X, Tai K, Tan H, Xie Z. Design of a two-stage compliant asymmetric piezoelectrically actuated microgripper with parasitic motion compensation. Mech Syst Signal Process 2024;208(September 2023):110950.
[47] Chen X, Xie Z, Tai K, Tan H. Design of low parasitic motion microgripper based on symmetrical parallelogram mechanism. Sensors Actuators A Phys 2024;367 (September 2023):115072.
[48] Huo T, Yu J, Zhao H, Wu H, Zhang Y. A family of novel RCM rotational compliant mechanisms based on parasitic motion compensation. Mech Mach Theory 2021; 156:104168.
[49] Li S, Hao G. Design and nonlinear spatial analysis of compliant anti-buckling universal joints. Int J Mech Sci 2022;219:107111.
[50] Huo T, Yu J, Zhao H. Design of a kinematic flexure mount for precision instruments based on stiffness characteristics of flexural pivot. Mech Mach Theory 2020;150: 103868.
[51] Zhao H, Bi S, Yu J. Nonlinear deformation behavior of a beam-based flexural pivot with monolithic arrangement. Precis Eng 2011;35(2):369–82.
[52] Zhao H, Han D, Bi S. Modeling and analysis of a precise multibeam flexural pivot. J Mech Des Trans ASME. 2017;139(8):081402.
[53] Li S, Hao G, Chen Y, Zhu J, Berselli G. Nonlinear analysis of a class of inversion-based compliant cross-spring pivots. J Mech Robot 2022;14(3):1–14.
[54] Bai R, Zhang H, Yang N, Yu Z, Li B, Xu Q, et al. Optimization of a near-zero-center-shift compliant pivot for large motion range and high bearing stiffness. Mech Mach Theory 2025;216(September).
[55] Zhao H, Bi S. Accuracy characteristics of the generalized cross-spring pivot. Mech Mach Theory 2010;45(10):1434–48.
[56] ¨c Tissot-Daguette L, F Cosandier, Thalmann E, Henein S. Near-zero parasitic shift flexure pivots based on coupled n-RRR planar parallel mechanisms. ASME jounral Mech Robot 2024;16(November):1–13.
[57] Nguyen HD, Van Le H, Dang MP. Analytical modeling and computational optimization for a 1-DoF compliant mechanism. Vietnam J Mech 2024;46(4): 311–30.
[58] Li H, Chen W, Yi L, Leng C, Wu H. Design, modeling and manufacture error identification of a new 6-degree-of-freedom (6-DOF) compliant parallel manipulator. Mech Sci 2025:143–56.
[59] Awtar S, Slocum AH. Flexure systems based on a symmetric diaphragm flexure. In: Proceedings of the ASPE 2005 Annual Meeting; 2005.
[60] Sun Y, Lueth TC. Member S. Safe manipulation in robotic surgery using compliant constant-force mechanism. IEEE Trans Med Robot Bionics 2023;5(3):486–95.
[61] Sun Y, Lueth TC, Member S. Enhancing torsional stiffness of continuum robots using 3-D topology optimized flexure joints. IEEE/ASME Trans Mechatronics 2023; 28(4):1844–52.
[62] Serafino S, Bruzzone L, Fanghella P, Verotti M. Design of compliant pivots based on three-flexure arrangement. In: Proceedings of the ASME 2024 International Design Engineering Technical Conferences and Computers and Information in Engineering Conference; 2024. p. 1–6.
[63] Peterson BT, Hopkins JB, Clites TR. Adapting cross-axis flexural pivots to minimize peak stress in specific planar load-deformation regimes. In: Proceedings of the ASME 2025, International Design Engineering Technical Conferences and Computers and Information in Engineering Conference; 2025. p. 1–10.
[64] Serafino S, Fanghella P, Verotti M. Design and testing of high-accuracy curved cross-axis flexural pivots with cable-driven actuation. Mech Mach Theory 2023; 189(January):105418.
[65] Wu S, Gao H, Ling M, Pan M, Chen T. Compliance analysis of transversely asymmetric flexure hinges for use in a piezoelectric Scott-Russell microgripper. Precis Eng 2024;91(September):95–106.
[66] Olfatnia M, Sood S, Awtar S. An asymmetric flexure mechanism for comb-drive actuators. Rev Sci Instrum 2012;83:116105.
[67] Li J, Wang J, Zhao J, Design Wei G. Dimensional synthesis and evaluation of a novel two- degrees-of-freedom spherical remote center of motion mechanism for minimally invasive surgery. ASME jounral Mech Robot 2024;16(May):1–11.
[68] Tang H, Li Y, Zhang JW, Zhang D, Yu H. Design and optimization of a novel sagittal-plane knee exoskeleton with remote-center-of-motion mechanism. Mech Mach Theory 2024;194(May 2023):105570.
[69] Jin M, Yang Z, Ynchausti C, Zhu B, Zhang X, Howell LL. Large-deflection analysis of general beams in contact-aided compliant mechanisms using chained pseudo-rigid-body model. J Mech Robot 2020;12(3):1–10.
[70] Bagivalu Prasanna P, Bapat SG, Midha A, Lodagala V. A methodology for determining static mode shapes of a compliant mechanism using the pseudo-rigid-body model concept and the degrees-of-freedom analysis. J Mech Robot 2020;12 (2):1–10.
[71] Venkiteswaran VK, Su HJ. A versatile 3R pseudo-rigid-body model for initially curved and straight compliant beams of uniform cross section. J Mech Des 2018; 140(9):1–8.
[72] Bilancia P, Berselli G. An overview of procedures and tools for designing nonstandard beam-based compliant mechanisms. CAD Comput Aided Des 2021; 134:103001.
[73] Zhu ZW, Zhou XQ, Wang RQ, Liu Q. A simple compliance modeling method for flexure hinges. Sci China Technol Sci 2015;58(1):56–63.
[74] Chen G, Ma F. Kinetostatic modeling of fully compliant bistable mechanisms using Timoshenko beam constraint model. J Mech Des Trans ASME. 2015;137(2):1–10.
[75] Gohari M, Sulaiman S, Schetter F, Ficuciello F. A sliding mode controller design based on Timoshenko Beam theory developed for a prosthetic hand wrist. 2025 11th Int Conf Autom Robot Appl 2025:338–42.
[76] Li P, Wang K, Wang B. Chained Timoshenko beam constraint model with applications in large deflection analysis of compliant mechanism. ASME jounral Mech Robot 2025;17(October).
[77] Bai R, Awtar S, Chen G. A closed-form model for nonlinear spatial deflections of rectangular beams in intermediate range. Int J Mech Sci 2019;160(December 2018):229–40.
[78] Zhu J, Hao G, Li S, Kong X. A compact mirror-symmetrical XY compliant parallel manipulator for minimizing parasitic rotations. J Mech Des 2022;144(7).
[79] Radgolchin M, Awtar S. Minimizing under-constraint in folded beams to achieve optimal bearing performance in diaphragm flexures. ASME J Mech Robot 2025;17: 115002.
[80] Hao G, Li H. Nonlinear analytical modeling and characteristic analysis of a class of compound multibeam parallelogram mechanisms. J Mech Robot 2015;7(4): 041016.

[81] Radgolchin M, Rath S, Awtar S. A multi-layer parallelogram flexure architecture for higher out-of-plane load bearing stiffness. ASME J Mech Des 2025;147:073302.
[82] Radgolchin M, Rath S, Awtar S. A novel sandwich flexure blade with improved out-of-plane stiffness. In: Proceedings of the ASME 2024 International Design Engineering Technical Conferences and Computers and Information in Engineering Conference; 2024. p. 1–11.
[83] Zhu J, Hao G. Modelling of a general lumped-compliance beam for compliant mechanisms. Int J Mech Sci 2024;263:108779.
[84] Bai R, Chen G, Awtar S. Closed-form solution for nonlinear spatial deflections of strip flexures of large aspect ratio considering second order load-stiffening. Mech Mach Theory 2021;161:104324.
[85] Verotti M, Serafino S, Fanghella P. Position accuracy criteria for planar flexural hinges. Precis Eng 2023;80:82–94.
[86] Liu T, Hao G, Zhu J, Kuresangsai P, Abdelaziz S, Wehrle E. Modeling compliant bistable mechanisms: an energy method based on the high-order smooth curvature model. Int J Mech Sci 2024;275(December 2023):109315.
[87] Wang N, Zhang Z, Zhang X, Cui C. Optimization of a 2-DOF micro-positioning stage using corrugated flexure units. Mech Mach Theory 2018;121:683–96.
[88] Kong K, Chen G, Hao G. Kinetostatic modeling and optimization of a novel horizontal-displacement compliant mechanism. J Mech Robot 2019;11(6).